

**University of**  
**Strathclyde**  
**Mechanical**  
**Engineering**

**Research into the installation of, and optimisation of,  
turning vanes and drag reduction technology as  
applied to the Land Rover Discovery MK3 vehicle**

**Johnathan James Kennedy**

**University of Strathclyde**  
**Department of Mechanical Engineering**

**Research into the installation of, and optimisation of,  
turning vanes and drag reduction technology as  
applied to the Land Rover Discovery MK3 vehicle**

**By**

**Johnathan James Kennedy**

**A thesis presented in fulfilment of the requirements  
for the degree of Master of Philosophy**

**2009**

## **Copyright statement**

This thesis is the result of the author's original research. It has been composed by the author and has not been previously submitted for examination which has led to the award of a degree.

The copyright of this thesis belongs to the author under the terms of the United Kingdom Copyright Acts as qualified by University of Strathclyde Regulation 3.50. Due acknowledgement must always be made of the use of any material contained in, or derived from, this thesis.'

# Acknowledgements

Special thanks to:

Dr Matthew Stickland – Senior lecturer University of Strathclyde

Adrian Gaylard – Senior Aerodynamicist *Jaguar – Land Rover*

Alistair Duff – Aerodynamics lab technician

All of the University of Strathclyde technical work-shop staff

## Abstract

Previous industry-based research has been carried out on the drag reduction of the *Land Rover Discovery MK3* at *Jaguar-Land Rover* based on CFD models.

The object of this research is to examine any beneficial effect caused by the addition of turning vanes, internal or external - and also to research further into energising the separated shear layer passing over the vehicle.

It has been noted at *Jaguar* that the cumulative drag coefficient for the open cooling case is lower than that for the closed cooling case, until the cooling flow re-emerges into the bulk flow.

This indicates that drag forces due to separation of the boundary layer from the bluff surfaces of the *Discovery* could be reduced through applying turning vane structures.

The Drag on a body is determined greatly by the character of the boundary layer, more specifically whether the boundary layer is attached or unattached.

Increasing the surface area that the boundary layer stays attached to greatly increases the aerodynamic performance of the vehicle. The lines of flow separation (and also re-attachment) of this boundary layer are very important, and factors that induce a premature separation in three-dimensional flow have been examined in this research.

It has been found during the course of this research that turning vanes can significantly decrease drag when placed on specific areas that display an adverse pressure gradient on the surface of the vehicle. This can be by as much as 13%. Rear turning vane structures have been found to reduce drag to the greatest extent, and when used in conjunction with vortex generation structures drag reduction is increased.

A rear roof turning vane inlet of approximately the thickness of the attached vehicle boundary layer leads to drag reduction and also to increased down force. Fin-shaped vortex generators angled slightly in the flow direction create a turbulent wake which encourages flow to remain attached to the rear surface area for longer.

# Table of Contents

<b>1. Literature review</b>	1
1.1. <i>Introduction</i>	1
1.2. <i>Aerodynamic drag and mileage effect</i>	2
1.3. <i>Boundary layer control</i>	6
1.4. <i>Improving aerodynamics</i>	8
1.5. <i>Turning vane background</i>	11
1.6. <i>Current turning vane applications</i>	12
1.7. <i>CFD discussion</i>	17
<b>2. Computational fluid dynamic model generation</b>	21
2.1. <i>Geometry creation</i>	21
2.2. <i>LASER scanning procedure</i>	21
2.3. <i>Manual surface creation</i>	25
2.3.1. <i>Wheel scanning and surface creation</i>	28
2.4. <i>Final model discussion</i>	29
<b>3. Meshing, simulation and experimental design</b>	31
3.1. <i>Meshing technique</i>	31
3.2. <i>Car half-model with RNG k-epsilon turbulence</i>	35
<b>4. Computational fluid dynamic Results and Analysis</b>	36
4.1. <i>Datum model analysis results</i>	36
4.2. <i>Applied drag reduction design results</i>	39
4.2.1. <i>Bluff front side vane</i>	39
4.2.2. <i>Windscreen 'A' frame vane</i>	40
4.2.3. <i>Windscreen roof vane</i>	42
4.2.4. <i>Side rear vane</i>	44
4.2.5. <i>Rear roof turning vane</i>	45
4.3. <i>Rear roof turning vane adaption results</i>	46
4.3.1. <i>Large inlet/nozzle outlet</i>	51
4.3.2. <i>Narrow inlet/diffuser outlet</i>	53
4.3.3. <i>Rear roof cowl</i>	54
4.3.4. <i>Rear roof semi-cowl</i>	56
<b>5. Rear vortex generation and associated drag reduction</b>	57
5.1. <i>Vortex generation discussion</i>	57
5.2. <i>Vortex generation results</i>	58
5.2.1. <i>Delta 'bump' Vortex generators</i>	58
5.2.2. <i>Delta 'fin' Vortex generators</i>	60
5.2.3. <i>Rear vane with 'bump' VG addition</i>	62
5.2.4. <i>Rear vane with 'fin' VG addition</i>	64
5.2.5. <i>Front fender vortex generator design</i>	65
5.3. <i>Design effects on boundary layer separation</i>	66
<b>6. Engineering drawings, and wind tunnel set-up</b>	73
6.1. <i>Lab set-up drag force test</i>	77
6.2. <i>Air velocity calculations</i>	78
<b>7. Wind-tunnel results and Analysis</b>	81
7.1. <i>Rear turning vane empirical data</i>	81
7.2. <i>Moving surfaces (wheel rotation discussion)</i>	85
7.3. <i>Simulation wind-tunnel</i>	88

7.4. <i>Similitude</i> .....	91
7.4.1. <i>Geometric Similarity</i> .....	92
<b>8. Conclusions</b> .....	93
8.1. <i>Turning vane installation data</i> .....	93
8.2. <i>Vortex Generation data</i> .....	93
8.3. <i>Downforce data</i> .....	94
<b>9. References</b> .....	96
<b>10. Publications</b> .....	99
<b>11. Appendix</b> .....	100
11.1. <i>General arrangement drawing</i> .....	100
11.2. <i>Fairing stand Drawing</i> .....	101
11.3. <i>Aerodynamic drag balance stand Drawing</i> .....	102
11.4. <i>Model/Balance connector Drawing</i> .....	103
11.5. <i>Project Gantt chart</i> .....	104
11.6. <i>Aerodynamic Force plots</i> .....	105

## Nomenclature

CFD	<i>Computational Fluid Dynamics</i>
SUV	<i>Sports Utility Vehicle</i>
$C_D$	<i>Coefficient of Drag</i>
$C_{DC}$	<i>Coefficient of Drag ‘Cooling-flow’</i>
$Y^+$	<i>Dimensionless wall distance</i>
VG	<i>Vortex Generator</i>
TV	<i>Turning Vane</i>
PET	<i>Polygon Editing Tool</i>
NURBS	<i>Non-Uniform Rational Bézier-Spline</i>
CATIA	<i>Computer aided Design Programme</i>
Geomagic	<i>Computer aided Design/manufacture Programme</i>
CAD	<i>Computer Aided Design</i>
TGRID	<i>Tetrahedral-Grid, meshing code for pre-processing</i>
RNG	<i>Re-Normalisation Group</i>
k-epsilon	<i>Computational turbulence kinetic-energy model</i>
Re	<i>Reynolds number</i>

# 1. Literature review

## 1.1. Introduction

Vehicle manufacturers have had a keen interest in vehicle aerodynamics for over 70 years - since the introduction of the Chrysler 'Airflow' in 1934. But even in those early days aerodynamic styling was viewed as a dark art, and rarely left the drawing board. The main exponents of aerodynamic styling and structure were the auto-racing sports; it was quickly discovered that the better aerodynamically designed car could win, and win often.

Even after the major car companies' track successes, due in no small measure to streamlining leading to decreased drag, the vehicle companies were still reluctant to incorporate these aspects in everyday consumer cars. But since those early days design priority has incrementally shifted in this direction; the need to improve fuel economy has now become paramount.

The consumer has hastened this advance in everyday car aerodynamics - the requirements of the consumer together with his wishes have created a difficult engineering criteria set. The easiest method of fuel economy is to create smaller, light-weight cars, with small fuel efficient engines – a predicament arises when a sizeable consumer base is known to want heavy-duty seven-passenger SUVs with an off-road heritage - while also obtaining good motorway/inner-city fuel efficiency.

“The main driver for lower aerodynamic drag is fuel economy”<sup>1</sup> says Max Schenkel, general Motors technical fellow, aerodynamics. “As long as federal standards for fuel economy increase and fuel costs go up, aerodynamic drag will have to be improved.”<sup>1</sup>

Financially automakers see the benefits of aerodynamics too:

“Aero benefits can almost be cost-free to some extent — just how you bend the metal and how you execute gaps and joints, and...a lot of that is design.”



"If you're trying to reduce weight by adding expensive exotic materials, that's not easy to do. And improving engine efficiency, that's not easy to do. So the leading strategy is to improve aerodynamics whenever possible. That's why we built our own full-size wind tunnel here." Says Rick Aneiros, Chrysler Group's vice-president of Jeep and truck design.<sup>1</sup>

Aerodynamics with respect to vehicle design is initiated virtually at the conceptual design stage. With the modern ease of translating CAD data to CFD programmes, and of obtaining quantifiable results in a short period of time (dependent on computing power), aerodynamic design verification has never been easier. And it also proves to be beneficial in the long term of the project. Wind tunnel set-ups can be simulated virtually and reasonable data sets can be obtained before prototype production and actual wind tunnel testing commences.

## 1.2. *Aerodynamic drag and mileage effect*

Fuel economy and aerodynamics are relatively new associates, as was illustrated in section 1.1; speed and competition have been replaced in a big way by the recent fuel economy and 'green' aspirations of modern automobile companies. The obvious conclusion in times such as these is to look for a quantifiable gauge of a commercial vehicle's aerodynamic 'worthiness' - that gauge is the vehicle  $C_D$ .

The 'Coefficient of drag' ( $C_D$ ) is essentially a unit-less ratio containing the  $F_D$  (total drag force [N]) and other physical constants (see Table 1). In basic terms the  $C_D$  is the measure of the ease which a structure is observed to possess while immersed in, and moving through, a fluid. For a given object the  $C_D$  varies only with Reynolds number. In the automotive case this fluid is air - but any fluid *can* be used.

Drag is the major factor, but not the *only* factor, the strategic design chief at Volvo, Doug Frasher, says:

"There's more to aerodynamics than just drag," He goes on to say: "There's downforce and lift. And there is yawing moment, which is basically when you're in a

crosswind, how much is the vehicle steered by the wind that is pushing on it? And then there's noise. So we try to look for all of those factors.”<sup>1</sup>

These are obviously important factors affecting the aerodynamics of vehicles. However, these factors are more suited to wind tunnel testing on full scale cars - thus a little beyond the scope of this investigation.




























"For a full-size truck, a change in drag coefficient of 0.01 is approximately equal to an improvement in fuel economy of 0.1 mpg on the combined city/highway driving cycle,"<sup>1</sup> says GM's Schenkel. He adds: "The same drag coefficient reduction can improve a car's fuel economy by approximately 0.2 mpg."<sup>1</sup>

This statement by Schenkel indicates that a drag coefficient decrease leads to a miles-per-gallon increase, seen consistently in trucks and ‘cars’. Although a ‘full-size truck’ will undoubtedly have a larger projected area ( $A_{REF}$ ) than a ‘car’, the economy saving correlates for both vehicles. This indicates that an SUV such as the *Discovery* would fall somewhere between the two vehicle types discussed by Schenkel.

Such improvements are a major boon to the average car buyer and operator, but major drag-reduction on the sizeable and boxy SUV market can greatly increase the popularity and affordability of already costly, diesel-hungry designs. The drag coefficient is a function of Reynolds number. Table 1 shows the coefficient of drag equation, as well as  $C_D$  data recorded from wind tunnel testing of specific shapes; note that the tear-drop shape has the lowest  $C_D$ .

Vehicle velocity is obviously an important factor; the reason that inner-city buses have no discernable drag-reduction features is due to the nature of their ‘stop-go’ route systems, and the lack of time at speeds exceeding 35mph. At a speed of 70mph the vehicle in question has nearly 4 times the total drag Force acting upon it; the velocity to total drag force viewed graphically is parabolic and varies with the square of velocity, until terminal velocity is reached.

**Table 1 - Coefficient of drag equation and details**

$F_D = \frac{1}{2} \rho u^2 C_D A,$ <p><math>F_D</math> = the Force of drag (the total force N)</p> <p><math>\rho</math> = the mass density of the fluid, modelled in <i>fluent</i> as air at 15°C (1.225 kg/m<sup>3</sup>)</p> <p><math>u</math> = the velocity, modelled in <i>fluent</i> as air velocity at 25m/s</p> <p><math>C_D</math> = Drag coefficient, dimensionless constant</p> <p><math>A</math> = the projected area of the vehicle, from front cross-sectional area, calculated via <i>fluent</i></p>	<table border="0"> <thead> <tr> <th data-bbox="847 181 1134 226">Shape</th> <th data-bbox="1134 181 1418 226">Drag Coefficient</th> </tr> </thead> <tbody> <tr> <td data-bbox="847 226 1134 315">Sphere → </td> <td data-bbox="1134 226 1418 315">0.47</td> </tr> <tr> <td data-bbox="847 315 1134 405">Half-sphere → </td> <td data-bbox="1134 315 1418 405">0.42</td> </tr> <tr> <td data-bbox="847 405 1134 495">Cone → </td> <td data-bbox="1134 405 1418 495">0.50</td> </tr> <tr> <td data-bbox="847 495 1134 584">Cube → </td> <td data-bbox="1134 495 1418 584">1.05</td> </tr> <tr> <td data-bbox="847 584 1134 674">Angled Cube → </td> <td data-bbox="1134 584 1418 674">0.80</td> </tr> <tr> <td data-bbox="847 674 1134 763">Long Cylinder → </td> <td data-bbox="1134 674 1418 763">0.82</td> </tr> <tr> <td data-bbox="847 763 1134 853">Short Cylinder → </td> <td data-bbox="1134 763 1418 853">1.15</td> </tr> <tr> <td data-bbox="847 853 1134 943">Streamlined Body → </td> <td data-bbox="1134 853 1418 943">0.04</td> </tr> <tr> <td data-bbox="847 943 1134 1032">Streamlined Half-body → </td> <td data-bbox="1134 943 1418 1032">0.09</td> </tr> </tbody> </table> <p style="text-align: center;">Measured Drag Coefficients [2]</p>	Shape	Drag Coefficient	Sphere → 	0.47	Half-sphere → 	0.42	Cone → 	0.50	Cube → 	1.05	Angled Cube → 	0.80	Long Cylinder → 	0.82	Short Cylinder → 	1.15	Streamlined Body → 	0.04	Streamlined Half-body → 	0.09
Shape	Drag Coefficient																				
Sphere → 	0.47																				
Half-sphere → 	0.42																				
Cone → 	0.50																				
Cube → 	1.05																				
Angled Cube → 	0.80																				
Long Cylinder → 	0.82																				
Short Cylinder → 	1.15																				
Streamlined Body → 	0.04																				
Streamlined Half-body → 	0.09																				

It is the profile drag that is of interest, and this is expressed in terms of a dimensionless  $C_D$  defined as:

**Equation 1**

$$C_D = \text{Total drag force} \div \frac{1}{2} \rho u_{\infty}^2 A$$

where  $\rho$  represents the density of the fluid,  $u_{\infty}$  the velocity (far upstream) with which the fluid approaches the body.<sup>2</sup> In the exception of aerofoil or hydrofoil cases  $A$  indicates the frontal projected area of the vehicle in the direction of the oncoming flow. The denominator of the coefficient is the product of the dynamic pressure of the undisturbed flow,  $\frac{1}{2} \rho u_{\infty}^2$ , and the specified area. Being, therefore, a ratio of two forces the coefficient is the same for two dynamically similar flows, (dynamic similarity is similarity of forces. If two systems are dynamically similar then the magnitudes of forces at similarly located points in each system are a fixed ratio.)<sup>3</sup>

and so  $C_D$  is independent of the size of the body (but not of its shape) and is a function of Reynolds number.<sup>2</sup>

In the low velocities dealt with in this study, i.e. subsonic, the flows may be considered incompressible and therefore independent of Mach number effects. Effects from side, or angled, cross-winds are also neglected in this investigation, but it should be noted that these could be modelled by calculating  $C_D$  for a yawed angle range. Flow mixture of differing flow velocities and flow directions can be modelled using the Froude number as a function of  $C_D$ .

When fluid flow in a particular direction interacts with an object the fluid will begin to exert a drag force, as a result of viscous interaction upon the object. *Skin friction drag*, as its name suggests, is related to the surface roughness of the wetted areas. *Pressure drag* is more relevant to the vehicle aerodynamics studied here; this depends on the flow encountering a structure in which not every feature is parallel to the main stream. In this case a different additional drag force is recorded resulting from pressure differences over the structure, due to the structure's inherent morphology. This type of drag is also referred to as *Form drag* for obvious reasons. Thus, whereas the skin friction drag is the resultant of the forces tangential to the surface, the pressure drag is the resultant of the forces normal to the surface.<sup>2</sup> These two functions of drag can be summed together to obtain the total drag, generally termed as the *profile drag*.

In virtually all cases, apart from that of an infinitesimally thin plate, the flow separates from the body of the structure at some point. In general the structures that produce a boundary layer separation induce a disturbed down-stream eddy flow, termed the *wake*. As a result of the energy dissipated by the highly turbulent motion in the wake the pressure there is reduced and the pressure drag on the body is thus increased.<sup>2</sup> On this premise a divergence in body shape and associated drag reaction can be asserted: a *streamlined body* is one which has a very small wake and thus a decreased pressure drag, and a *bluff body* is one which has a *large* pressure drag and separation taking place over much of its surface area.

### 1.3. *Boundary layer control*

Research indicates that when considering airflow around an object such as a car, there are regions where air viscosity is important and regions where it can be neglected. In a thin layer of flow near the body surface, (the boundary layer), the effect of viscosity is important. However outside this layer, the flow can be modelled as being inviscid (i.e. zero viscosity).<sup>4</sup> While this statement holds true through much of the flow-field the inviscid-flow model also breaks down at regions of turbulence, as well as boundary layer, where even minor viscous effects are greatly enhanced. Turbulence, being present over much of the surface area of the *Discovery*, is observed in high-Reynolds flows and characterises itself by the transfer of energy to small scale motion, which is then dissipated by surrounding fluid viscosity (viscosity affecting wake formation greatly).

The boundary layer can be differentiated into two specific types, laminar and turbulent. In laminar flow airflow progresses in sheets (laminae, or layers) - in contrast turbulent flow represents a mixing within layers; flows initiate in a laminar way, and then transition to turbulent flow occurs, either naturally or as a result of designed instabilities. As was mentioned in section 1.2 the drag on a vehicle is greatly dependent on the character of the boundary layer, and especially on the separation lines. Reduction of skin friction and delaying of the separation are the two main methods of profile drag reduction. Pressure drag is the major source of drag on blunt bodies such as cars; static pressure changes lead to boundary layer detachment creating a low-pressure turbulent wake, pressure drag being ultimately due to the non-aerodynamic shape of the vehicle. Skin friction is not relevant in automotive aerodynamics, but does account for up to 60% of the profile drag in highly streamlined bodies. Clearly, much can be done to diminish aerodynamic profile drag; box- shaped geometry can be incrementally changed so that it adheres morphologically to the most streamlined shape possible - a tear-drop. This can be done by using CFD or wind tunnels and dramatic  $C_D$  reduction will be observed; but it is obviously impossible completely to remove the effects of drag, or to prevent the gradual thickening of the boundary layer, the formation of adverse pressure gradients

or separation across necessary design features. For this other methods of aerodynamic design are needed.

It has been shown theoretically that a ‘cowl’ or vane redirection can ‘reduce the drag of a blunt body (such as an aircraft engine), the external vanes allow the airflow that would otherwise shear off and create a turbulent wake, to remain forcibly attached around sharp corners’.<sup>5</sup>

Handley-Page slats and slotted trailing edge-flaps have been developed through the years; these aerofoil adaptations are similar in many ways to the turning vane concept and have allowed greater boundary layer control in aviation.

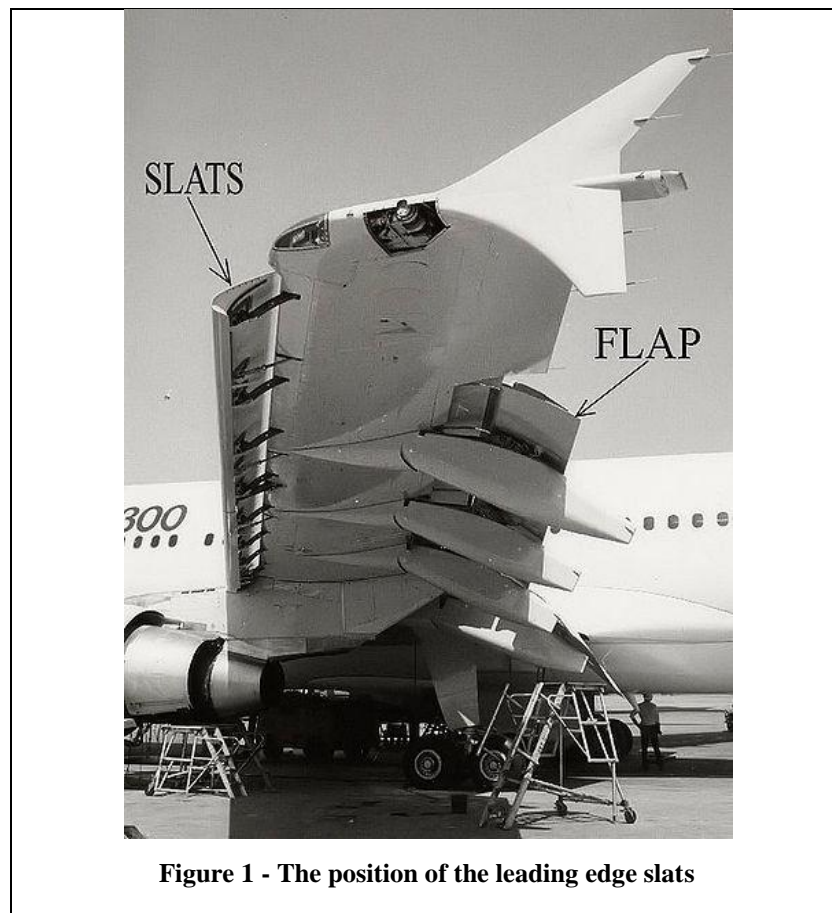


**Figure 1 - The position of the leading edge slats**

The ‘leading edge slat’ (Figure 1) acts as an auxiliary aerofoil at a high lift coefficient. The boundary layer in this case is maintained due to the strong downwash from its trailing edge. The slat forces the boundary layer to adhere to the wing and forces boundary layer attachment, or quick re-attachment if the flow has already separated.

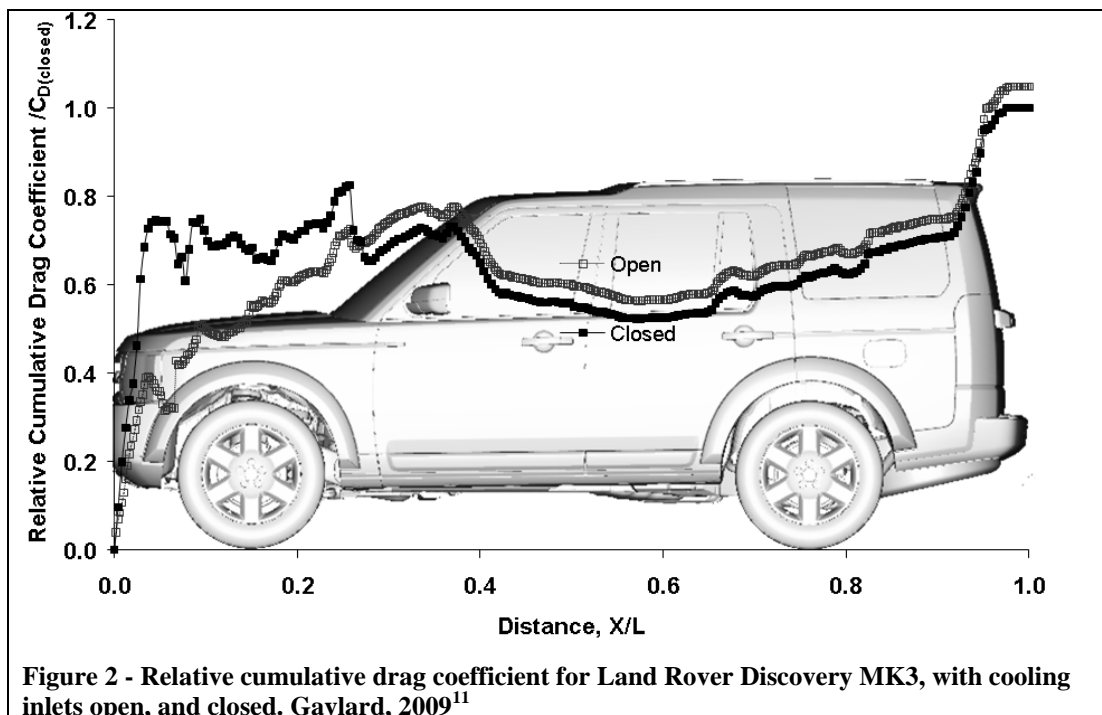
We may explain the action of the slat by saying that the circulation about it decreases the fluid velocity which would otherwise occur over the leading edge of the main wing; the rise in pressure undergone later by the boundary layer is therefore diminished and separation possibly prevented.<sup>6</sup>

The fact of separation occurring at high dynamic pressure points can be deduced from the pressure/velocity relationship described in a series of papers by Euler<sup>7,8,9</sup>. [7] concerning fluid mechanics, [8], containing the discovery of the ‘Bernoulli equation for the stream-lines’, in which Euler derives it as a result of the new general equations of hydrodynamics and [9], where Euler applies the Bernoulli equation to the problem of resistance. The results of [9] provided the, ‘Only non-trivial exact solution of the hydrodynamic equations that could be given a reasonably simple interpretation.’<sup>9</sup>. The Bernoulli Equation can be paraphrased: ‘where the flow is fastest, the pressure is least’.<sup>10</sup> As the flow passes over the vehicle surface it reaches its maximum speed (dynamic pressure) - it must subsequently slow down. As the flow slows the pressure increases, and hence an adverse pressure gradient is created. The adverse pressure gradient, acting on the boundary layer, causes the flow to separate and hence a turbulent wake is formed. This is illustrated on CFD plots as a surface dynamic pressure increase.

#### 1.4. *Improving aerodynamics*

Cars (general road vehicles) are different aerodynamically when compared to SUV / trucks – SUVs sit higher, have larger, wider, and more deeply-treaded tyres, and are larger and more ‘bluff’ in general. Bigger cars in general have bigger engines and the *Land Rover Discovery* is no exception to this rule; with a 2.7 litre TDV6 common-rail diesel engine. Larger, more powerful, engines require far more volumetric airflow being taken into the heat exchangers, for applications such as heat exchangers, turbulent flow is essential for good heat transfer and mixing, and therefore the vehicles exhibit high ‘cooling drag’ - but this may also lead to a pressure drag drop due to the bleeding away of air from the frontal stagnation point.<sup>11</sup> Heat exchanger drag / bleed situations have been neglected in this study both in terms of CFD and wind tunnel work. In the case of the *Discovery* and ‘XK’ it has been

observed that the cooling case actually leads to the stagnation pressure drop, (before re-emergence - indicating the bluffness of the vehicle itself to be the greatest drag dependent variable.<sup>11</sup>) As can be seen in Figure 2 *Jaguar Land Rover* have found that for the bluff front section of the vehicle the 'open' heat exchangers leads to a 'cooling drag' ( $C_{DC}$ ) drop, once this bluff section has been negotiated the 'open' system leads to a  $C_{DC}$  increase relative to the 'closed' situation across the rest of the vehicle. This is due to a combination of losses through the cooling system and external interference drag effects, for example: inlet spillage drag, and changed approach angle for the onset flow onto the front wheels.<sup>11</sup>



As was mentioned in section 1.1 certain shapes are inherently aerodynamically efficient (e.g. tear-drop) and only need minor adjustment to reduce the profile drag and thus to gain an aerodynamic benefit, for minimal cost. For the vehicle profile we are interested in, it can easily be seen, even by the non-aerodynamicist, that appreciable  $C_D$  decreases can be made by lowering and completely re-shaping the vehicle in question. But as was illustrated in the introduction, these issues are beyond debate and any attempt dramatically to change the vehicle in this way is completely unfeasible. Hence the morphology of the *Discovery* Mark 3 must remain the same with only minor detail change, i.e. the optimum design change must



incorporate the minimum cost, minimum physical and aesthetic change, no legal or safety ramifications, and must also bring the greatest  $C_D$  benefit - when compared to the original model.



**Figure 3 - The original Land Rover, and Bugatti Veyron, visually and aerodynamically very different**

As can be seen from Figure 3 the adaptations applicable to the original Land Rover to gain aerodynamic benefits have to be carefully weighed against the vehicle's off-road heritage. Aerodynamic adaptations have to be in accordance with the vehicle's flexibility; modifying the vehicle to be similar to the Bugatti would be changing the whole identity of the SUV, and would result in loss of the consumer base.

"We look at all areas of the car that come in contact with the air. Upper surface shape, under floor, wheels and even cooling and engine bay," says Ian Anderton, aerodynamicist at the Jaguar Design Studio in Gaydon, England.<sup>1</sup>

Steve Wegryn, manager of Ford Motor Co.'s aerodynamics department is reported to have made a prediction of probable future aerodynamic reduction devices:

- Active air dams, that lower when at high speed tarmac conditions such as motorways (air dams are in general inappropriate for SUV vehicles by their very nature)
- Active rear spoiler systems that can vary with the vehicle's speed, (although spoilers are more downforce aids and can occasionally increase drag rather than decrease it)

- ‘Easy ride’ systems that actively change the ride height dependent on terrain and/or vehicle speed, which is currently a feature on some Range Rovers, and is a possibility for easier drag reduction on the *Discovery*. Mercedes-Benz is reported to have said, “Lowering the ride height at speed results in a 3-percent improvement in drag.”<sup>1</sup>

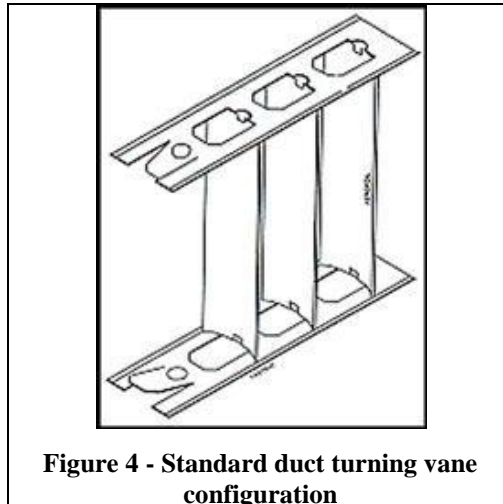
A Darwinian-style evolution of aerodynamically designed vehicles is more probable than a massive leap forward. This is the current thinking. Mercedes has been reported saying in recent years that,

"Engineers and designers are always striving for improvement, but the constraints placed on the designers by consumer tastes, practicality, legislation and production technologies will prevent giant strides."<sup>1</sup>

Other car producers have reported similar feelings on the subject, and it is probably true that vehicle manufacturers are not about to create ‘the worlds most aerodynamic car’, for which there is no market or cost-benefit necessity.

### 1.5. *Turning vane background*

Turning vanes are predominantly used in heating and ventilation systems, and are regularly seen in wind tunnels and confined fluid flow paths. The turning vanes, when applied to the above configurations, in addition to 90deg bends in piping systems reduce the loss coefficient characteristic of mitred joints. This method of using turning vanes in a mitred 90 deg turn has allowed for a more efficient loss coefficient than would normally be associated with a turn. This means that the piping bend can perform as well at a sharp 90 deg junction as it does at a smoothly-radiused transition bend (which often requires more space, more material and an inside radius of twice the duct diameter). Vanes are used in these mitred ducts to guide the flow more efficiently around the sharp corner, and are placed at the radius line of the duct junction - for a 90 deg bend the vanes would be placed at a 45 deg angle (Figure 4).



The turning vanes effectively divide up the flow that passes around the mitred duct corner, each one of the divided flows has an ideal inside radius to adhere to; the molecules in the separated flows are efficiently guided around the 90 deg turn. The external momentum change created by the vanes prevents the adverse pressure gradients observed to account for the inefficient passage of fluid in a system without turning vanes.

These duct-based turning vanes can also produce a certain amount of flow loss. Upstream sections can cause stagnation to a certain extent, and abruptly-ending vanes can prevent the flow from adequately recovering, creating a pressure drop. This ‘bluff body flow loss’ can be effectively reduced with vane adaption and modification.

### *1.6. Current turning vane applications*

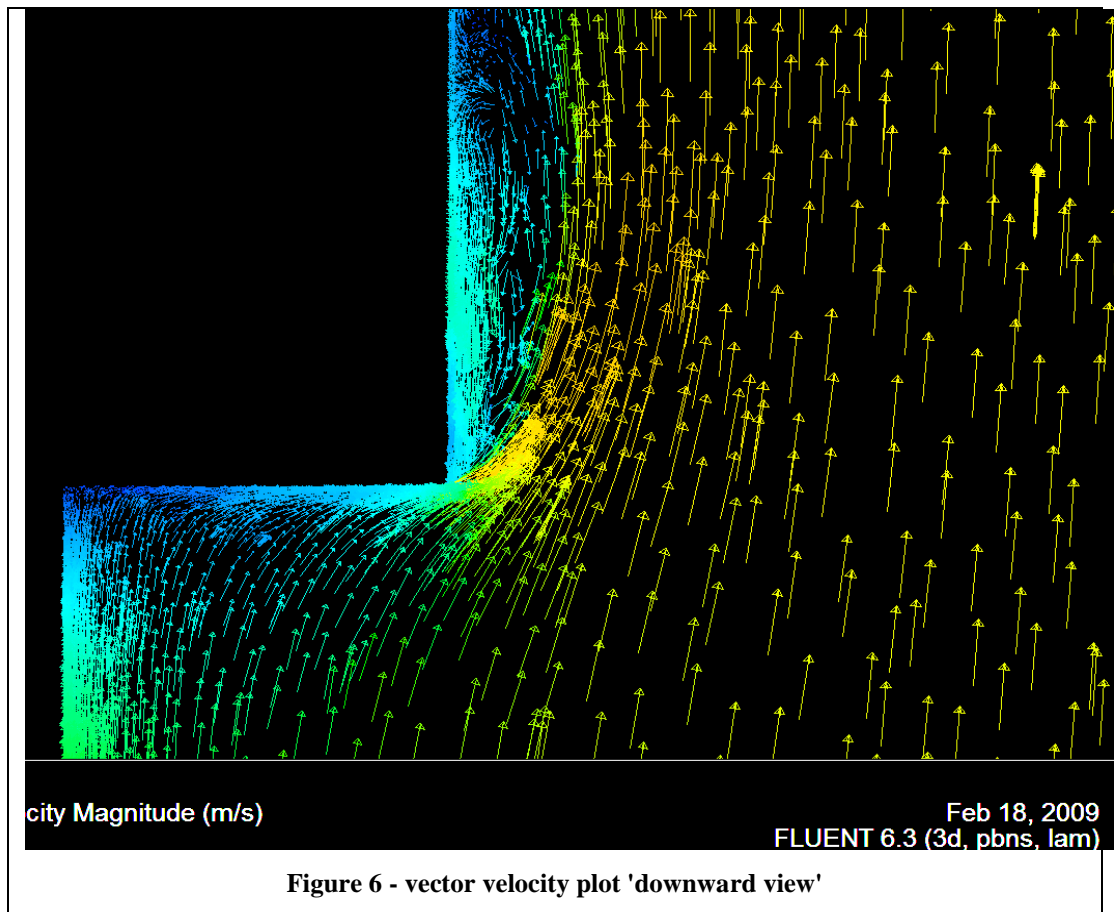
Turning vanes, predominantly side turning vanes (Figure 5), are used in 68% of all long-haul and medium-haul freight vehicles according to Dept. For Transport data<sup>12</sup>. Usually placed below the Cab window, they cover sharp edges and help to reduce build up of road film and dirt. They have an addition cost of £100 and a payback of 0.7 years in terms of aerodynamic fuel savings, (Data recorded for the average long/medium-haul freight transport vehicle).



The majority of the air passes around the exterior of the vanes and evidence suggests that any drag reduction obtained derives from the increase in the effective radius of the cab edges to a level that is sufficient to ensure that the flow does not separate<sup>12</sup>. Preliminary CFD studies have shown that an increased radius has a similar effect to turning vane inclusion on a simple brick model within *Fluent*, (Figure 6). Attached flow is also maintained and turned forcibly by the inside structure of the vane - indicating that the vane has two distinct purposes: 1<sup>st</sup>, providing a greater effective radius around a sharp corner: 2<sup>nd</sup>, delaying boundary layer separation in zones of adverse pressure gradient.

The Department For Transport lists the following turning vane points for consideration<sup>12</sup>:

- If the cab edge is sharp or has a small radius, vanes can provide a slight reduction in drag
- Suitably located vanes can reduce dirt deposition on the cab side windows or doors
- Improved cab appearance with less need for washing
- Drag can be increased if the cab edges are already well-rounded



In this simple *fluent* flow case a half model of a brick (2x2x4m) was simulated travelling at 25m/s above a ground moving also at this velocity. The brick was tested with sharp corners, rounded corners and also with corners with a front turning vane applied. The boundary layer is clearly seen (Figure 6) to be rapidly separating at the sharp corner. The pressure gradient is so adverse that the boundary layer flow has been forced to detach creating a low velocity turbulent wake. The faster moving air-flow needs to be re-attached with minimum turbulence to reduce the drag coefficient. In the sharp-angled block study the fast moving layer never reaches the re-attachment stage (due to the block's being too short) which adds to the rear pressure drop effect, effectively 'sucking' the block backwards.

In the cases pictured in Figure 7 and Figure 8, the radius case and the turning vane case both appear to decrease the drag coefficient in the same manner; through increased external radius size leading to a smooth and gradual transition and to increased velocity around the corner of the brick model. The 200mm radius case in

Figure 8 is potentially more effective than the turning vane case in Figure 7, but either solution is acceptable when compared to the sharp corner of Figure 6.

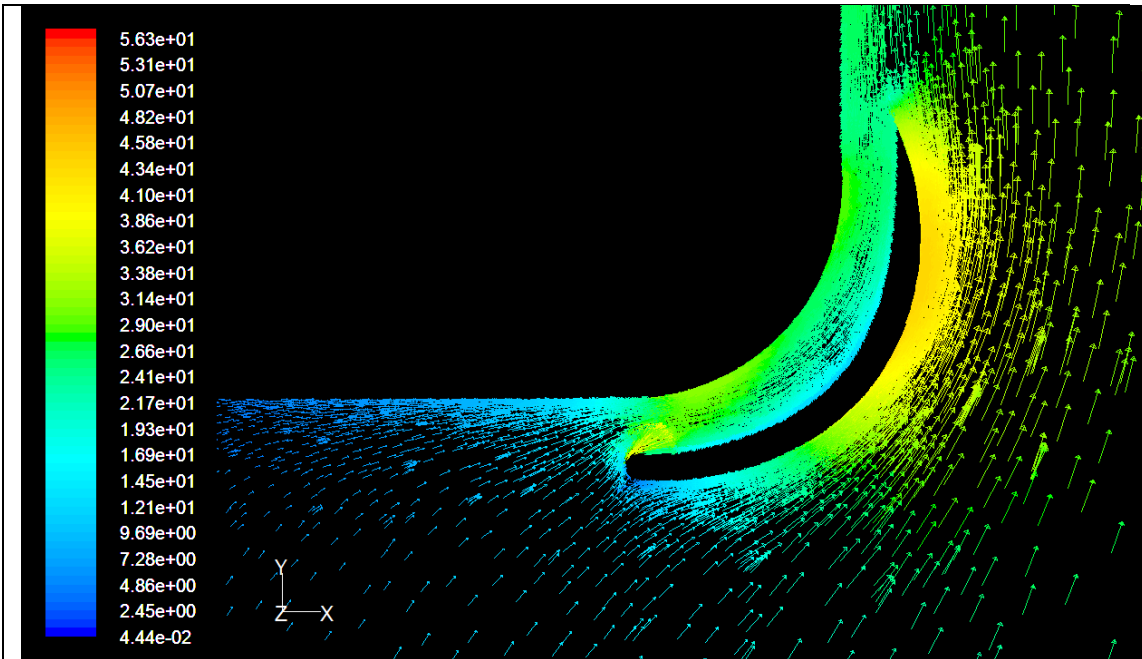


Figure 7 - Side turning vane Velocity vector plot

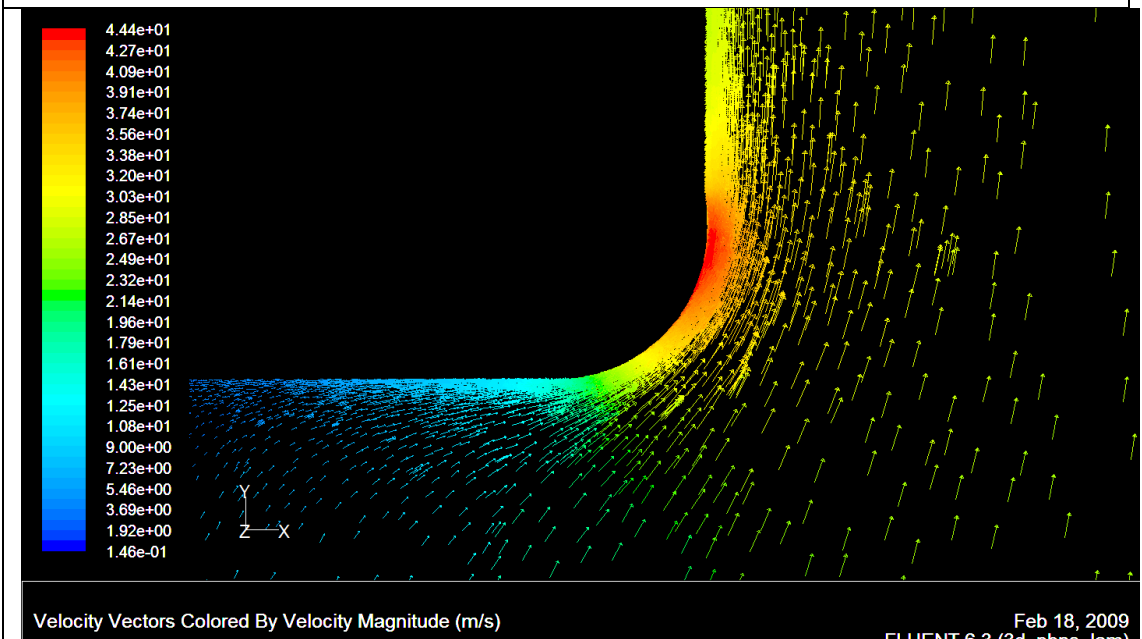
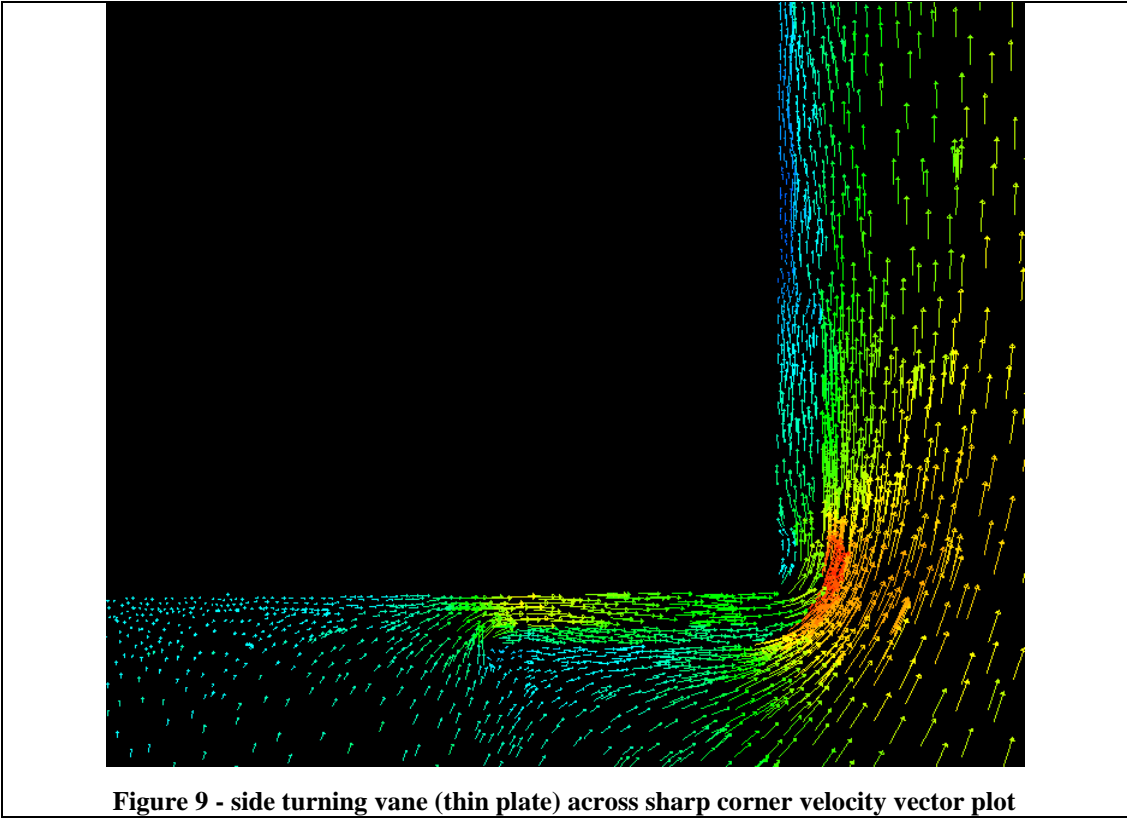
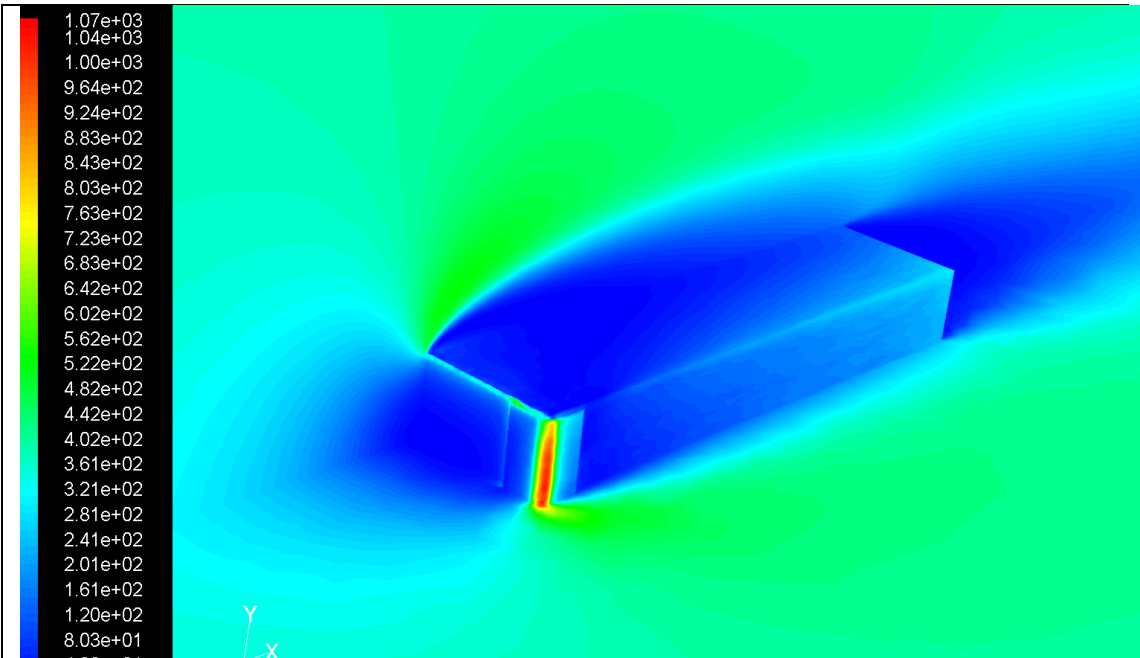


Figure 8 - 200mm fillet velocity vector plot



**Figure 9 - side turning vane (thin plate) across sharp corner velocity vector plot**



**Figure 10 - turning vane (across sharp corner), dynamic pressure plot**

**Table 2 – Block adaption data**

<b>Block adaption</b>	<b>C<sub>D</sub></b>
Sharp corner (Figure 6)	1.04
turning vane & 200mm radius (Figure 7)	0.88
200mm radius (Figure 8)	0.88
front turning vane on sharp corner (Figure 9)	0.65

As seen in Table 2 the results hinge conclusively on the extended radius produced in both the front turning vane case and the 200mm radius case. This indicates that the drag decrease produced by a turning vane can adequately be produced by an increase in external radius. This implies that for adequately rounded structures on the *Discovery* there will be no benefit from turning vane addition, and that, potentially, the addition of vanes may lead to a drag increase. Figure 9 & Figure 10 also confirm that the addition of a vane to a sharp bluff corner decreases separation and reduces recirculation caused by separation; the dynamic pressure plot of Figure 10 shows the visibly-reduced dynamic pressure wake on the side of the block compared to the wake on the top of the block where no vane has been added.

### 1.7. CFD discussion

CFD, or Computational Fluid Dynamics, is a branch of standard fluid dynamics that utilises numerical methods and specific algorithms to solve complex fluid motion problems. Similar in certain ways with FEA (Finite Element Analysis), domains are created in a pre-processor, solved in a processor (i.e. *FLUENT*) and viewed using a post-processor.

Certain boundary conditions must be applied to provide as accurate a simulation as possible; but it must also be conceded that certain parts of the insoluble [to date] Navier-stokes equation (which governs the fluid flow characteristics) have been averaged or simply represented; leading to inevitable gaps in the required information. It is important to bear in mind the fact that CFD is a *simulation* and not a ‘virtual wind-tunnel’.



According to Gaylard, computational Fluid Dynamics (CFD) simulations have the potential to provide highly-resolved representations of the complete flow field around a vehicle. However, this comes at a cost: even with substantial computing resources it is not practical to match the throughput of conventional wind-tunnels.<sup>11</sup> Although widely used, CFD by itself does not provide the full picture when it comes to drag reduction or to lift production in certain circumstances. In industry, CFD and wind tunnel use should be in collaboration, and neither tool should be used extensively in preference to the other to ascertain the aerodynamic factors of a design. Gaylard also mentions the strengths and weaknesses of CFD analysis:

Computational Fluid Dynamics - The strengths of the computational approach include:

- A practically complete characterisation of the flow around, and through, a vehicle.
- Test properties do not need to be manufactured, just defined via CAD.
- Shape changes can be precisely defined.
- Major shape changes can be made quickly (often using mesh-morphing techniques).
- Inherently high Reynolds number flow simulation.
- Easy access to data in optically obstructed regions (engine bay, under body).
- The ability to define a very low blockage domain and arbitrarily comprehensive moving ground simulation.
- Lower organisational footprint.
- Ready access to unsteady force and flow characterisation.
- Suitable for use within a Design of Experiments (DoE) or objective function optimisation framework.

However, CFD techniques have a number of well-known weaknesses:

- Capturing the effects of turbulence (there is, as yet, no general theory of turbulence. This requires the use of either turbulence models or Direct Numerical Simulation. The former methods have limitations, the latter is too computationally expensive to be viable for the Reynolds number range and geometric complexity required for automotive aerodynamics.)
- Adequately resolving, or modelling, boundary-layers.
- Correctly capturing flow separations in adverse pressure-gradients.
- Resolving vortex structures (RANS methods tend to under-predict vorticity; Lattice-Boltzmann solvers tend to over-predict vorticity.)
- Accounting for the influence of incidental flow paths and relatively small-scale roughness (i.e. tyre tread).
- Accounting for mechanical deformation of parts (e.g. tyre shape).
- Accounting for deformation of parts under aerodynamic load (e.g. wheel deflector deformation).
- Modelling laminar to turbulent transition in boundary layers (only relevant for vehicles with wings and, perhaps, aero-acoustic simulation of flow structures on external rear-view mirrors.)

The above - listed frailties of CFD indicated by A.P Gaylard in his 2009 paper, *The Appropriate Use of CFD in the Automotive Design Process*<sup>11</sup>, show that the results produced in this investigation and in other works are not without flaw, even if the inherent flaw is small. But in certain situations such as aero-acoustic simulation FEA can fill the gaps and can allow for a CFD/FEA collaboration to provide a fluid-structure interaction simulation more closely grounded in reality.

As is mentioned above there is, as yet, no all-encompassing turbulence theory.

There is a select number of models in industrial use - these models have their own frailties, and generally work on assumed constants, as was mentioned earlier. In the majority of real engineering situations, and in the analyses shown in this thesis, the flow is turbulent, changing the energy losses in the flow considerably.

Turbulence is characterised by vortices and the time dependency observed by the velocity components variation. Whole areas of physics research is devoted to

producing high quality turbulence models. The models used in this investigation are the standard k-epsilon model and also the RNG k-epsilon model (which will be discussed later in this thesis). The k-epsilon model has been used extensively for many years by aerodynamicists. It is viewed as a numerically stable method, with many applications – which indicates flexibility. The initial assumption made while using the k-epsilon is that turbulence is isotropic, generally a reasonable assumption for most flows. But as discussed later the standard k-epsilon model has been noted to perform badly in regions or flows containing swirl or extreme turbulence. In such cases (e.g. Vortex Generator analysis) the RNG k-epsilon model was initially favoured as being the most robust model to deal with the situation.

- 1) The inlet velocity is  $V_{\text{inlet}}$ , the initial inlet values of  $k$  and  $e$  are calculated as follows:

**Equation 2**

$$k_i = 4.5 \times 10^{-3} \times (V_{\text{inlet}})^2$$

**Equation 3**

$$e_i = \frac{(k_i \times 1.5 \times 0.1643)}{(0.09 \times \text{height})}$$

where HEIGHT is the flow inlet dimension (in this case the wind tunnel).

- 2) The *initial* conditions for  $k$  and  $e$  are then set in the turbulence model field in fluent using the above calculated values:

***Solve/Initialize***

The standard k-epsilon model values were applied to all analyses and is the prime turbulence model used throughout this investigation.

## 2. Computational fluid dynamic model generation

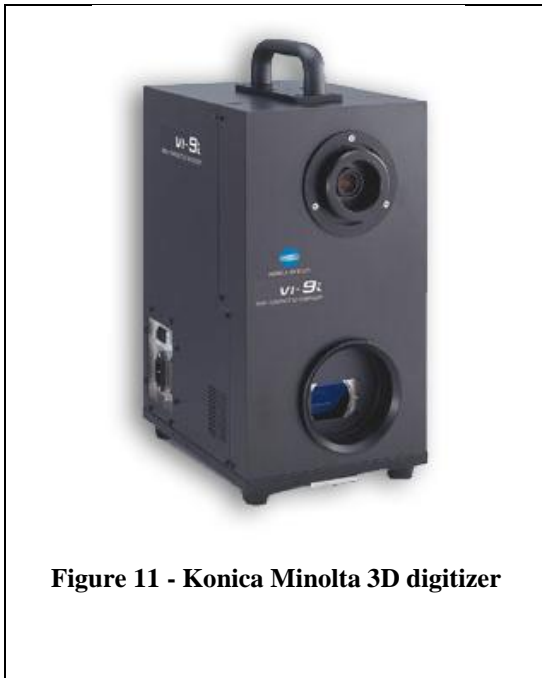
### 2.1. Geometry creation

After the preliminary simple block CFD runs, turning vanes were shown to produce a drag reduction. The aim of this investigation is to illustrate the results of turning vane shape and placement on an SUV. A 1:6 scale production-accurate model of a *Land Rover Discovery* was purchased, in order to carry out scale wind tunnel tests to verify the full scale CFD simulation. A *Konica Minolta* laser scanner (Figure 11) was used to create a point cloud (Figure 14) that was then read into *Catia V5*. The point cloud was converted into NURB surfaces (Figure 16) which allowed the adaption of the surfaced structure within the CAD package. This was then suitable for transfer (as a *.model* file) to the pre-processor program, *Gambit* and then to the commercial CFD code *Fluent*, and was also successfully re-designed in *Catia V5*, to allow for successive designs.

### 2.2. LASER scanning procedure

The 1/6<sup>th</sup> scale model of the *Land Rover Discovery* mark 3 was initially purchased to perform wind tunnel tests on. It was agreed that this was the most accurate model to scan into the computer, so preparations were made to the body work and chassis to allow for accurate laser reflection and appropriate surface creation.

Scanning was done using a *Konica VI-9i* non-contact 3-d digitizer (Figure 11). This is a free-standing scanner suitable for scanning large objects at variable distance, accurate to 50µm. It is ideally suited to a number of applications, from the medical sphere to a design verification process such as this.<sup>13</sup>



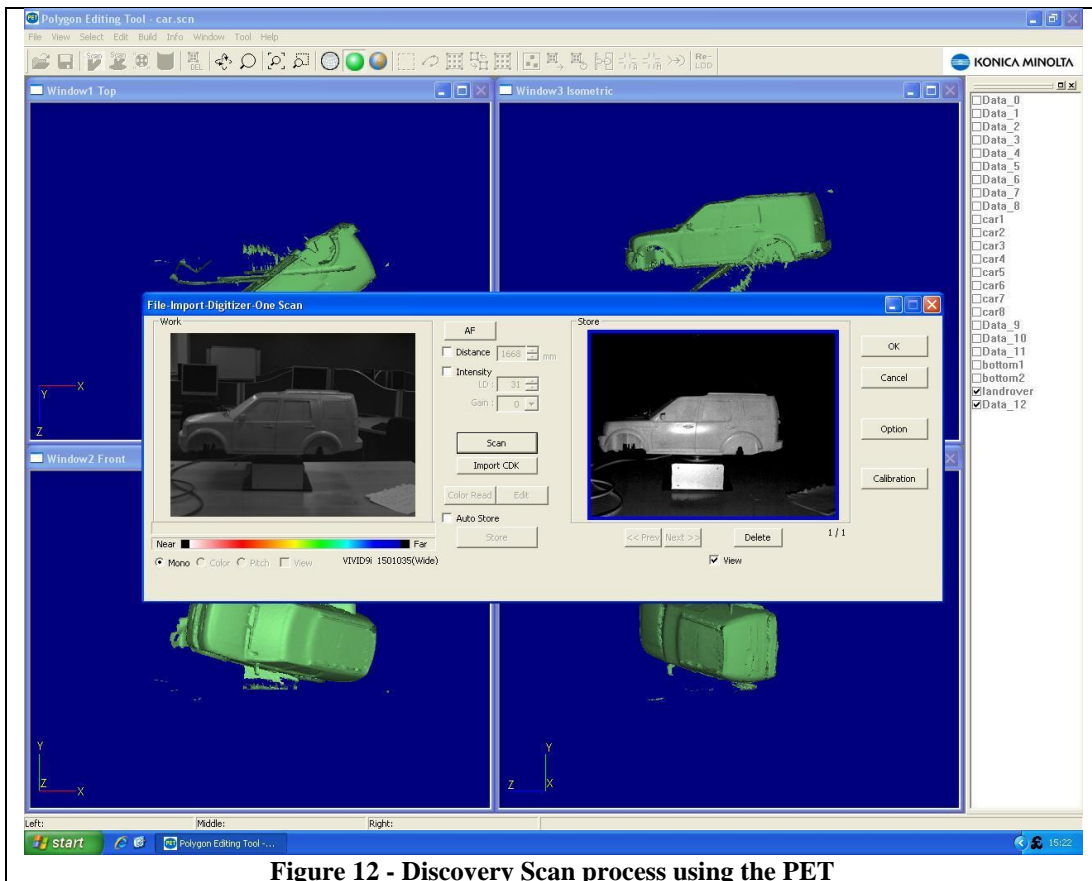
Konica Minolta non-contact 3D Digitizers are based on the principle of laser triangulation. Objects are scanned using a laser light stripe. The light reflected from the object then enters the CCD camera of the VI-910. The distance to the object can be obtained by the angle of reflection of the laser, the angle of incidence of the reflected light from the object into the CCD and the fixed distance between Laser and CCD camera.<sup>13</sup>

The wheel system was removed (this was scanned separately at a later date), and the body work was spray-painted with a light-coloured matt finish model spray paint.

The original colour and finish of the model *Discovery* was completely undesirable, (black, and reflective); due to the laser scan method any surface that absorbs all light (e.g. black) and any surface that has a sheen will yield poor, if any, data.

The spray-painting was conducted using appropriate masks and safety precautions in an external area using environmentally friendly model paint.

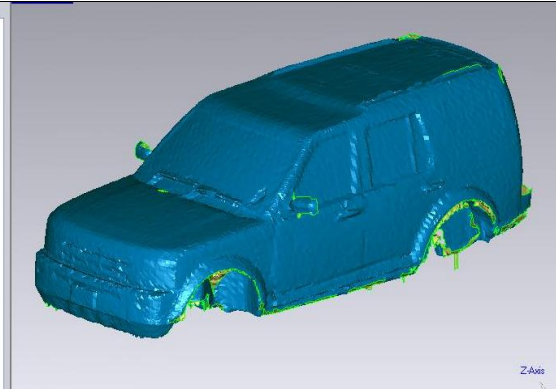
Once all reflective areas of the vehicle (and wheels) had been sprayed work was carried out to secure the chassis to the body work using masking tape to cover gaps left in the chassis by the removal of the wheels. The masking tape was also used to line the inside of the wheel arches and to remove the unwanted detail on the underside of the chassis; the tape was picked up well by the scanner - being a light-coloured matt texture.



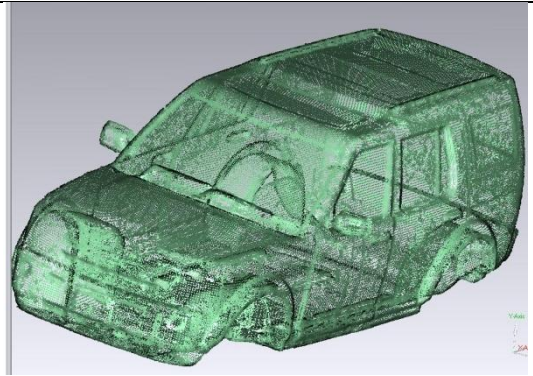
**Figure 12 - Discovery Scan process using the PET**

Figure 12 shows an initial group of *Discovery* body work scans grouped together, before the tape was applied. The later more accurate scans had a taped chassis and also the model was placed on a black reflective film, to cut out unwanted ‘noise’ data from the table/stand.

The final scan contained ~60 scans of the body work and chassis and ~15 scans of one wheel that was later duplicated and added to the CAD model.



**Figure 13 - Initial Geomagic point cloud triangulation (before surface creation)**



**Figure 14 - Highly detailed point cloud recovered from Konica Minolta scanning and stitching using the PET**

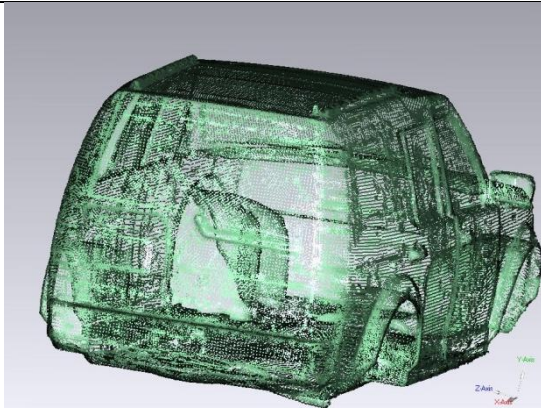


**Figure 15 - Rear view**



**Figure 16 - Initial NURBS surface creation in Geomagic**

The *polygon editing tool* was used to create the point-cloud shown above via a stitching process of the scans. Each scan was taken at  $\sim 20^\circ$  intervals turning the car through  $360^\circ$  (using the bottom of the chassis as a datum); the same process was repeated through pitch and yaw, using the same datum. This method produced a lot of images, but the repeated data on the previous scan allowed for accurate supplemental scan-stitching, and eventually a highly detailed point-cloud. This detailed point-cloud can be seen in Figure 14 and Figure 15, at this stage unnecessary data was removed via the deletion of data points, e.g. in the windscreen wipers, in order to simplify surface creation.

This led to a successful concurrent engineering process with regard to the simulation aspect of this project, and to the usage of leading industrial standard design and validation software.

### 2.3. Manual surface creation

Once the valid scan information had been collected using the Konica Minolta scanner, the data had been cleaned of unwanted ‘noise’ data, and had been stitched together using the *PET*, the point-cloud data was then exported as an ‘.igs’ file to ‘*Geomagic*’.

The point-cloud data is all very well and good, but completely useless without ‘NURBS’ surfaces. NURBS are what all CAD programmes work on (including *Gambit* and *Fluent* CFD programmes).

NURBS stands for Non-Uniform Rational Bézier-Spline. NURBS in relation to a 2D surface means, ‘create curves with respect to control points and lines defined by the triangulation of the point-cloud derived from the *PET*’.

Problems arise when the data reaches high complexity. The more complex the surface (i.e. the multiplicity) the more the knot vector has to increase and the more the number of NURB patches has to increase.

Both *Catia V5* and *Geomagic* have point-cloud NURBS surface creation work benches, but after investigation it was found that *Geomagic* was the dedicated industry leading tool.

Tests were done in each programme using the auto-surface function, turning the point-cloud into a series of NURB patches (which would then be exported to *Gambit*) and, ultimately, a 3-D surfaced vehicle.

In both programmes, however, it was found that the patches created were highly irregular and were difficult to mesh. Additionally, when the surfaces were applied much of the detail on the surface of the car was lost. Figure 17 & Figure 18 show the resulting patch layouts:



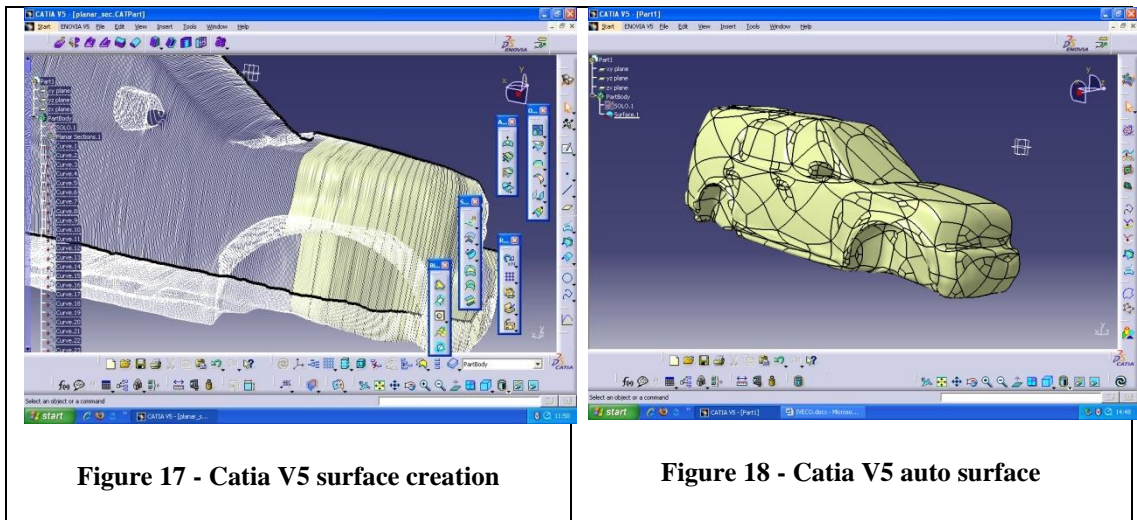
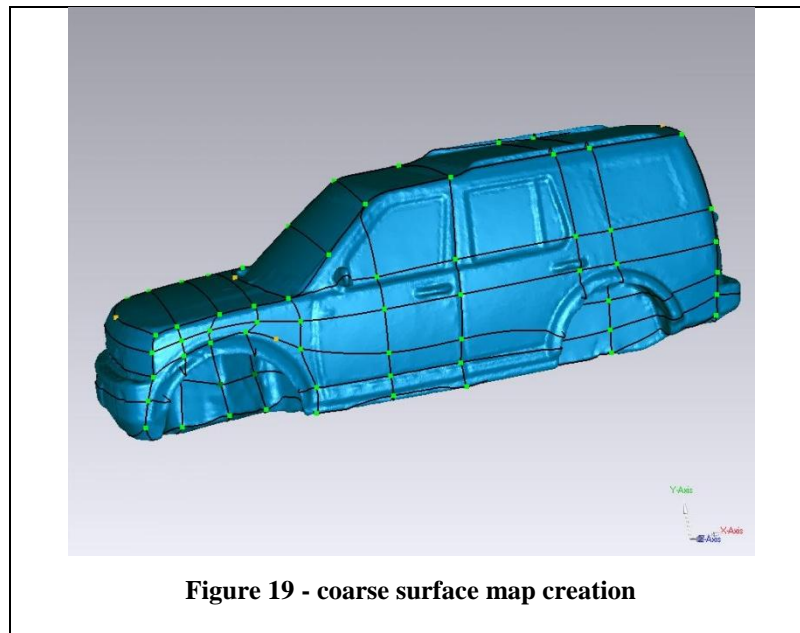


**Figure 17 - Catia V5 surface creation**

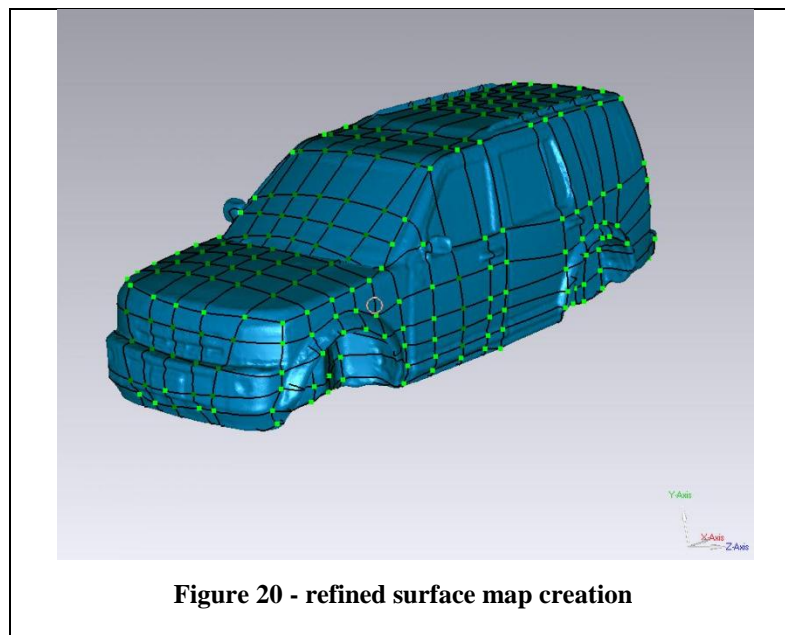
**Figure 18 - Catia V5 auto surface**

In each case, over 1000 patches were created. It was felt that this would be unsuitable for the remainder of the project. Further work was done to verify that the laser-scanned model could be used for analysis. The *Catia* model was initially chosen, as more detail was retained in this model, and attempts were made to alter the patch shapes and to mesh the model in *Gambit*. It was time-consuming to repair the model in *Gambit* to the point where a mesh could be applied. However, it was successfully meshed, verifying that the laser-scanned model was likely to be the most successful approach to geometry creation.

As the model would undergo many alterations later in the project, in order to improve the accuracy of the model and to shorten the time taken to apply a mesh, it was felt that manually creating a patch layout was necessary. *Geomagic* was used, initially with very large patches, as larger patches are simpler for applying a uniform mesh. The initial layout is shown in Figure 19 :



The original manual patch layout is shown in Figure 19. These patches contained too much detail, meaning that it was lost when NURBS surfaces were applied. The patch number was increased in Figure 20 to allow more detail to be retained. The patches were carefully aligned with main vehicle features.



Following this stage, *Geomagic* automatically applies a mesh for each patch that has been created. The surfaces are then laid over the meshes, creating a usable model for

CFD. Square patches were used so that these meshes did not overlap at any point. The grid pattern also significantly reduced the number of skewed elements in *Gambit*.

### 2.3.1. Wheel scanning and surface creation

The wheels were scanned using the same process as described previously (Figure 21). The same process was followed for manual patch creation, keeping square faces to avoid meshing errors in *Gambit*. The detail was retained in the spokes of the wheel as it was felt that these areas might affect the drag of the wheel as it spun. Each wheel contains 155 faces, adding a significant amount of complexity to the model.

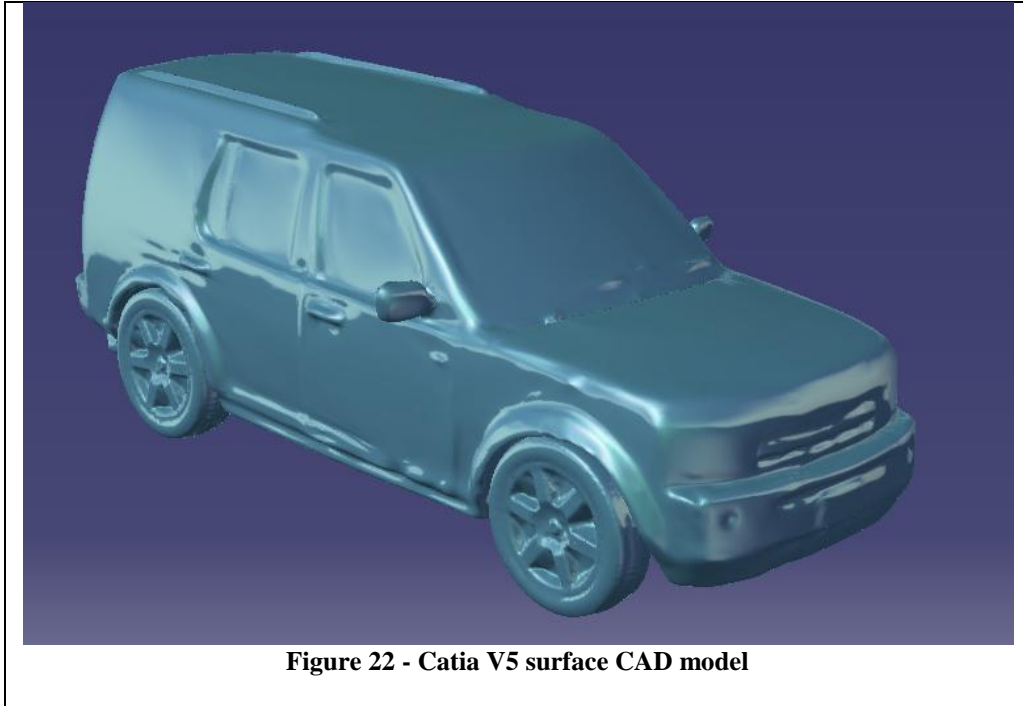


**Figure 21 - scanned wheel**

The tyre tread and spoke detail has been retained to show the effect of wheel profile on the overall drag of the vehicle, in order to improve realism. These details have been indicated in drag increase, leading to the inclusion of ‘racing rims’ by many sports car manufacturers.

#### 2.4. *Final model discussion*

Figure 22 shows the final *Catia V5* CAD model produced. Parts of the model were simplified for ease of meshing and economical solving time; the adaptations were executed at the point-cloud stage, excess windscreen-wiper detail and wing-mirror details were removed for the CFD model.



The ‘*Surfaces*’ work bench was utilised in the manipulation of the SUV model. This work bench is used in aeronautical design and allows for the creation of flowing surfaces that can easily be exported to CFD / FEA programmes. *Generative shape design* allows for complex surface design and modification, and allows for complex drag-relieving designs and ideas to be effectively and realistically tested in leading edge CFD packages.

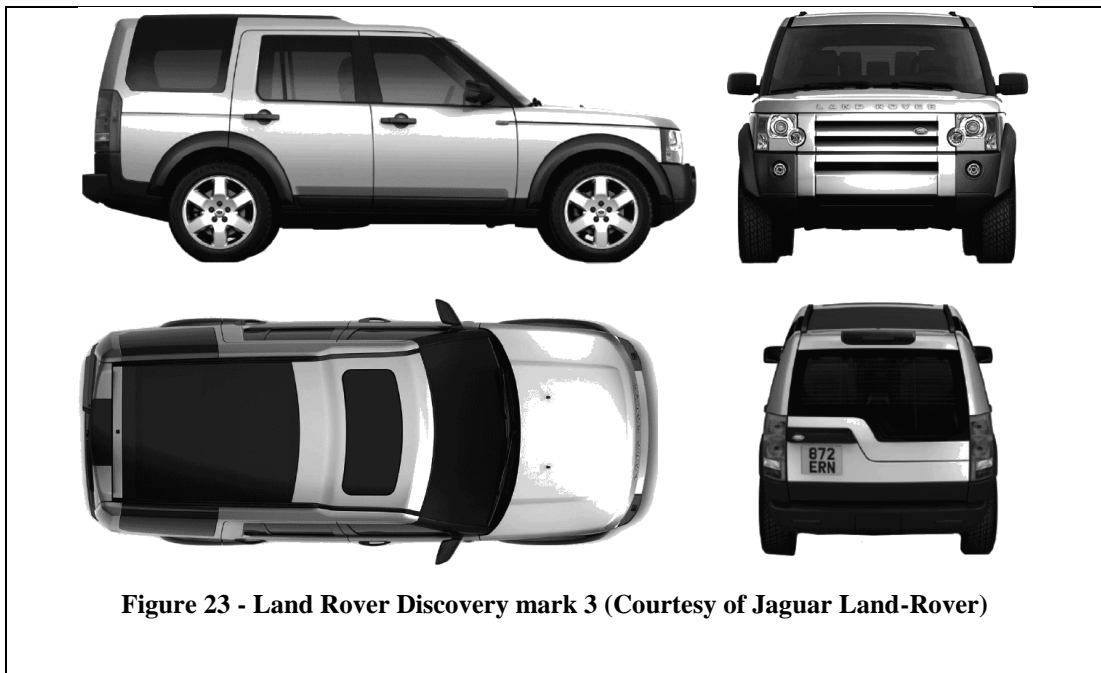
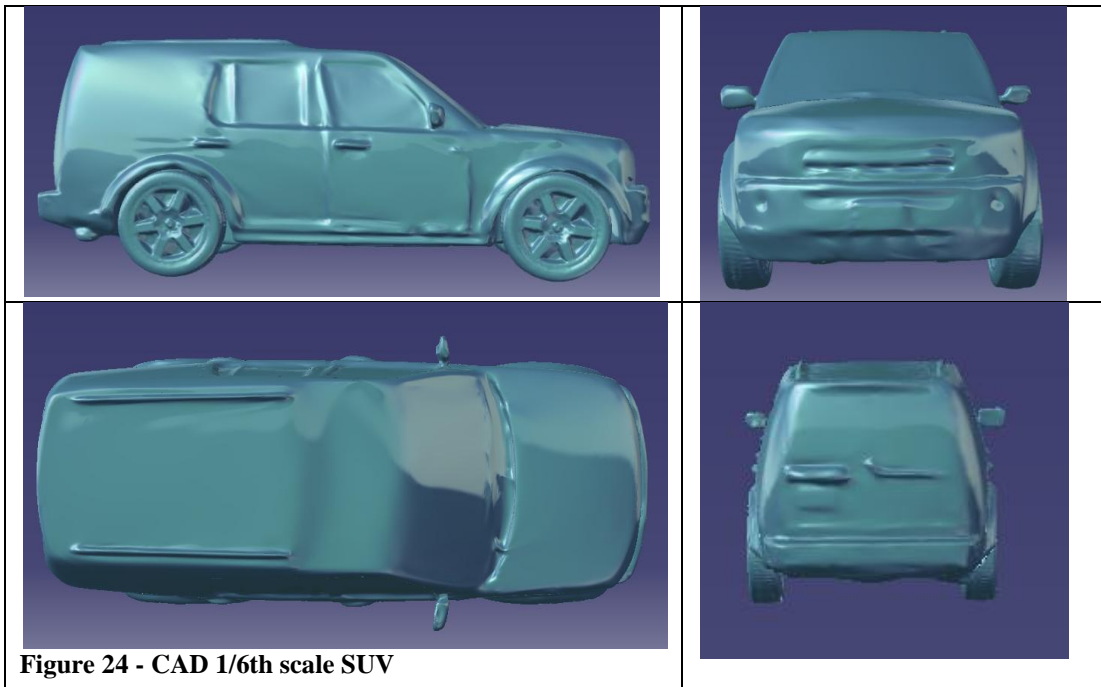


Figure 24 shows the CAD model obtained from the Laser scanning. This model is fully capable of adaption and redesign within the CAD programme, and allows a reasonably accurate and transferable *fluent* analysis model, which can easily be imported. CAD and *Discovery* vehicle morphology can be seen to compare reasonably when comparing Figure 24 with Figure 23.



CAD geometry is 1:6 scale, *Fluent* allows for simple re-scaling to full size for detailed CFD analysis. Note that the car is a closed system and inlets have been shut.



### 3. Meshing, simulation and experimental design

#### 3.1. Meshing technique

All the Computer modelling in this investigation was to aid the creation of a valid CFD model in *fluent*. The CFD model produced for this project was created to represent the *Land Rover Discovery Mk 3* (Figure 23), but also to be simplified to the extent that runs were conducted smoothly, accurately, and economically with respect to time in *fluent*.

It is common practice to create half-models for CFD runs, halving run time. It was found that creating a half model of the *Land Rover Discovery* was simple; using the *Boolean remove* function with respect to the control volume produced an accurate half model (Figure 25).

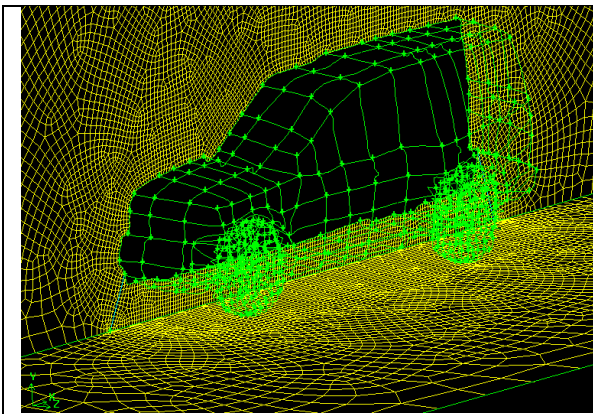


Figure 25 - graded shell mesh control volume

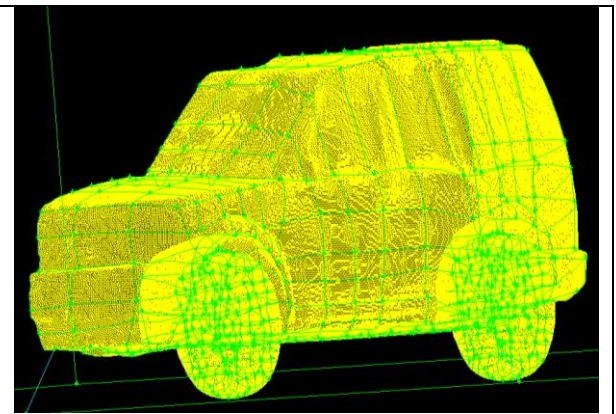


Figure 26 - 3mm fine mesh geometry (shell)

The finest mesh was used, following wind tunnel mesh convention, with respect to vehicle velocity (25m/s), (Figure 27).<sup>14</sup> The use of a large control volume (Figure 28) necessitated mesh grading, large cells being refined to small cells on the vehicle surface. High  $C_D$  values were obtained in early simulations and were the result of a coarse mesh, applied to a vehicle within a control volume that was limiting surrounding airflow. The inlet and outlet boundaries of the earlier computational domain were too close to the model which caused a non-uniform flow-field at the boundaries. The optimum simulation was refined using the following method: TGrid tet-mesh was used to mesh the control volume after the surfaces of interest were accurately meshed using the finest mesh in the study (Figure 26). The surrounding control volume was graded using the edge mesh function; growth rate

was closely monitored and set at no greater than 20% to allow for a gradual size increase in the important areas.<sup>14</sup>

It is important that the surface mesh is suitable enough to represent and to resolve all the details of the geometry in addition to satisfying the physical requirements of the study. For the *Discovery* model it is important to realise that form drag is dominant over skin friction - which implies that the accuracy of the drag and lift predictions depends greatly on the accuracy of the static pressure effect on the vehicle.

$Y^+$  is a non-dimensional wall distance for wall-bounded flow; it is commonly used when describing boundary layer theory. The  $Y^+$  value depends on which part of the boundary layer is being investigated:

- 1) the laminar sub-layer ( $Y^+$  less than 5)
- 2) the blending region ( $5 < Y^+ < 30$ )
- 3) the log-law region ( $50 < Y^+ < 500$ )

A  $Y^+$  value close to the lower bound ( $Y^+ \approx 30$ ) was most desirable.<sup>15</sup>

For high Reynolds number flows, such as that around a vehicle body, the laminar sub-layer analysis is virtually impossible due to the prohibitive cell numbers needed to model the near wall situations accurately. The log-law  $Y^+$  value was used and grid adaption in *fluent* was used to ensure a  $Y^+$  value which economically represented the boundary layer. This was particularly important in areas close to the wheels, and near-wall areas.

The grading system of TGRID allowed for a fine surface mesh to be allocated (see Figure 27) which then graduated into a coarser surrounding mesh. The degree of resolution was found to be appropriate with regard to the amount of detail on the geometry.

Figure 27 shows a method for graphically determining an average element size based on free stream velocity. 3mm element size was assigned to all edges of the vehicle. To insure adequacy of the geometric resolution of mesh, and the representation of actual geometry and key surface detail, a number of mesh quality and process checks were carried out:

- Make sure that a particle coming from the inlet area and following a path to the front stagnation point of the car would have to pass through minimum 100 cells. If this region is under resolved, the pressure coefficient will go far beyond 1 and spoil the overall solution.
- Check that the largest cells within the flow domain are smaller than those attached to the bounding box (for pure tetrahedral meshes)
- Check that Quality of cells is below 0.9 for the whole domain. It is recommended to have a quality of below 0.85 for prism elements on the car surface. Use TGrid's Mesh Repair functionalities to fix local quality problems<sup>14</sup>

In summary the surface mesh should be non-uniform triangular high quality elements, resolving all radii well and representing geometric features accurately. Areas of basic detail can be meshed using coarse elements.<sup>14</sup>

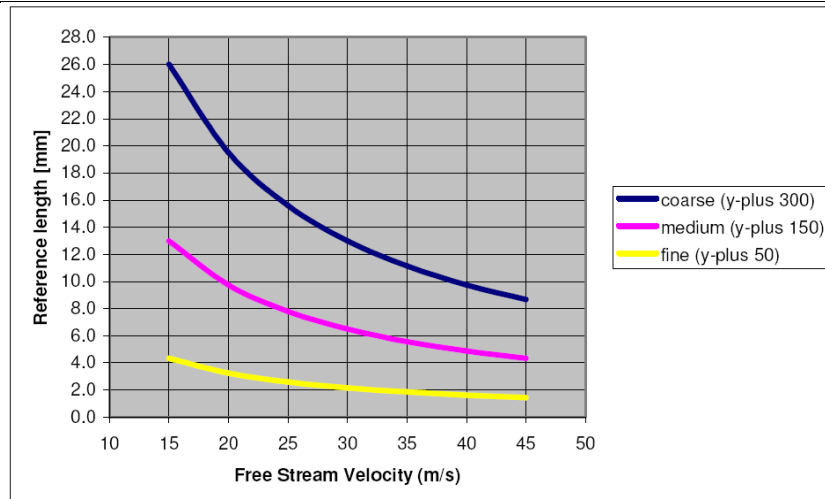
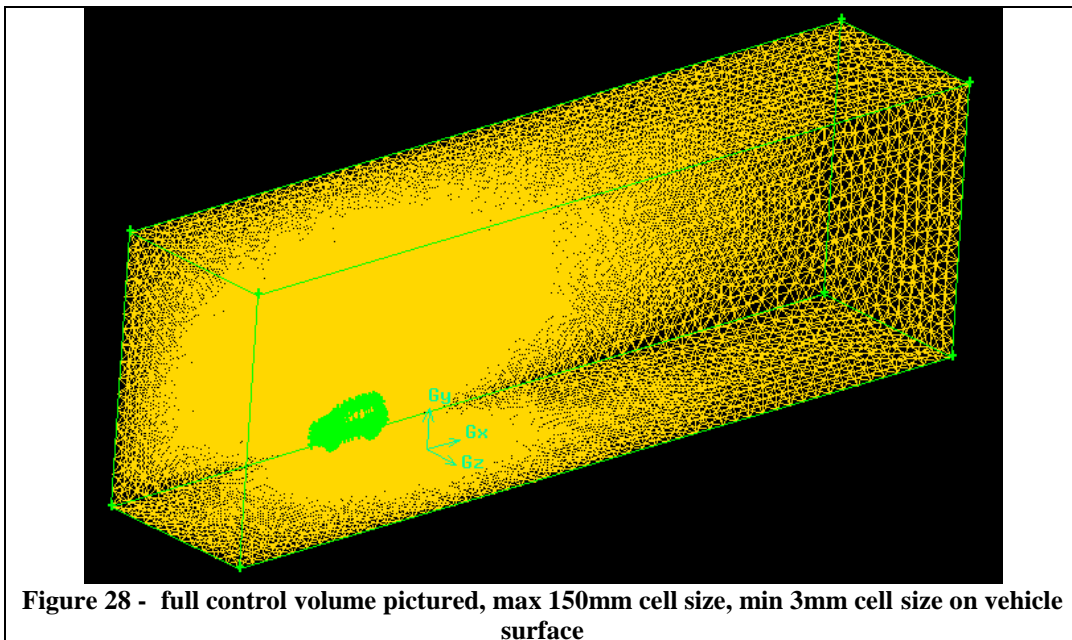


**Figure 27 – Graph estimating surface mesh reference length Lanfrit (2005)<sup>11</sup>**  
*The graph above indicates mesh sizes with respect to flow velocities. A mesh size of 3mm was selected for the vehicle surface, in order to decrease vehicle angularity and to increase the CFD accuracy.*

This grading system was important as it proved impossible to create a mesh size that would be convergent with respect to the accuracy of the results, the time taken for analysis, and adequate size of control volume. Average run time was still approx. 14 hours per analysis, using a moving ground plane and accurately rotating wheels. CFD is always subject to some constraints. Among these constraints are: available RAM, total amount of CPU time and expected response time for results.<sup>14</sup> The convergence criteria of the residuals was set at  $1e^{-5}$ , for all residuals, using standard



k-epsilon turbulence. Residual reduction to this point was the main criteria and a converged result was one deemed to be no longer fluctuating. If the residuals continue to adapt and vary beyond the convergence criteria cut-off zone, then the solution is effectively still changing. The use of TGRID allowed areas of detail (e.g. the car body) to be finely meshed, gradually growing out-wards into a coarse volume mesh. Agreed best practice dictates that a coarse mesh consists of approx. 2-4 million cells, a moderate one 10 million, and a fine one >10 million. Figure 28 has approx. 2.2 million cells, and shows refinement in areas of interest and coarse cell arrangement towards the control volume boundaries. According to agreed best practice for vehicle simulation<sup>14</sup>, the size of the domain for the external aerodynamic analysis of a vehicle should be at least 3 vehicle-lengths in front of the vehicle and 5 vehicle-lengths behind. With reference to data gathered on vehicle analysis the vehicle should not be greater (in cross-sectional area) than 1 – 1.5% of the total control volume's individual surface area.<sup>14</sup> With this standard working data, the control volume (Figure 28) had dimensions of; length 8m, height 2.5m, breadth 1.6m. The whole area can easily be scaled to actual size in *fluent*. All *Fluent* runs were carried out in actual vehicle 1:1 scale. Wall boundary zones were created for both the front and rear wheels and the wheels were set to rotate at an angular velocity of 67.204rad/s, which relates to the transitional mesh of the road and the immersing fluid velocity (i.e. 25m/s).



Sharp angles were noted between the wheel and the ground plane; mesh grading and the inclusion of small elements decreased the number of skewed elements between ground and tyres. The use of an excessively fine mesh near the walls was avoided, because the wall functions would cease to be valid in the viscous sublayer<sup>15</sup>.

A recommendation for max cell size again derives from vehicle aerodynamic best practice, and the length of the control volume, is generally 100-200mm.<sup>14</sup>

The elimination of skewed surface mesh elements led to the automatic generation of cells using the auto-volume mesh functionality of TGRID.

### 3.2. Car half-model with RNG k-epsilon turbulence

The RNG turbulence model in *fluent* is a feature that can conduct a turbulent viscosity model with greater accuracy and greater reliability, for a wider class of flows, than the standard k-epsilon model can. The aerodynamics of the *Discovery* contain a variety of different surface shapes, and thus form drag differs across the surface of the car; the standard k-epsilon model only accounts for a fully turbulent situation, whereas the RNG model significantly improves accuracy for strained flows (via an addition to the epsilon equation) and also for turbulent swirling flows.<sup>15</sup>

Low-Reynolds-number effects are accounted for, as are high Reynolds effects, increasing accuracy in the attached and un-attached boundary layer regions of the vehicle form. The RNG model is viewed as a statistical refinement to the standard k-epsilon model.

‘Improvements obtained from the RNG k-epsilon model were attributed to the better treatment of near-wall turbulence effects’<sup>16</sup>

As was mentioned earlier, the RNG adaption was found to yield a more robust solving method when highly turbulent flows were encountered such as the flow pattern produced by vortex generators. Having said this it was found that the RNG model slightly increased convergence time - and led to a lack of ‘complete’ convergence on some iterations. RNG initially improved robustness with skewed elements, but once skew had been eliminated by element refinement, standard k-

epsilon was favoured in all analyses due to its better convergence level in a shorter time.

## 4. Computational fluid dynamic Results and Analysis

### 4.1. Datum model analysis results

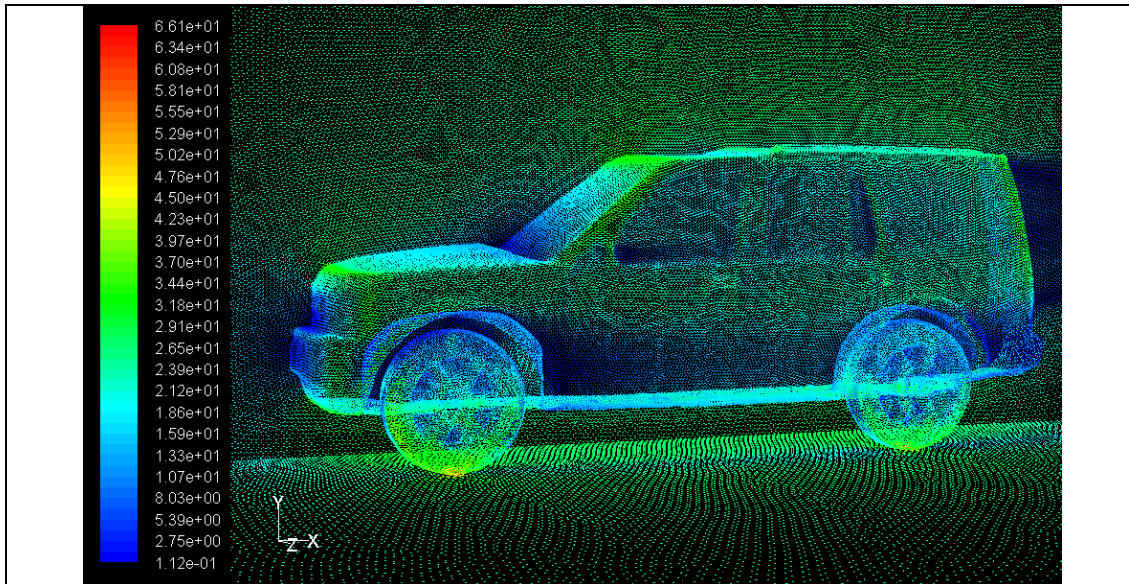


Figure 29 - vector plot showing fluid velocity

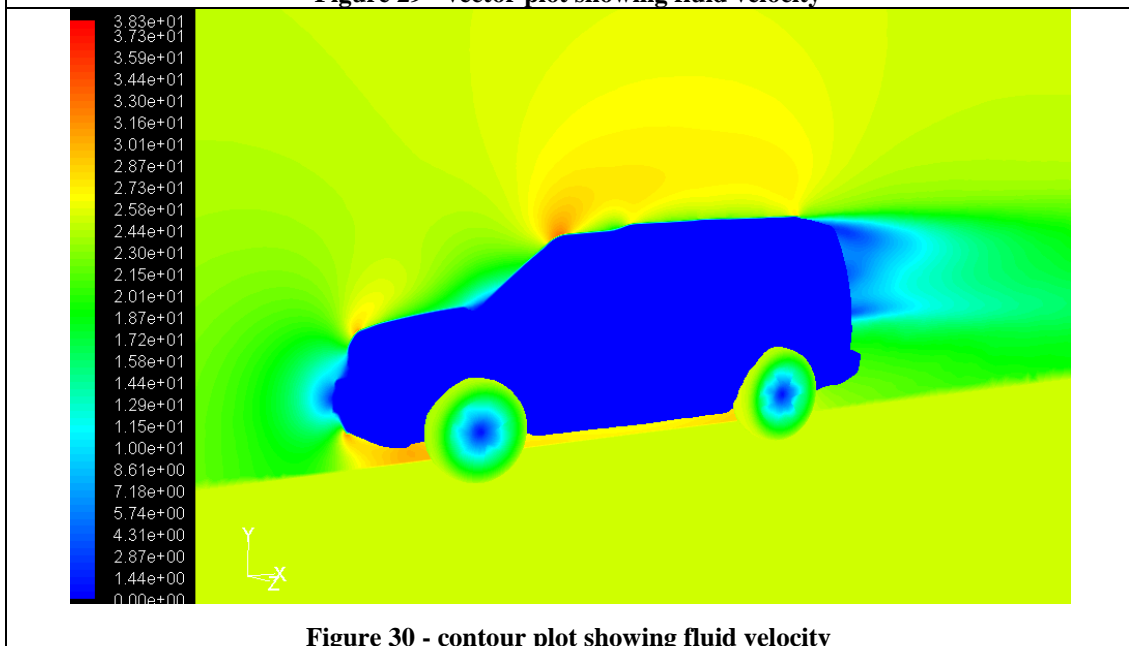
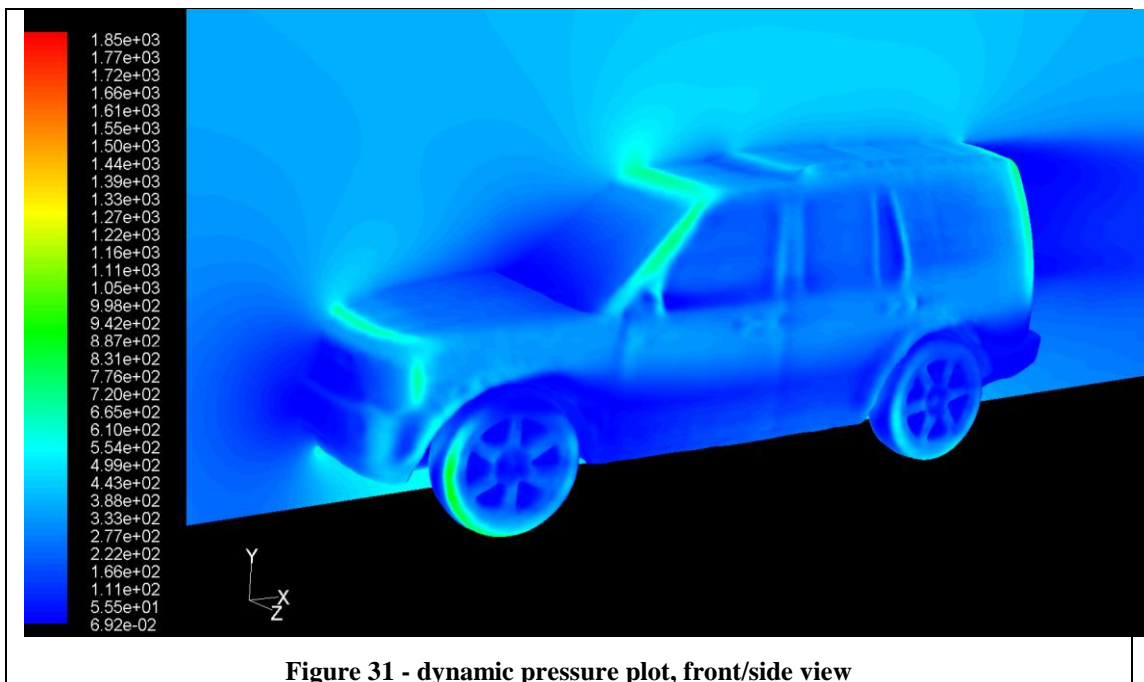
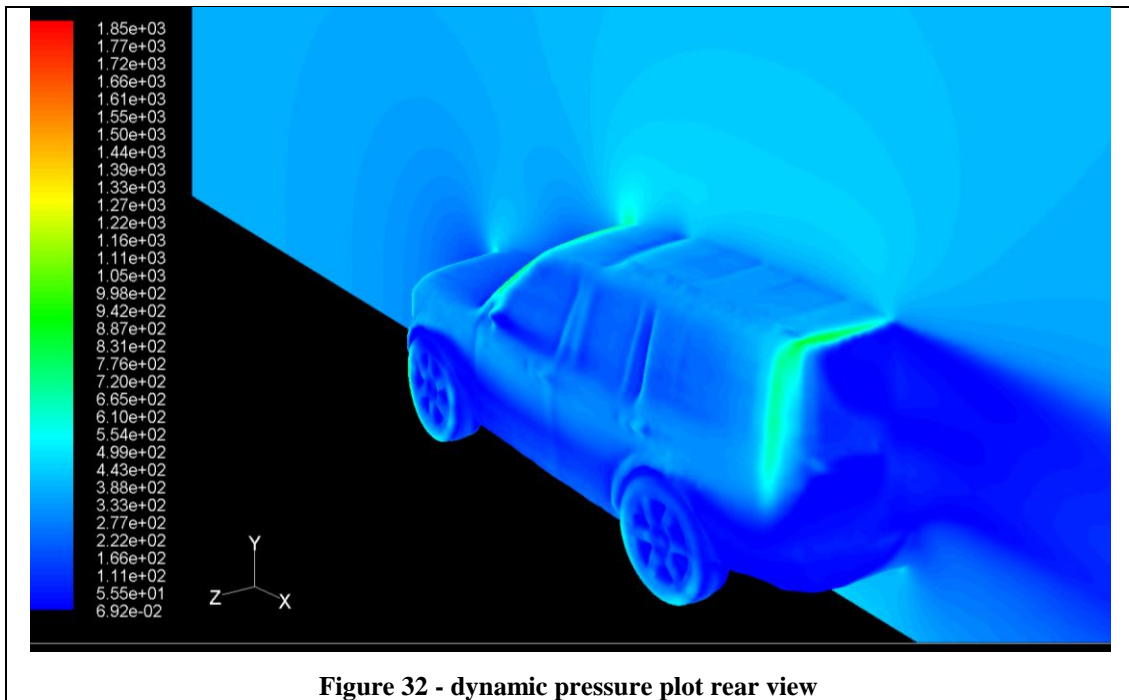


Figure 30 - contour plot showing fluid velocity

The initial fluent solution carried out was named the 'datum' and the model used was that originally scanned into the computer, and scaled to actual size. This first run gave a base line for adaption and refinement via cumulative trial and error. The full-vehicle vector plot shown in Figure 29 illustrates with greater clarity the high and

low velocity fluid areas; bluff front, the wheels and the wind screen pillar. The low velocity zones are seen predominantly behind the front wheel arch and at other points that halt or restrict air velocity. High static pressure low velocity fluid pockets could be bled to decrease drag. When comparing the velocity vector image (Figure 29) with the dynamic pressure images (Figure 31 & Figure 32) the areas of low fluid velocity and high dynamic pressure can be seen (this is obviously drag producing). Areas of high fluid velocity preceding higher pressure (as seen on the wind screen roof junction and also the windscreen pillar area) are main indicators of possible adverse pressure gradients downstream, leading to a detachment of the boundary layer. Turning vanes in these areas should produce an aerodynamic bonus to the vehicle. It can also be seen that the turbulence of the front wheel is producing a wake that prevents the air flow from taking advantage of the streamlined central door section. The air-flow over the door section is low velocity and re-circulating, indicating a significant delay in boundary layer re-attachment after the front wheel turbulence.





**Figure 32 - dynamic pressure plot rear view**

The wheels are turning from the centre points (Figure 30), the main body of the car is seen to be static - due to the airflow moving past the stationary car, as per standard wind-tunnel simulation<sup>14</sup>. The velocity vector plot (Figure 29) shows the fluid path lines across the surface of the vehicle.

**Table 3 – Datum model data**

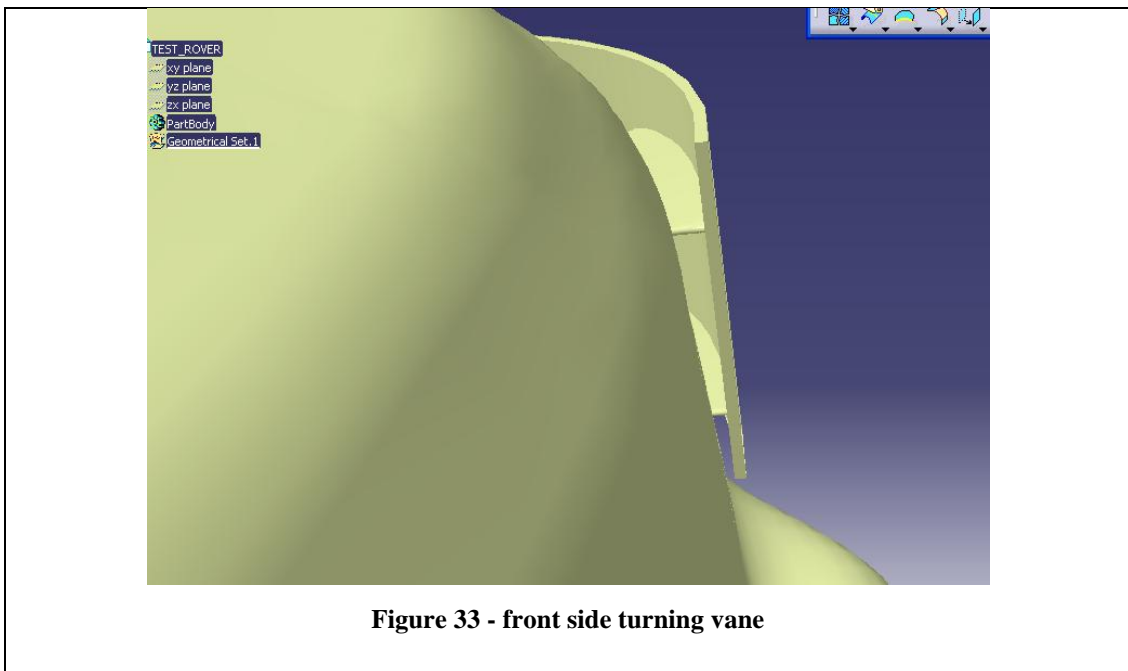
Projected area (A)	1.55 m <sup>2</sup> (half model)
Drag force (F <sub>D</sub> )	249.77 N (half model)
Coeff. Drag (C <sub>D</sub> )	0.42

The C<sub>D</sub> (Table 3) was slightly higher than first predicted in published data for the *Discovery* in a non-heat exchanger flow model usually quoted as 0.41 for open systems<sup>11</sup>. All internal flows in this study have been shut. Cooling flows could be considered to provide a fixed zero-yaw delta. In certain areas of the vehicle turning vanes could affect the processes of heat exchangers, and actively increase drag, or exchanger performance. This model was used as the ‘datum’ base study and % increase or decrease of C<sub>D</sub> was assessed with regard to this rotating wheel model.

## 4.2. Applied drag reduction design results

### 4.2.1. Bluff front side vane

The image in Figure 33 shows the front side turning vane design, placed just above the front bumper near the light block system. The design was intended to capture the separating boundary layer associated with the bluff front section of the vehicle, and smoothly to maintain the air flow in that region. In a similar way to the HGV turning vane pictured in Figure 5, the external surface of the vane allows for a gradual ‘sweep’ around an otherwise ‘sharp’ corner.



The side vane in Figure 33 did not have the desired affect during CFD analysis; as can be seen from Table 4, the total  $C_D$  has increased. This could be due to the already adequate radius of the front fender of the *Discovery*; existing Dept. For Transport research has shown that drag increases with additional front turning vanes in such cases.<sup>12</sup>

**Table 4 – front side turning vane**

Front side turning vane structure	$C_D = 0.429$ (2.14% increase from datum)
-----------------------------------	--



#### 4.2.2. Windscreen 'A' frame vane

As can be seen in the previous pressure plot (Figure 31 & Figure 32), the higher dynamic pressure zones on the vehicle are indications of high local velocities which lead to an adverse pressure gradient, and boundary layer separation, the energy being transformed into reversed direction turbulent vortices. This implies that it is imperative to assess the effect of turning vanes placed in these localised areas. It will be shown in the subsequent analyses that a rear turning vane encompassing the high dynamic pressure zone to the rear of the vehicle has a dramatic improvement on  $C_D$ . This 'A' frame analysis shows the upper windscreen column encompassed by a turning vane, in an effort forcibly to maintain the boundary layer in the area of fluid slow-down and high dynamic pressure.

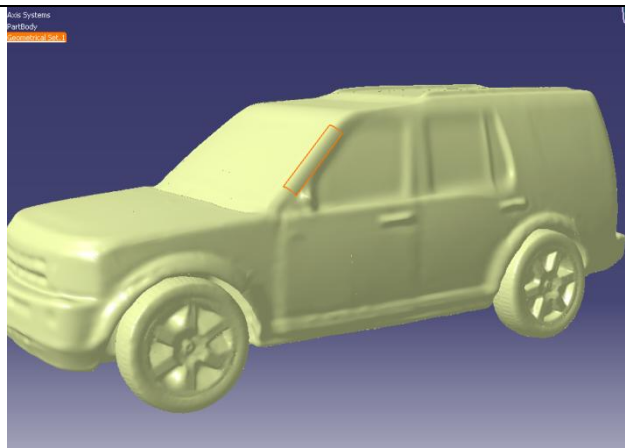


Figure 34 - 'A' frame vane

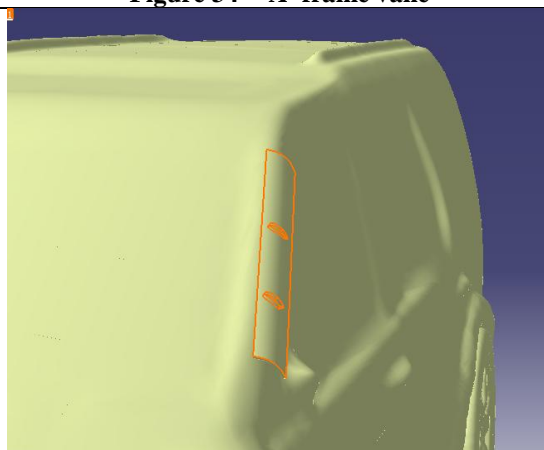
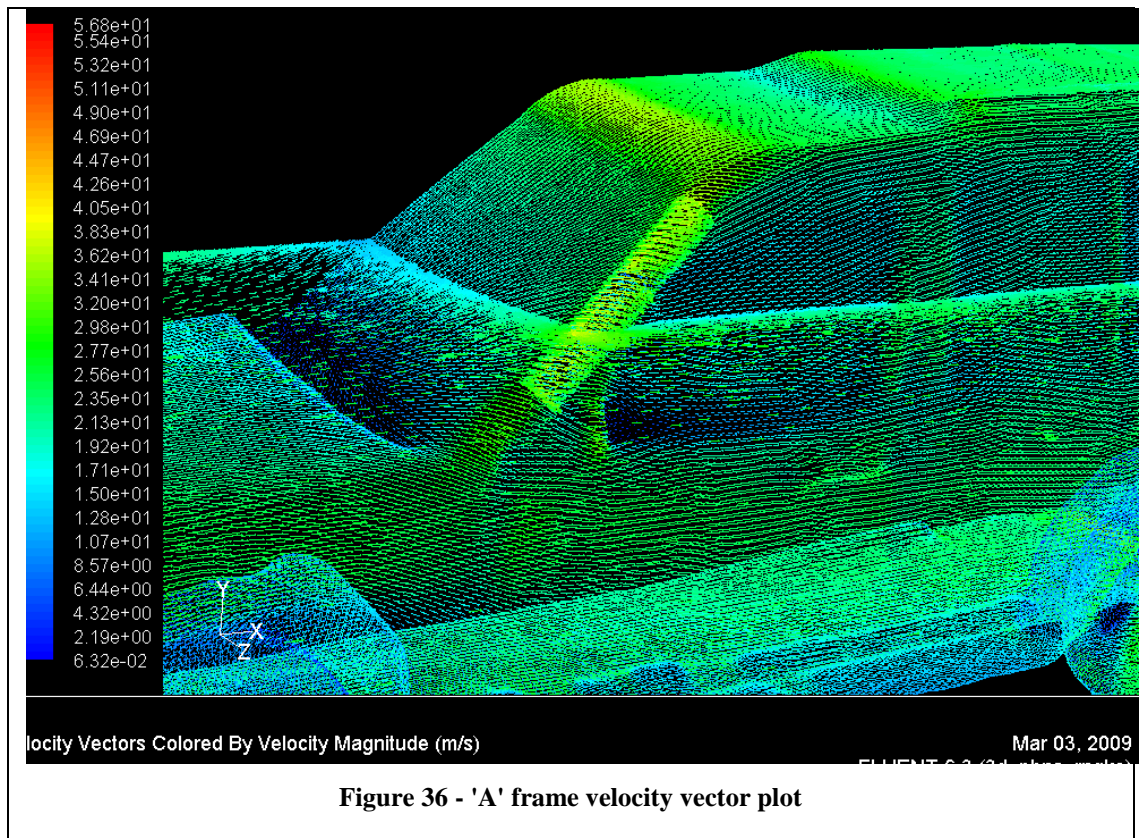


Figure 35 - 'A' frame vane detail

Figure 34 & Figure 35 show the CAD 'A' frame TV adaption, modelled using *Catia*.



The image in Figure 36 shows the front turning vane effect in the plane of the windscreen. To prevent premature layer detachment the air flow boundary layer around the windscreen pillar must be maintained. The vane is inline with the pillar and provides a small channel (between the vehicle and the vane) for air to manoeuvre around the bluff corner. The external side of the vane supplies a smooth curvature, which also maintains the steady attached flow.

**Table 5 – 'A' frame Vane data**

'A' frame Turning vane structure	$C_D = 0.408$ (4.77% decrease from datum)
----------------------------------	--

This turning vane analysis shows drag decrease (Table 5), which was expected when considering the original dynamic pressure plots on the datum model, and the extended area over which adverse pressure gradients were encouraging air-flow separation.



### 4.2.3. Windscreen roof vane

This design is an extension of data recorded in HGV yearly records. Although aerodynamic roof vanes are not currently in existence, cab sun-shades are, and interesting observations have been made. From a freight best practice survey of 718 vehicles 69% noted an aerodynamic advantage to having a cab sun-visor.<sup>12</sup>

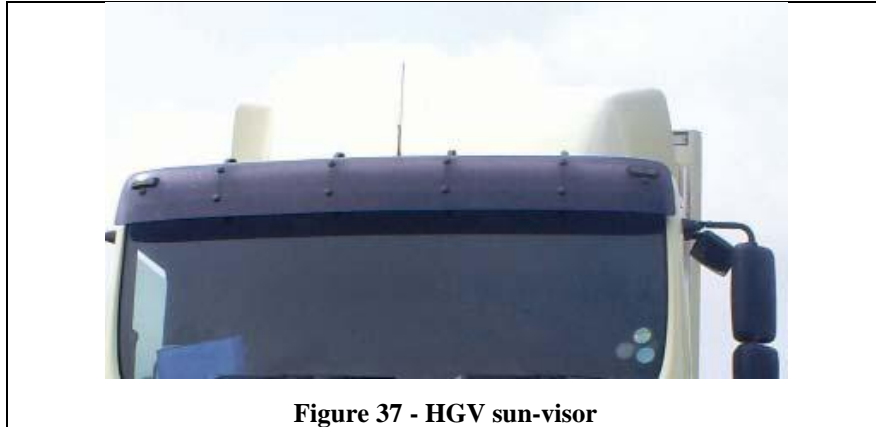


**Figure 37 - HGV sun-visor**

Sun-visors on HGV vehicles are obviously not designed to aid vehicle aerodynamics - and only certain designs (Figure 37) have been noted to have drag-reducing qualities. Effectively the sun-visor acts as a crude turning vane structure, maintaining the boundary layer and increasing the effective edge radius as described previously.

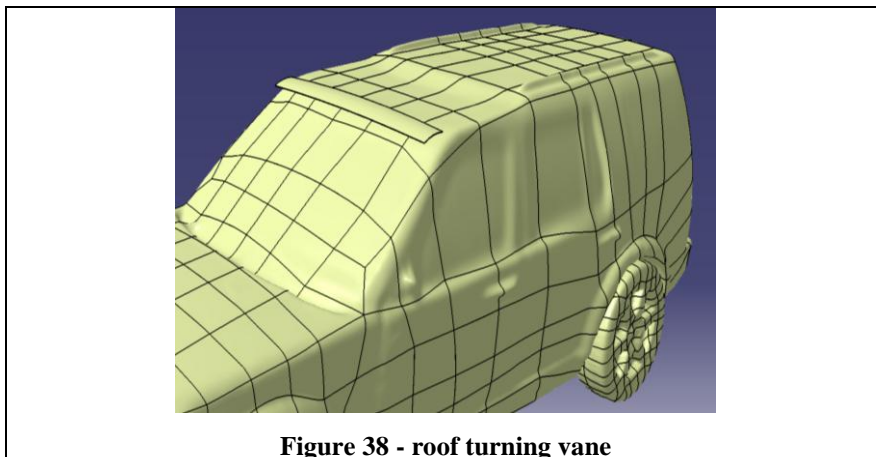


**Figure 38 - roof turning vane**

The roof turning vane in Figure 38 is similar to the sun-visor in Figure 37; the vane is located on a region of adverse pressure gradient, and thus flow separation.

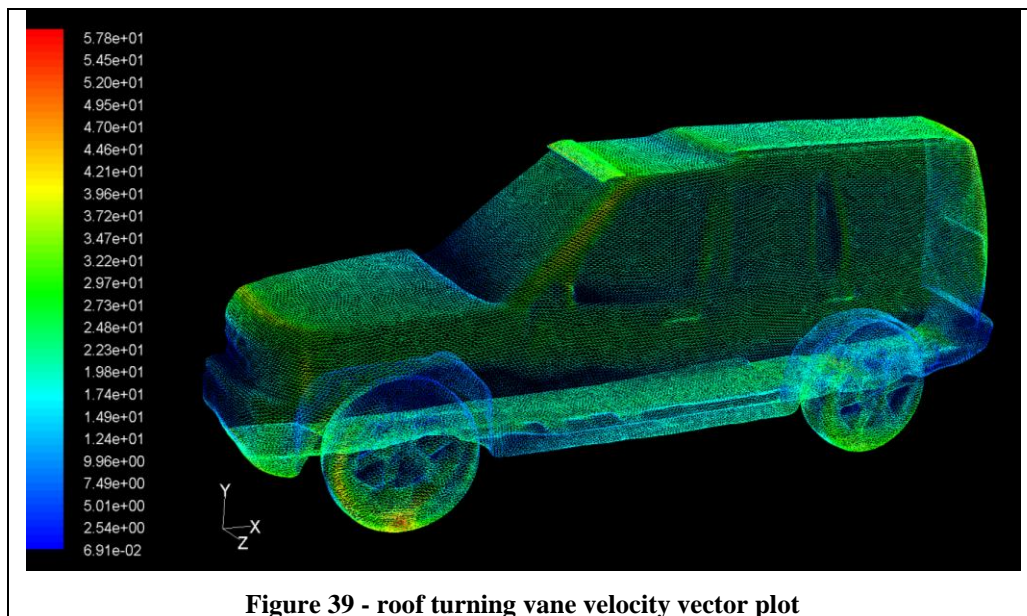


**Figure 39 - roof turning vane velocity vector plot**

The vane works in much the same way as was discussed earlier and a drag decrease has been noted (Table 6). Further development of this design could well yield further drag decreases for the SUV, plus sun-visor applications could be re-designed with an aerodynamic dual purpose.

**Table 6 – Roof vane data**

Windscreen / roof vane	$C_D = 0.399$ (5% decrease from datum)
------------------------	---

It can clearly be seen in Figure 31 & Figure 32 that energy loss is occurring in the regions undergoing an adverse pressure gradient; turning vanes have been applied to these adverse pressure areas in an attempt to reap an aerodynamic benefit. Hucho states that “The Aerodynamicist tracks down ‘weak points’ in the flow around a car – first of all separations – and he attempts to approach the ideal (i.e. attached flow) by modifying the geometry.”<sup>17</sup>

Gaylard points out that these ‘weak points’ are, typically, regions of energy loss – as a crude equivalence can be drawn between energy loss and vehicle drag.<sup>11</sup>

Newton’s 3<sup>rd</sup> law applies - as the vehicle applies force to the fluid, the fluid applies an opposite force to the vehicle (at constant velocity), i.e. drag. One way of non-

contact measurement of a vehicle's drag is to measure the momentum loss in the wake; this momentum loss is exactly equal to the drag on the vehicle.

#### 4.2.4. Side rear vane

The rear side vane in Figure 40 is angled to follow the contours of the external wall of the vehicle, with a gap of approx. 25mm, which allows the boundary layer passage without capturing the bulk flow. Again, the rear of the vehicle is modified due to the dynamic pressure and velocity fluctuation noted on the datum analysis.

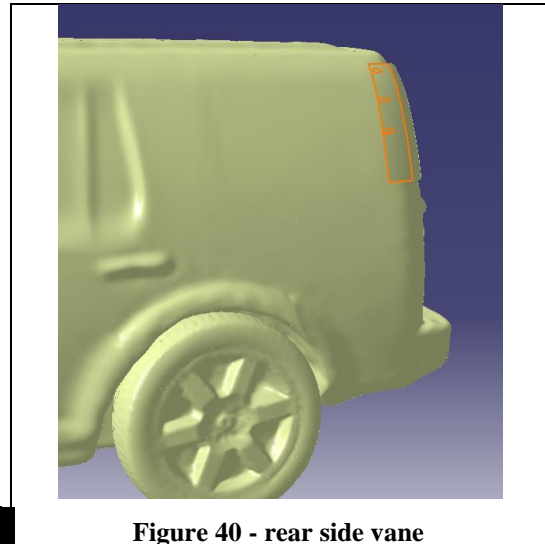


Figure 40 - rear side vane

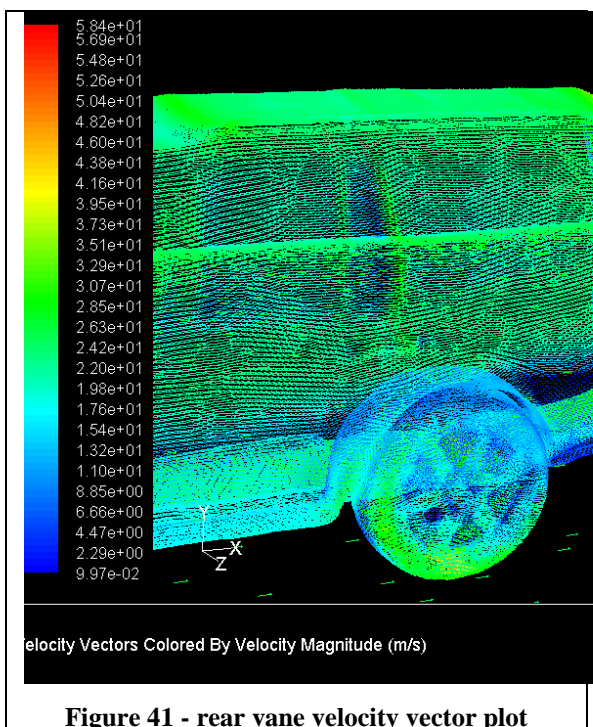


Figure 41 - rear vane velocity vector plot

Again further development of this design may prove beneficial to drag-relief. Figure 41 shows the velocity vector plot, drag reduction is noted (Table 7). The exposed sharp edges on this basic design lead to vortex creation and an added drag factor. As will be shown later, cowled edges in general minimise these drag factors.

**Table 7 – Side rear vane data**

Side rear vane	$C_D = 0.408$ (2.85% decrease from datum)
----------------	--

#### 4.2.5. Rear roof turning vane

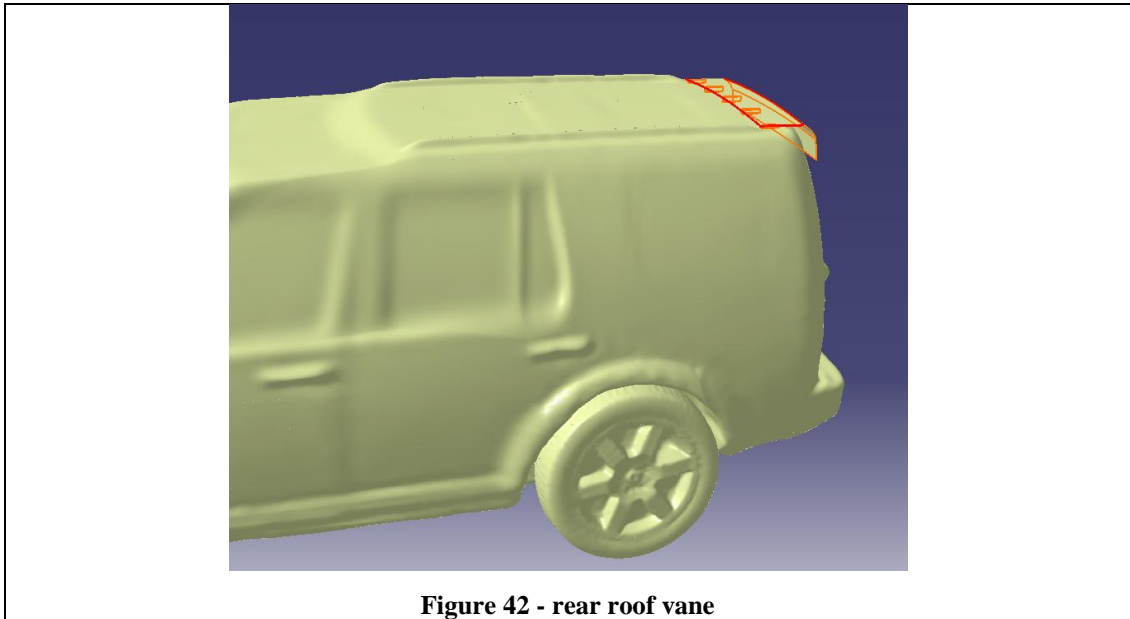


**Figure 42 - rear roof vane**

The rear roof vane (Figure 42) was designed in response to the  $C_D$  decrease created by applying turning vanes to body-work regions showing adverse pressure gradients. As can be seen in Figure 32, the rear roof section of the *Discovery* shows the greatest indication of an adverse pressure gradient. The rear vane pictured in Figure 43 has a vane/body distance of 25mm, which is approx. the boundary layer thickness.<sup>18</sup> The struts shown in Figure 43 seem to have an added  $C_D$  benefit; they appear to be acting like boundary layer fences, preventing the boundary layer from sweeping to the sides of the rear and thickening.

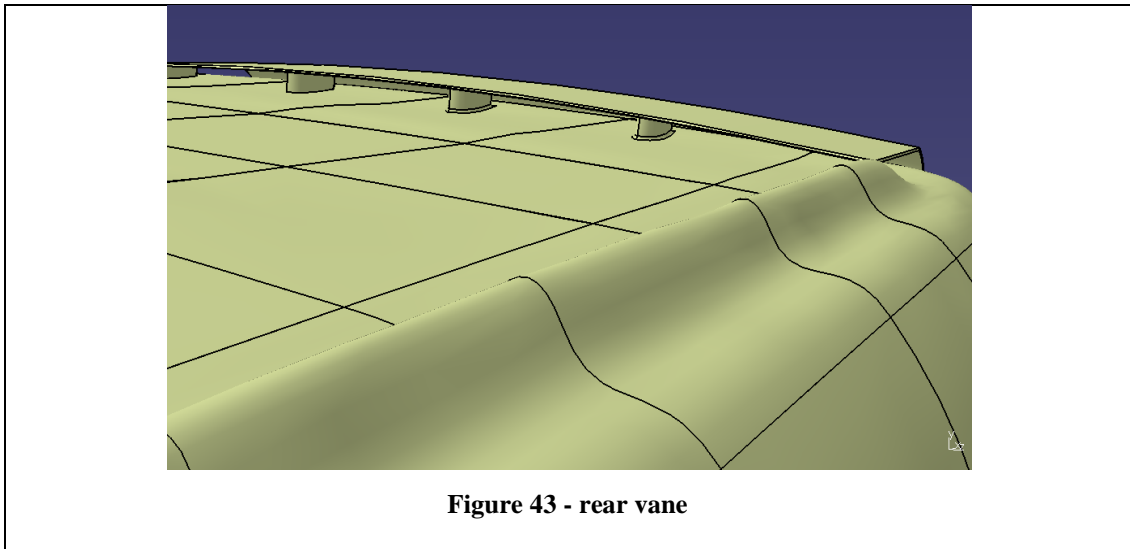


Figure 43 - rear vane

**Table 8 – Rear roof vane data**

Rear roof vane	$C_D = 0.377$ (10.24% decrease from datum)
----------------	---

Table 8 shows the largest  $C_D$  decrease in initial turning vane application to the *Discovery* analysis model due to its being the largest continuous area on the vehicle undergoing adverse pressure gradients leading to boundary layer separation. After this result greater focus was applied to this design, in order to maximise  $C_D$  reduction, with the minimum vehicle adaption.

#### 4.3. *Rear roof turning vane adaption results*

Since the most extreme drag reduction appears to come directly from the rear turning vane it is necessary to find by cumulative trial and error the most effective rear turning vane design. This can be assessed using a simple group of varying designs; the initial hypothesis is that the wider inlet leading to the narrower outlet should be the optimum drag reducer, as it effectively injects high velocity air into the low velocity zone at the immediate rear of the vehicle. Having said this it is possible that the higher velocity air, effectively ‘bled’ to the rear, may increase drag due to

recirculation and cause greater turbulence. Increased inlet size will also lead to ‘air scooping’ and high pressure drag.

Due to design constraints and the problems of model construction testing hypotheses regarding the drag reduction mechanism led to greater understanding of the mechanism, allowing the generation of a series of competitively better designs in terms of  $C_D$  reduction. Each design can be individually tested and the good points can be considered and accentuated in the subsequent designs until an optimum has been reached.

Figure 44 shows a diagram containing two simplified images of the rear of the *Discovery*. Image (a) shows the outlet part of the vane, data was taken from 0 degrees (dotted line) up to 60 degrees from the dotted line. Image (b) shows the inlet part of the vane, data was recorded from 0 degrees (dashed line) up to 30 degrees from dashed line.

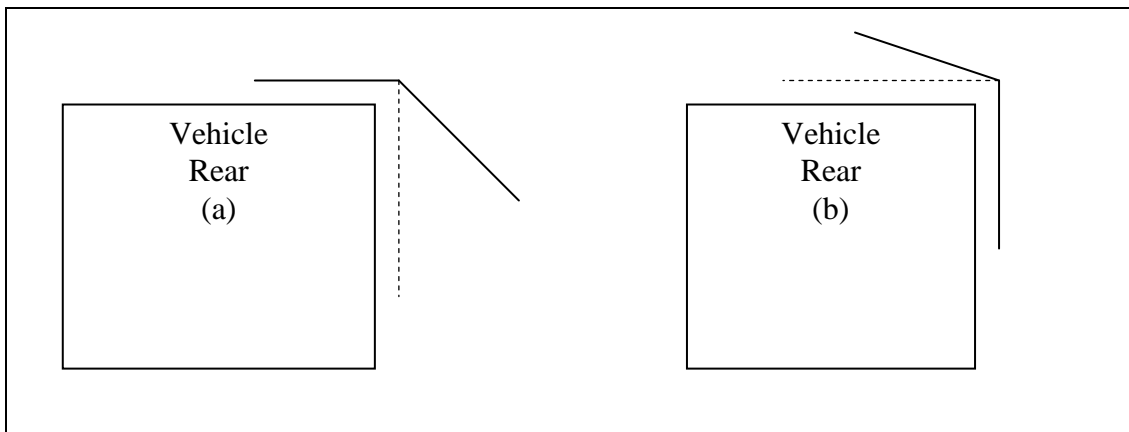


**Figure 44 - rear vane angle optimisation**

**Table 9 – rear vane angle optimisation data (increasing inlet size)**

$C_D$	inlet (angle from direction parallel to flow)	outlet (normal to flow)
0.391	0	0
0.395	10	0
0.443	20	0
0.472	30	0

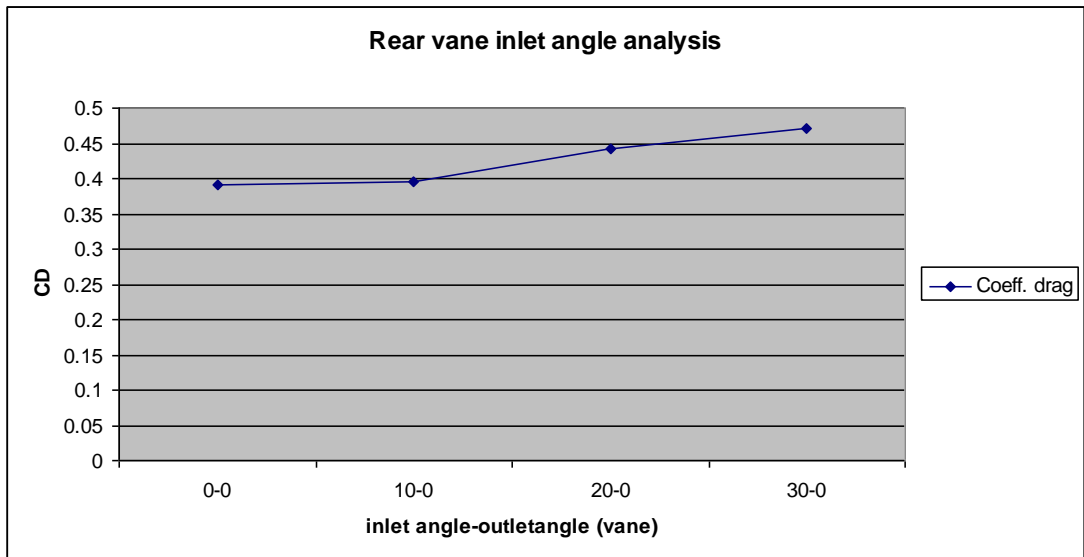


**Figure 45 - Graph to show relationship between turning vane inlet angle and  $C_D$**

Figure 45 and Table 9 shows that the increase in inlet angle leads to a steady drag increase, due to the effect of air scooping not only the faster moving boundary layer but also the bulk flow. It has to be stated that the Turning vane used in this data was a simplified 'straight' vane that was not smoothly curved nor mirroring the curve of the rear roof (at right angles to flow); for simplicity the attaching struts were also removed.

**Table 10 – Rear vane angle optimisation data (increasing outlet size)**

$C_D$	inlet (angle from direction parallel to flow)	outlet (normal to flow)
0.391	0	0
0.396	0	10
0.403	0	20
0.386	0	30
0.416	0	40
0.411	0	50
0.402	0	60

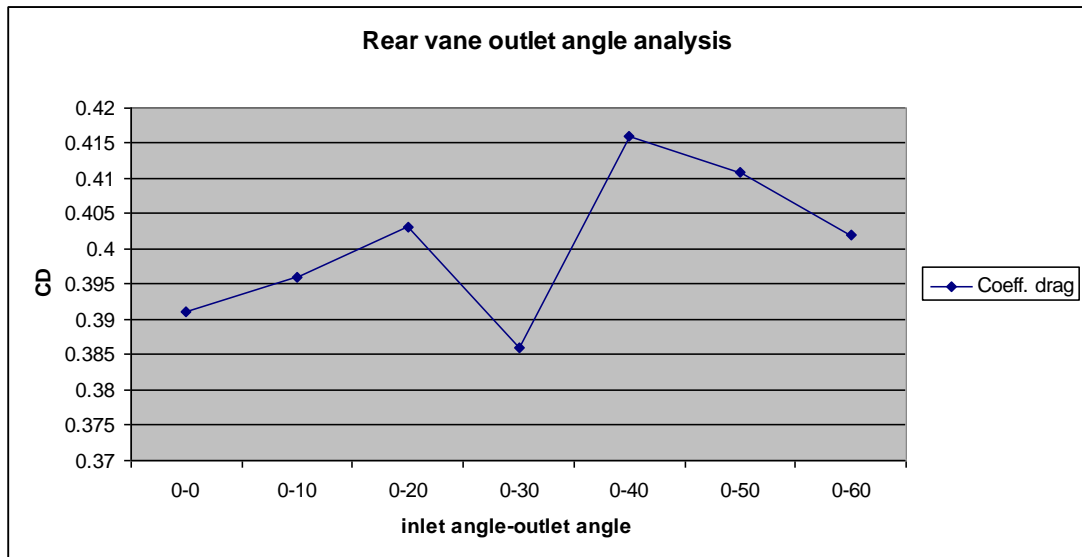
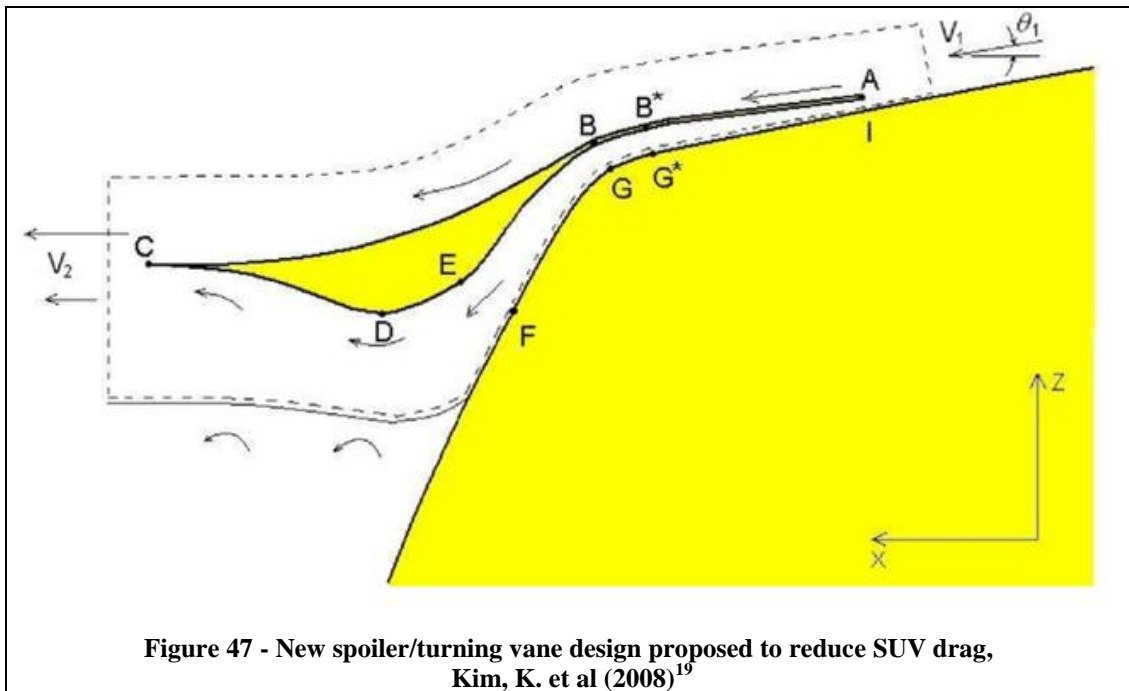


**Figure 46 - Graph to show relationship between vane outlet angle and  $C_D$**

Figure 46 and Table 10 shows a sharp decrease in  $C_D$  at the 30 deg outlet zone, and also at the 60 deg zone. This trend was also found during wind-tunnel test work.

Recently, (2008), research has been published by a fluid dynamics research team from the University of Michigan-Dearborn relating to the effects of turning vane-like structures fitted to the rear of bluff backed vehicles. The rear turning vane structure reportedly shows a drag decrease of 5% on SUV-like vehicles travelling at 108 kph (67mph).<sup>19</sup>





As was mentioned earlier the rear pressure drag on bluff-backed vehicles, and the resulting boundary layer separation due to the adverse pressure gradients, greatly increases SUV drag. Kim, K. et al<sup>19</sup> were interested in increasing the dynamic pressure drop associated with the rear of the vehicle. They effectively designed a diffuser style turning vane. Setting the diffuser outlet at 30 deg, and at 60 deg, to the rear has been noted to produce the best drag coefficient in both CFD analysis and wind tunnel-tests (see Table 10 & **Error! Reference source not found.**) in this investigation. The small inlet/ diffuser outlet design (Figure 50) also shows good  $C_D$  decrease from the datum model. A ‘diffuser’ allows the velocity to transition gradually using the *Bernoulli principle*; the adverse pressure gradients seen on the datum (Figure 31 & Figure 32) can be avoided by using diffuser designs such as that in Figure 47. The upper section (of the design in Figure 47) also allows a smoother velocity transition for the bulk flow, reminiscent of the 0-60 degree vane diffuser (Table 10). Kim, K. et al seem to have incorporated the best-performing turning vane angles with regard to boundary layer maintenance and smooth handling of the bulk flow.

According to Kim, K. et al:

The scientific principle and geometry of the new rear-spoiler are completely different from those of conventional spoilers that have been used so far. The new rear spoiler acts like a diffuser when it is attached to the back of a vehicle, and thus, the pressure on the back of a vehicle with the new spoiler is higher than that on the back of a vehicle without it.

The new rear spoiler can be applied to other minivans, vans, sports-utility-vehicles and buses. With the new spoiler attached, the vehicles having a bluff back would have not only a higher mileage but also better stability.<sup>19</sup>

This diffuser mechanism expands the flow, causing a reduction in velocity and hence an increase in dynamic pressure to the rear of the vehicle, pressurising the rear wake.

#### *4.3.1. Large inlet/nozzle outlet*

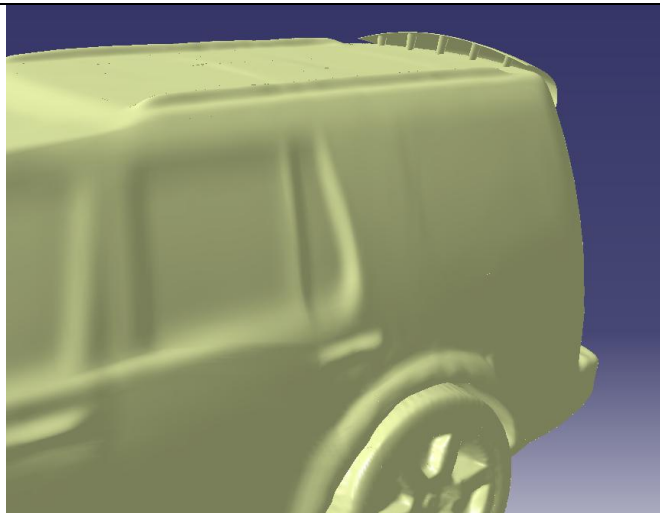


**Figure 48 - large inlet/nozzle outlet**

The design above shows a large inlet in full scale. It is 75mm in height and it has an outlet of 25mm distance from rear window.

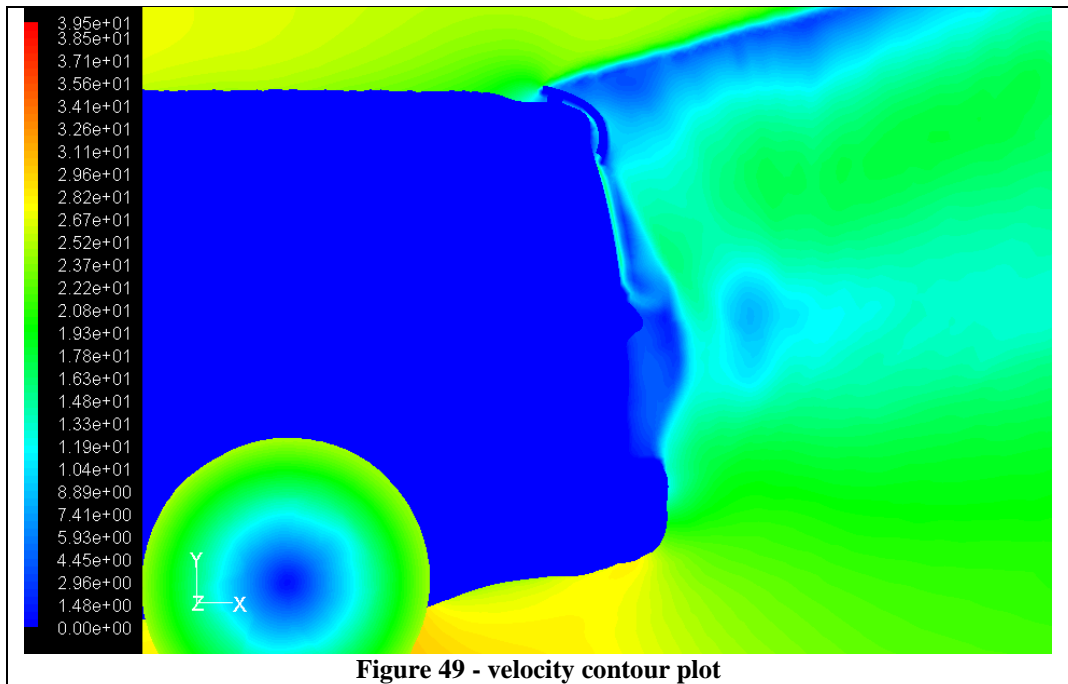


Figure 49 - velocity contour plot

This velocity plot shows the large inlet acting as an air-scoop which, as a result, causes a large region of low velocity air from its leading edge. The rear contracting outlet injects a sheet of much higher velocity air (~17.5m/s) to the back region of the vehicle, inducing a visible increase in the rear velocity.

Table 11 –  $C_D$  data for large inlet/nozzle outlet

Large inlet/nozzle outlet (Figure 49)	$C_D = 0.447$ (6.42% increase from datum)
---------------------------------------	--

Table 11 shows the  $C_D$  data for the vane tested in Figure 49. A  $C_D$  increase is noted, but the effect of higher velocity air injection to the rear provides an interesting ‘bleed-like’ situation.

Potentially the major problem with this design is the size of the inlet; full scale it reached a height of approx. 75mm. This crossed the boundary layer thickness level (approx. 25mm) and instead of skimming off the high velocity attached boundary layer, lower velocity bulk flow air was disturbed. The nozzle outlet energised the rear of the vehicle greatly, effectively acting as a bleed system, but the inlet size forced a premature layer separation. Figure 49 indicates that a greater volumetric flow of air to the rear can prevent separation in other areas, but that the inlet size required creates its own separation problem.

### 4.3.2. Narrow inlet/diffuser outlet

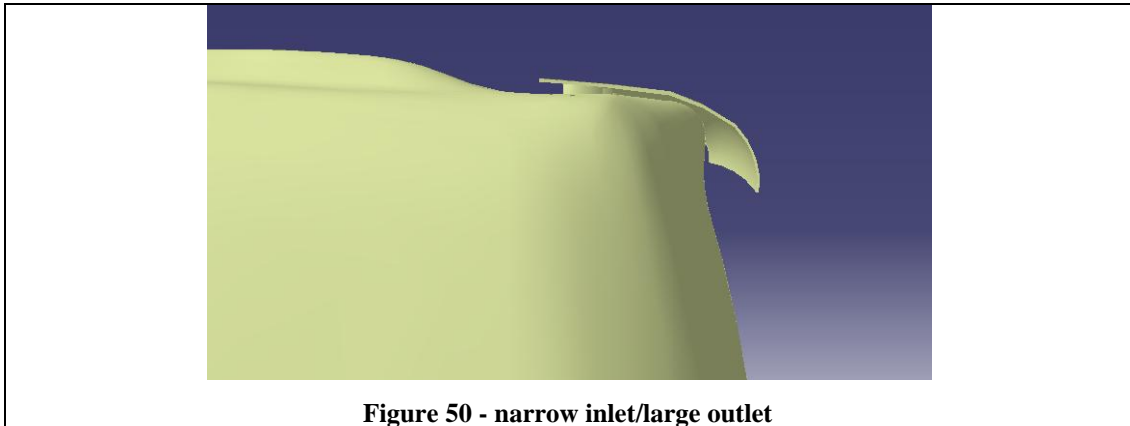


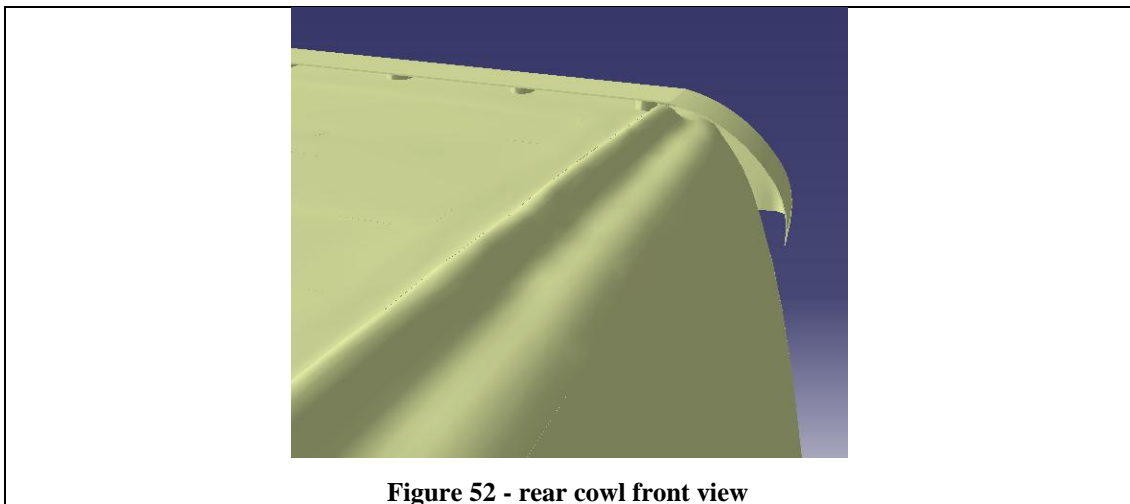
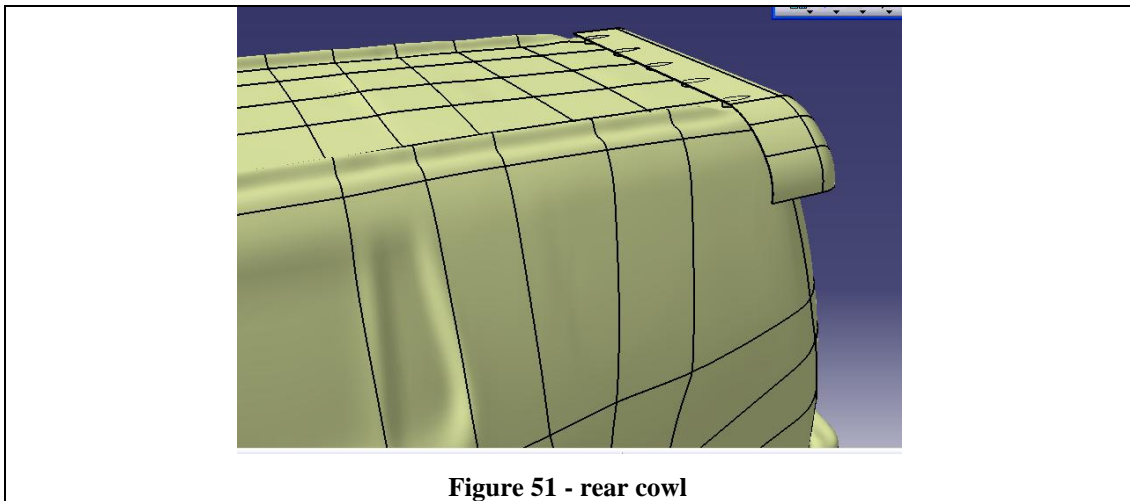
**Table 12 –  $C_D$  data for narrow inlet/diffuser outlet**

Narrow inlet/Diffuser outlet (Figure 50)	$C_D = 0.397$ (5.48% decrease from datum)
--	--

Figure 50 shows the narrow inlet/diffuser outlet. This design has the same basic shape of the original rear vane, but with a larger diffuser style outlet. In Table 12 a  $C_D$  decrease is noted, but this decrease is not as marked as the decrease observed in the original rear vane case.

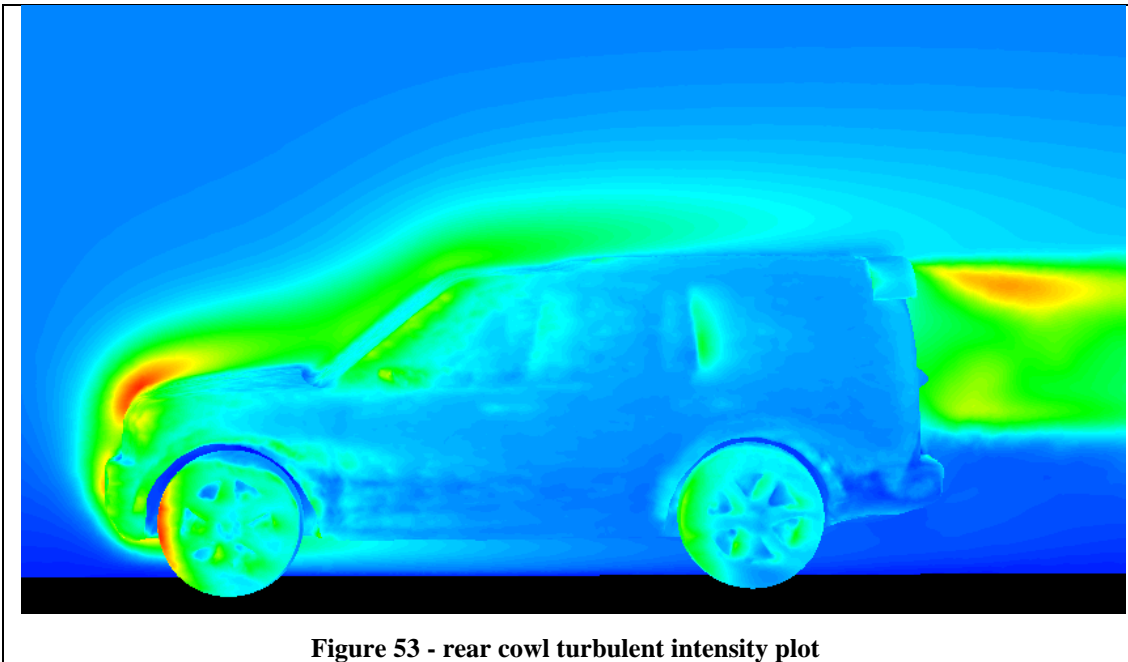
### 4.3.3. Rear roof cowl

The rear turning vane adaption pictured in Figure 51 represents a modification of the original rear turning vane (Figure 43). The ‘corner cowling’ section is designed to deal with the boundary separation across the upper rear column section of the *Discovery*. In an effort to maintain the boundary layer in this perpendicular section the cowl arcs around the upper corner. This design also reduces the number of sharp corners which lead to premature separation. The design is intended to re-direct as much air as possible without greatly increasing the inlet angle.



**Table 13 –  $C_D$  data for rear cowl**

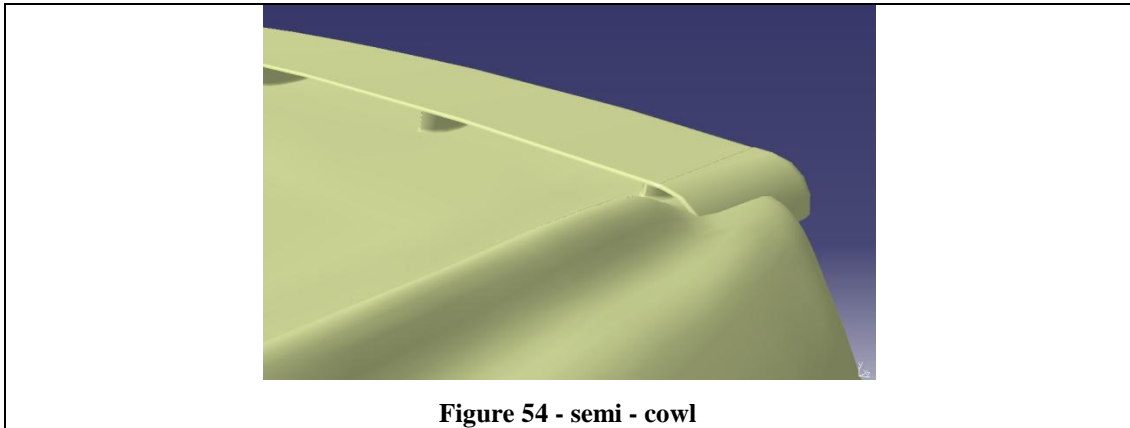
Rear cowl (Figure 52)	$C_D = 0.399$ (5% decrease from datum)
-----------------------	---



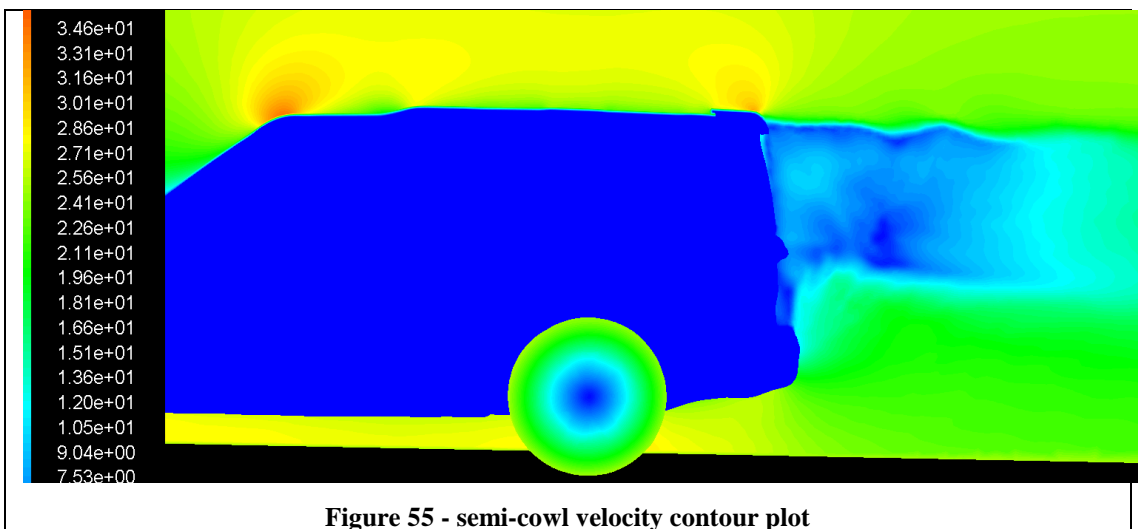
The overall  $C_D$  has decreased from the datum by 5% (Table 13). This is a  $C_D$  decrease - but not as marked a decrease as in the initial rear turning vane case. This could be due to the air scoop-effect at the sides of the structure, and to the vane itself being too large, not allowing the flow to recover adequately.

Figure 53 shows the turbulence intensity plot across the vehicle with the rear cowl added. The front section shows the greatest turbulent intensity while the rear shows an area of high intensity possibly due to separation from the outer part of the vane.

#### 4.3.4. Rear roof semi-cowl



The design shown in Figure 54 illustrates a design overlap between the ‘rear cowl’ vane and the ‘rear vane’. The open edges of the ‘rear vane’ have been filled in with an aerodynamic cowl shape, but the overall design is tucked in to the bodywork much more, and tapers towards the rear. The design is still at 90 degrees, but the edges have been smoothed and the rear hang length of the vane has been greatly decreased, allowing for door accessibility. The rear hang length of the outlet was also thought to isolate the flow for too long, preventing adequate flow recovery (Figure 53)



**Table 14 – C<sub>D</sub> data for rear semi-cowl**

Rear semi-cowl (Figure 55)	$C_D = 0.372$ (11.43% decrease from datum)
----------------------------	---

The enclosed edges and the ‘merged’ structure have decreased vortex generation at the outer edges of the rear vane, and have decreased overall drag greatly. Figure 55 shows that the boundary layer is maintained for longer across the external area of the vane. The internal area effectively re-directs the flow to the rear. Separating the rear roof from the rear sides has a drag relieving effect. The smooth transition in design may have reduced the separation that was produced by the abruptness of the previous design.

## **5. Rear vortex generation and associated drag reduction**

### *5.1. Vortex generation discussion*

A major method of boundary layer control which relies on high turbulence intensity is vortex generation. Vortex generation is employed to re-energise a boundary layer which otherwise would separate. A turbulent layer can survive an adverse pressure gradient for some distance before separating. For any boundary layer, however, the greater the adverse pressure gradient, the sooner separation occurs.<sup>2</sup>

According to Thwaites a natural form of this phenomenon is ‘turbulent mixing’, which enables a turbulent boundary layer to overcome an adverse pressure gradient sufficient to cause a laminar layer to separate.<sup>13</sup>

In this section artificial methods of increasing the transfer, via turbulent mixing of energy from the free stream into the boundary layer have been added and styled on the bodywork of the *Discovery*. Vortex generation was first proposed at the United Aircraft Corporation, and is largely connected with the work of H.D. Taylor (1947) and Bruynes (1951). Many experiments have been performed, largely by McCullough, Nitzberg, and Kelly (1951), on Clark-Y aerofoils using small vane-like structures set at an angle of incidence to the local flow direction. Research indicates that aerofoil VGs arranged along a span-wise line on the top rear side alternately at  $\pm 22.5^\circ$  incidence creates contra-rotating vortex systems.<sup>13</sup>



## 5.2. Vortex generation results

### 5.2.1. Delta 'bump' Vortex generators

A turbulent boundary layer also delays flow separation in certain circumstances. Or even causes the re-attachment of separated flow. This design (Figure 56) tests vortex generation, and the drag-relieving effects it is seen to produce. Figure 56 is a relatively basic vortex-generating structure placed at the rear of the *Discovery*. It was found that the optimum height of the VGs is almost equivalent to the thickness of the boundary layer<sup>18</sup> (15 to 25 mm) and that the optimum method of placement is to arrange them in a row in the lateral direction 100 mm upstream of the roof end at intervals of 100mm. The VGs are not highly sensitive to these parameters and their optimum value ranges are wide. Better effects are obtained from delta wing-shaped VGs than from bump-shaped VGs. The vortex generators were placed and designed at (100mm) intervals as per the best practice investigation<sup>18</sup>

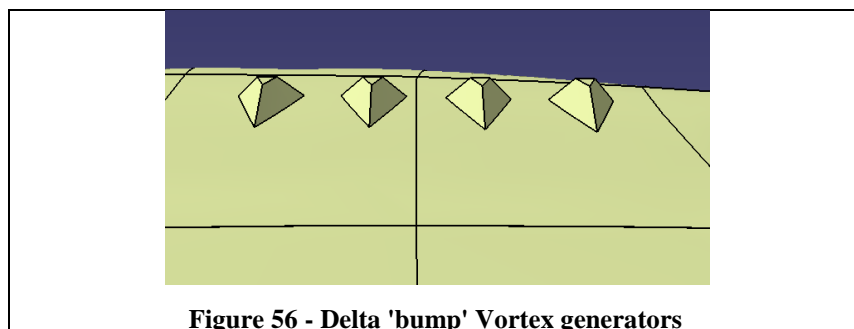
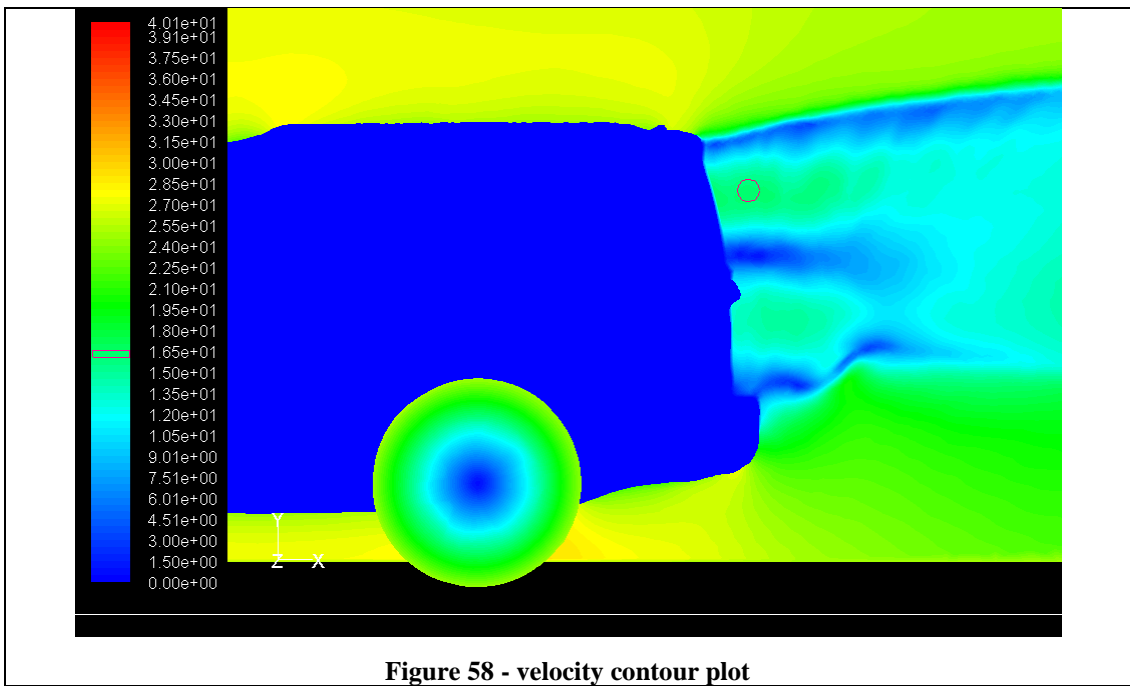
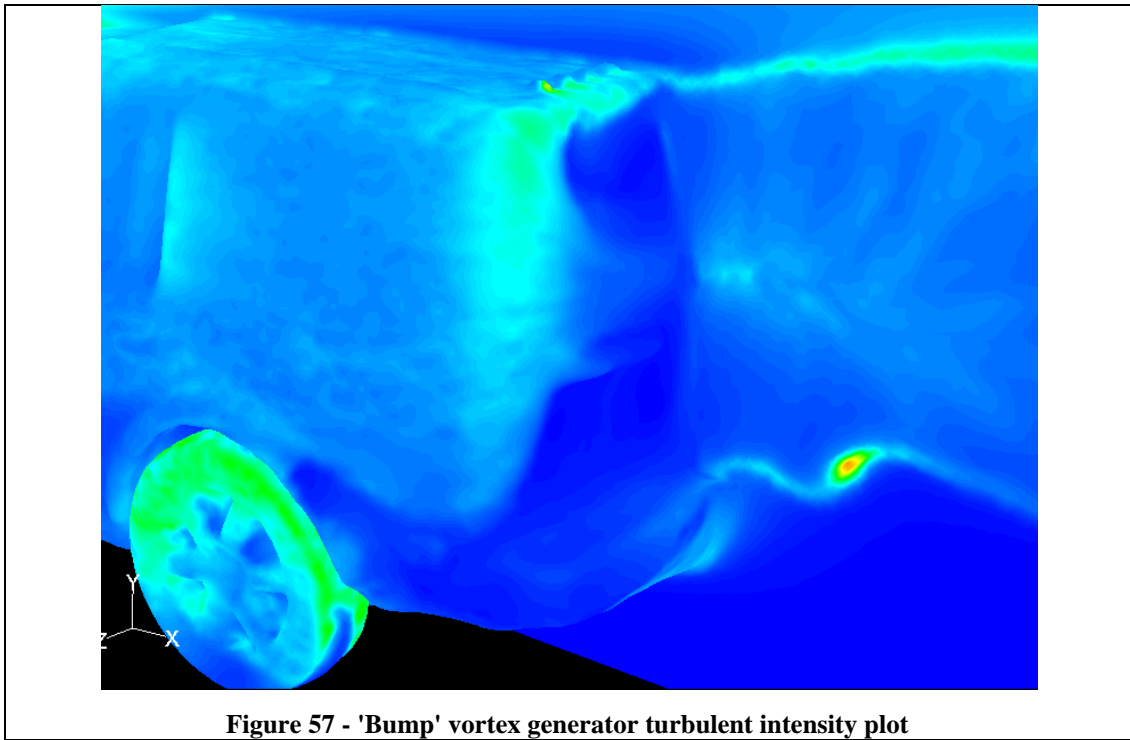


**Figure 56 - Delta 'bump' Vortex generators**

The VG design shown in Figure 56 is a simplified adaption to the current vortex generator designs seen on many vehicles today. Research by KOIKE, M et al indicates that these 'bump' style vortex generators are less effective than the 'fin' style, due to their individually high projected areas and drag readings.

The CFD model was hand meshed (in this area) and refined element by element in order to prevent skew and provide an accurate mesh resolution for these small features, consequently tetrahedral growth rate was controlled in this area providing a 3D boundary of sufficient refinement, as per best practise<sup>14</sup>.



In this velocity magnitude plot (Figure 58) the air speed has been increased in two distinct pockets behind the vehicle. This is probably due to increased turbulence and vortex-creation induced by the vortex generators. High areas of turbulence can be seen resulting from the VGs (Figure 57). Air velocity has effectively been doubled

to a maximum of 16.5m/s, (Figure 58 indicated by circle) from the datum case (**Error! Reference source not found.**), indicating energy dissipation taking the form of turbulence.

**Table 15 – ‘Bump’ vortex generator data**

Delta ‘bump’ vortex generators	$C_D = 0.411$ 2.15% decrease from datum
--------------------------------	--

The  $C_D$  indicates a 2.15%  $C_D$  decrease (Table 15) from the accurate datum model (Figure 30), indicating a potential area that could result in better aerodynamics with little redesign or cost.

### 5.2.2. Delta ‘fin’ Vortex generators

According to research by KOIKE, M et al the delta-wing-shaped VGs should be installed at a yaw angle of  $15^\circ$  to the airflow direction. In order to meet this condition, the direction of airflow at the roof end was investigated by oil flow measurement.<sup>18</sup> It was found through investigation of Vortex generation that the airflow is aligned directly with the backward direction at the centre of a car, but that it increasingly deviates toward the centre as the measurement point shifts away from the central position. For this reason, the delta wing-shaped VGs must be installed at an angle of  $15^\circ$  to the vehicle centreline for the central position, whereas they must be installed at almost  $0^\circ$  for outermost positions.<sup>18</sup>

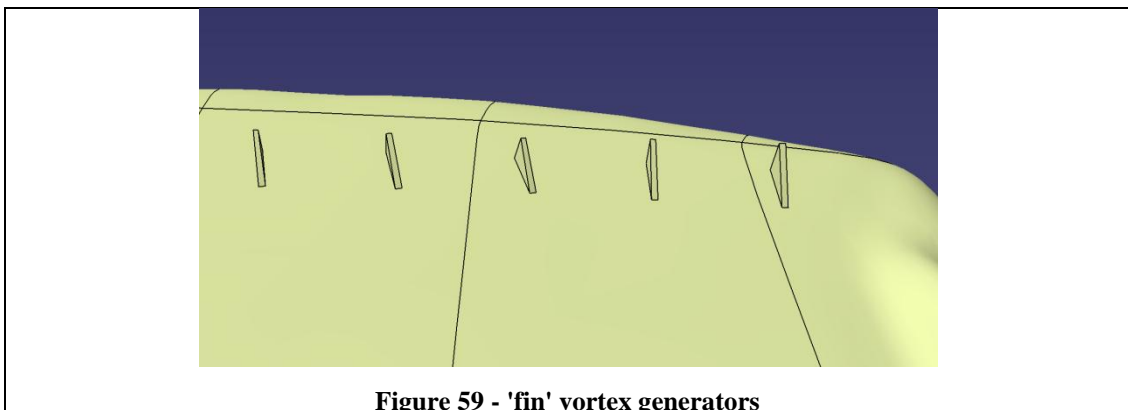


**Figure 59 - ‘fin’ vortex generators**

Figure 59 shows the recommended vortex generator shape and placement on the rear of the *Discovery*. An effort was made to place these VGs slightly upstream of the predicted separation point associated with the adverse pressure gradient.

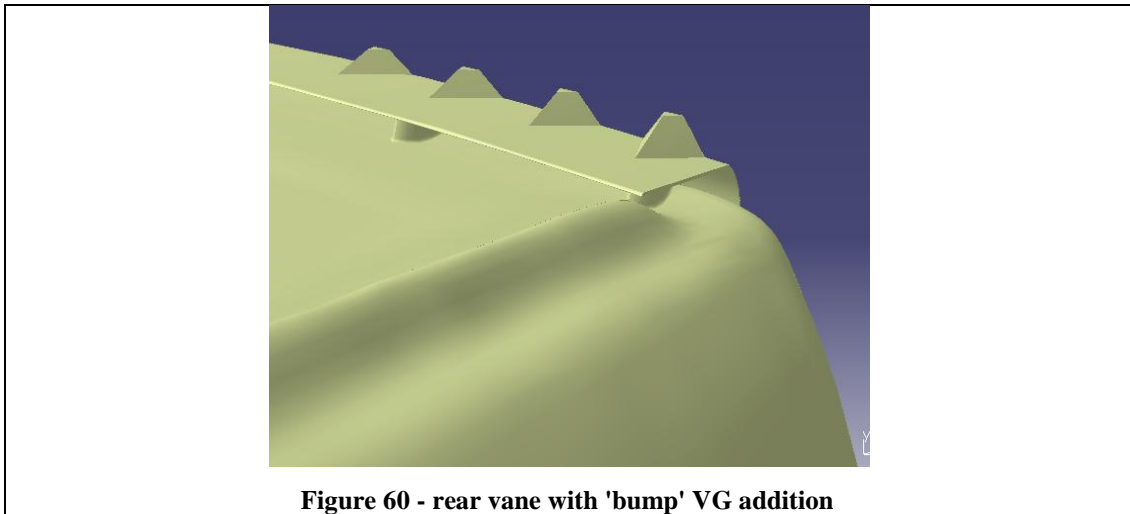
**Table 16 – Delta ‘fin’ VG data**

Delta ‘fin’ VGs, 25mm	$C_D = 0.398$ 5.24% reduction from datum
-----------------------	---

Table 16 shows a  $C_D$  decrease from datum and also from the ‘bump’ style VG. Both ‘bump’ and ‘fin’ vortex generators have drag reducing effects, encouraging faster re-attachment and a high level of boundary layer energy. According to KOIKE, M et al, VGs create stream-wise vortices, the vortices mix higher and lower layers of boundary layer and the mixture causes the flow separation point to shift downstream - consequently the separation region is narrowed. From this we can predict that VGs cause the pressure of the vehicle’s entire rear surface to increase, therefore decreasing drag.<sup>18</sup>

Reduced frontal area of these (fin) vortex structures diminishes the structures’ inherent drag, without decreasing the structures’ effects. The action of vortex generation creates drag; but if vortex generators are designed effectively this drag can be negated effectively.

### 5.2.3. Rear vane with 'bump' VG addition



The novel design shown in Figure 60 merges the 'bump' VG design and the 'rear vane' design, in an attempt to energise the boundary layer on the top surface of the rear vane, and in an attempt to increase re-attachment in order to obtain further drag reductions.

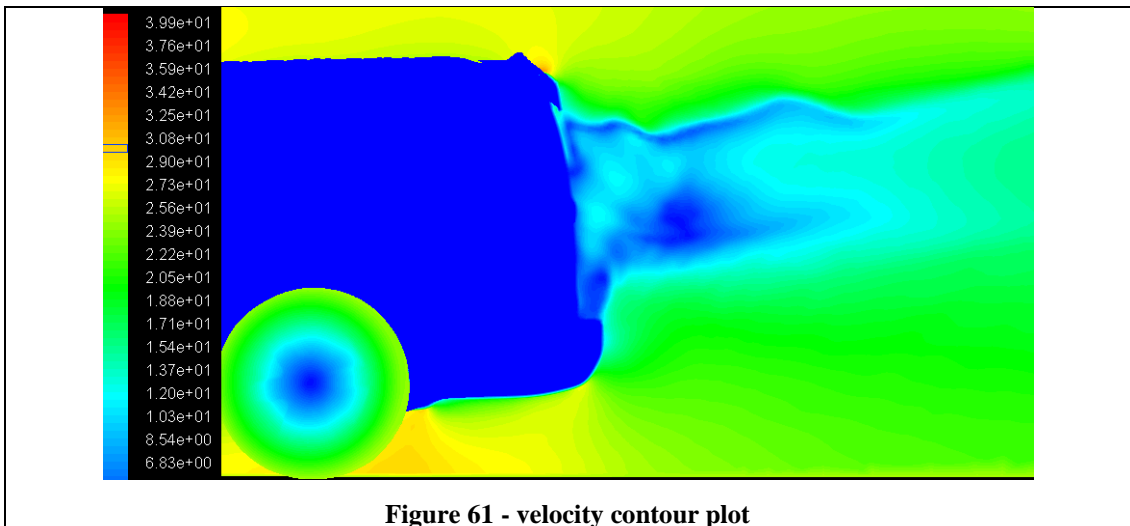


**Table 17 – Rear vane 'bump' VG addition data**

Rear vane 'bump' VG	$C_D = 0.395$ 5.96% reduction from datum
---------------------	---

It can be seen that the ‘bump-VG addition’ did not have the desired level of drag decrease, although when compared to the datum model a drag decrease was noted (Table 17). The increased surface area due to the vortex generator inclusion increases the pressure drag on the structure; the recommended height is 25mm (approx. boundary layer thickness).<sup>18</sup> The vortex generators have had the effect of moving the separation point on the top vane surface rearwards (Figure 61).

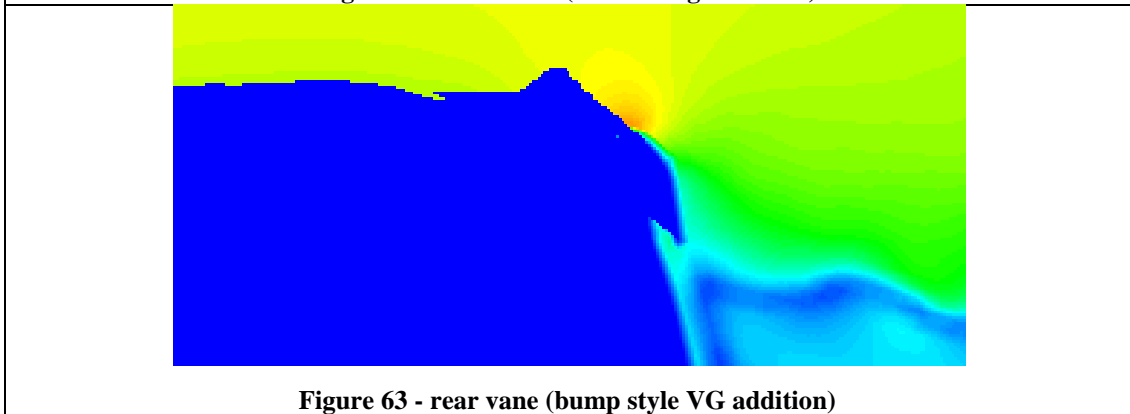
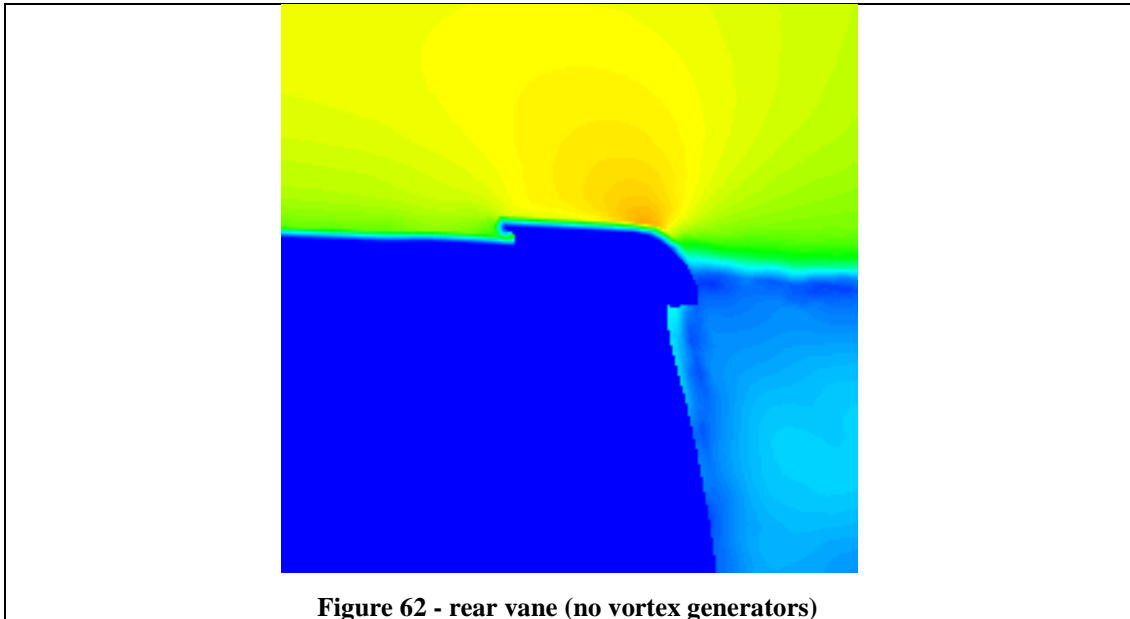
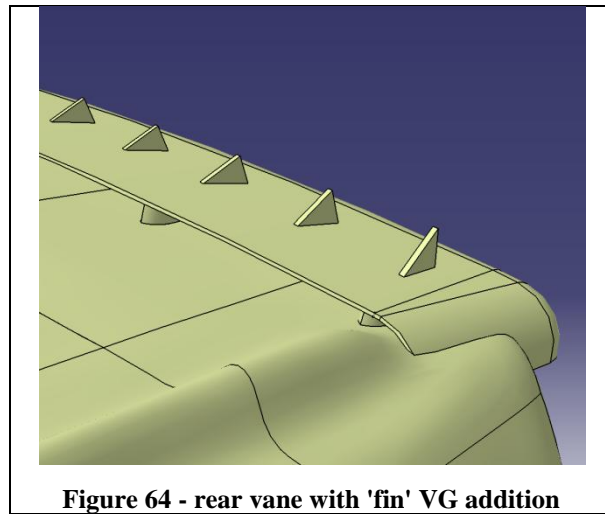


Figure 62 & Figure 63 show the velocity effects and boundary layer effects of the vortex generator addition to the rear vane. Figure 63 clearly shows that the separation point has been shifted downstream of the vortex generator.

#### 5.2.4. Rear vane with 'fin' VG addition



The design illustrated in Figure 64 shows the more successful VG 'fin' design coupled with the more successful 'Semi-cowl rear vane' design in an attempt to further decrease vehicle  $C_D$  by encouraging air-flow re-attachment due to external vortex creation. The 'fin' design is generally better due to the decrease in surface area of the VGs which lessens the profile drag of these structures. The angle of the fins decreases from a maximum of  $15^\circ$  to the normal - in the centre of the vehicle - to a minimum of  $0^\circ$  at the outside, acting in part as a 'boundary layer fence'. Research shows that the boundary layer tends to move sideways towards the wing tips [in aircraft] thus thickening the layer there and inducing early separation.<sup>1</sup> The design in Figure 64 prevents sideways movement to a certain extent, adding to drag reduction.

**Table 18 – Rear vane with 'fin' VG addition data**

Rear vane with 'fin' VG addition	$C_D = 0.365$ 13.1% decrease from datum
----------------------------------	--

Table 18 shows a 1.89% decrease from the original 'semi-cowl vane' design; the addition of the VGs has had the effect of decreasing the overall pressure drag by increasing the fluid velocity. It is the lowest  $C_D$  recorded, a 13.1% drag decrease from Datum model with the addition of the 'fin' VGs.

### 5.2.5. Front fender vortex generator design

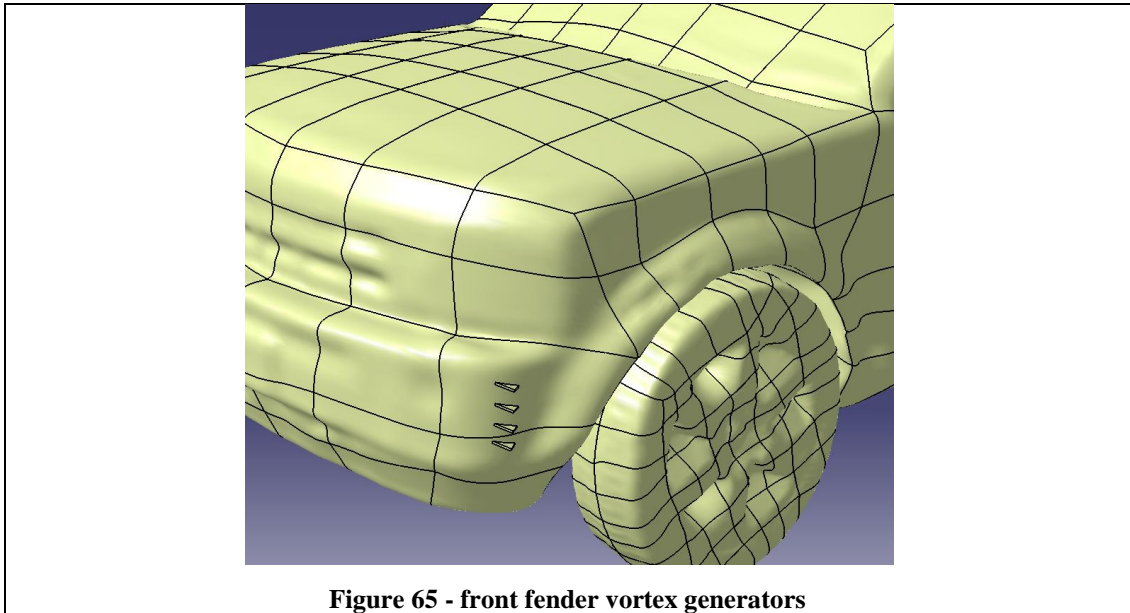


**Figure 65 - front fender vortex generators**

**Table 19 – front fender Vortex generation data**

Front fender Vortex generator design	$C_D = 0.391$ 6.91% decrease from datum
--------------------------------------	--

The front fender VGs (Figure 65) do the job of energising the boundary layer before the air flow encounters the rotating front wheel; a drag decrease was achieved (Table 19). The boundary layer is faster-flowing due to these VGs and more likely to re-attach after passing the wheel arch. The VGs are arranged at a 15 degree angle to the flow direction. They have been placed immediately in front of the wheel arch, and are similar in dimension to the rear VGs.



### 5.3. Design effects on boundary layer separation

Contour plots are frequently used in CFD and also in other analysis types such as FEA. The contour plots shown for the velocity and dynamic pressure present the reader with a physical image of the conditions undergone by the vehicle. Contours that are tightly clustered about vehicle features on the plots clearly indicate the presence of vigorous flow activity as the fluid passes over the rear of the vehicle and over other notable morphological features. According to Jiyuan TU, et al:

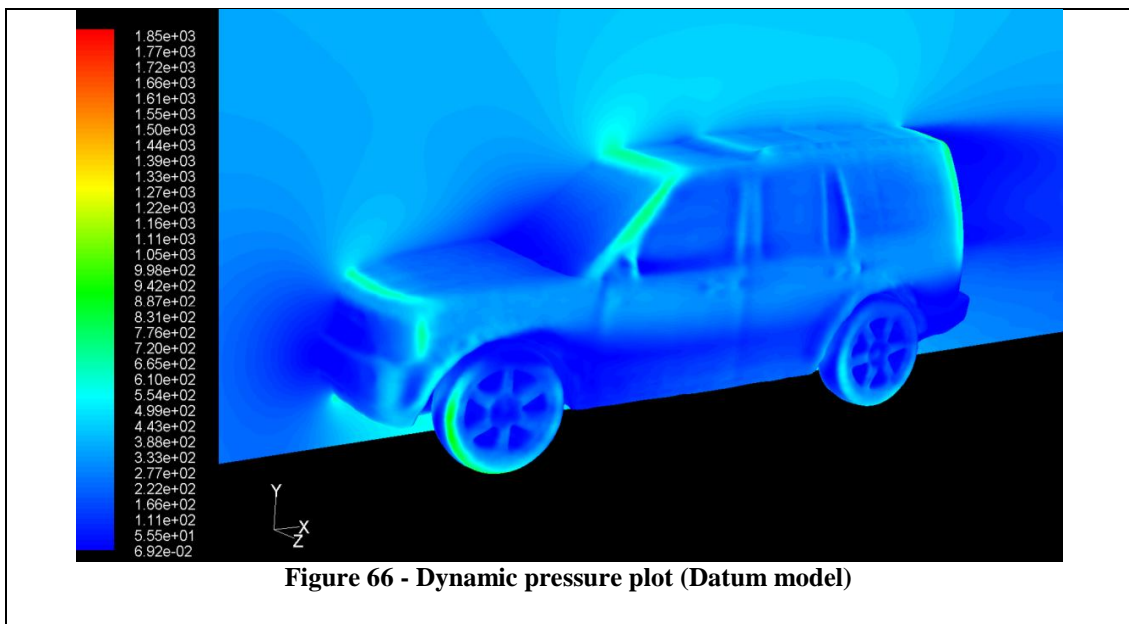
If the pressure *decreases* in the downstream direction, then the boundary layer thickness reduces; this case is termed as a *favourable pressure gradient*. If, however, the pressure *increases* in the downstream direction, then the boundary layer thickens rapidly; this case is termed as an *adverse pressure gradient*. This adverse pressure gradient together with the action of the shear forces acted at a sufficient length cause the boundary layer to come to rest. The flow separates from the surface leading to the formation of reversed flow eddies represented by apparent recirculation vortices (wakes).<sup>20</sup>

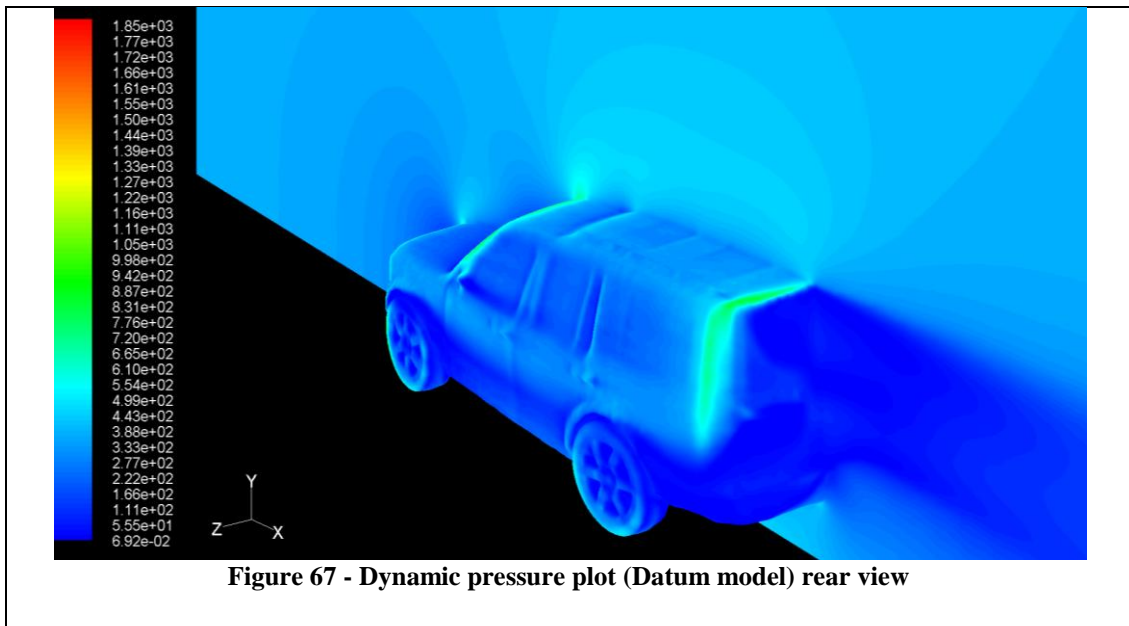
This section reviews the datum model and four drag reducing designs, in terms of dynamic pressure plots and also downforce production in an attempt to identify the cause of the drag-reduction observed.

## Datum Model

The datum model dynamic force plots are repeated in this section in Figure 66 & Figure 67. They show the increase in dynamic pressure associated with the regions of separation of the boundary layer. Separation effects of the subsequent designs can be compared with the images from the datum model. The separation area of interest is the rear roof section shown in Figure 67. The separation zone and area of adverse pressure gradient can be seen to follow the roof contour and to continue down the rear side, where the dynamic pressure gradually returns to the ambient vehicle dynamic pressure.

The downforce shown in Table 20 is 227.496 N for the full vehicle. Downforce is obviously a desirable reaction which improves tyre traction and vehicle stability.





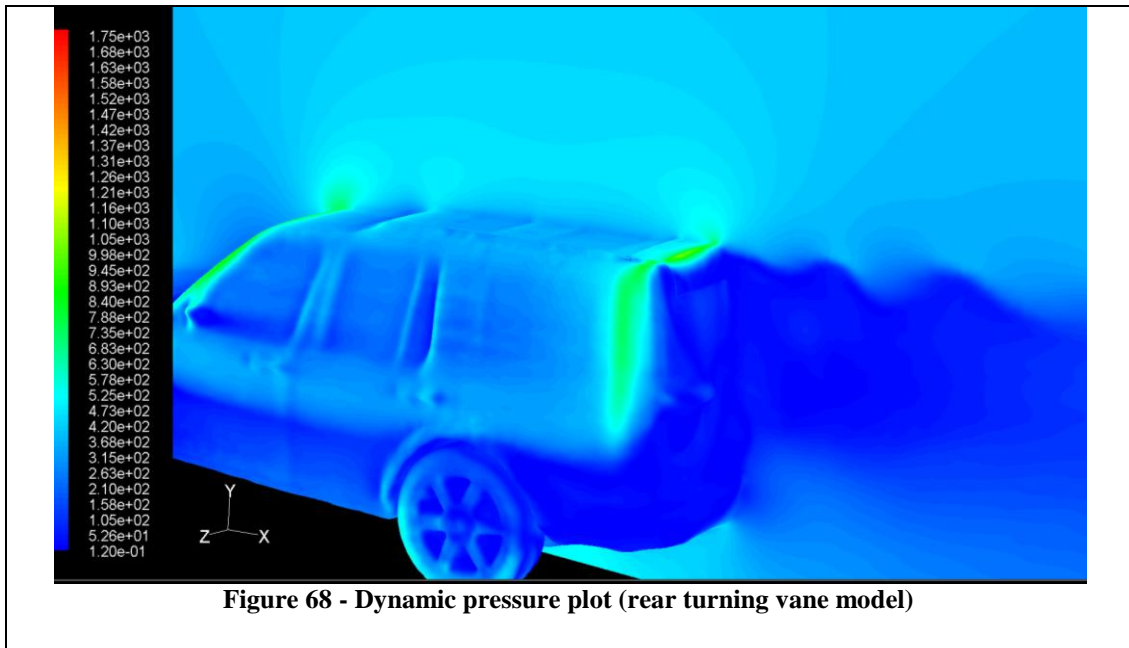
As can be seen from Figure 66 one major zone of boundary layer separation is located on the front tyre surface (un-covered by the front air-dam). This major area of adverse pressure gradient has been noted in published Jaguar data for drag reduction: increasing front wheel coverage (total  $C_D$  decrease = 0.006) produced drag reductions mainly at the rear of the vehicle. The reverse can even be the case: increasing roof camber (total  $C_D$  decrease = 0.003) reduced the drag of the front end substantially, but increased base drag. Data obtained from Jaguar, Gaylard<sup>11</sup>.

**Table 20 - Aerodynamic force (Downforce -Y direction)**

Datum model	Downforce = 227.49N
-------------	---------------------

The datum vehicle used in this investigation is an approximation to the actual vehicle model used by Jaguar Land Rover. The die-cast scale model and scanning technique removed lower body detail, but led to a good similarity to the wind tunnel model. The process of identifying, ‘regions to modify or flow structure to suppress losses’ as described by Gaylard<sup>11</sup>, is the most important out-come of scale model analysis.

## Rear turning vane



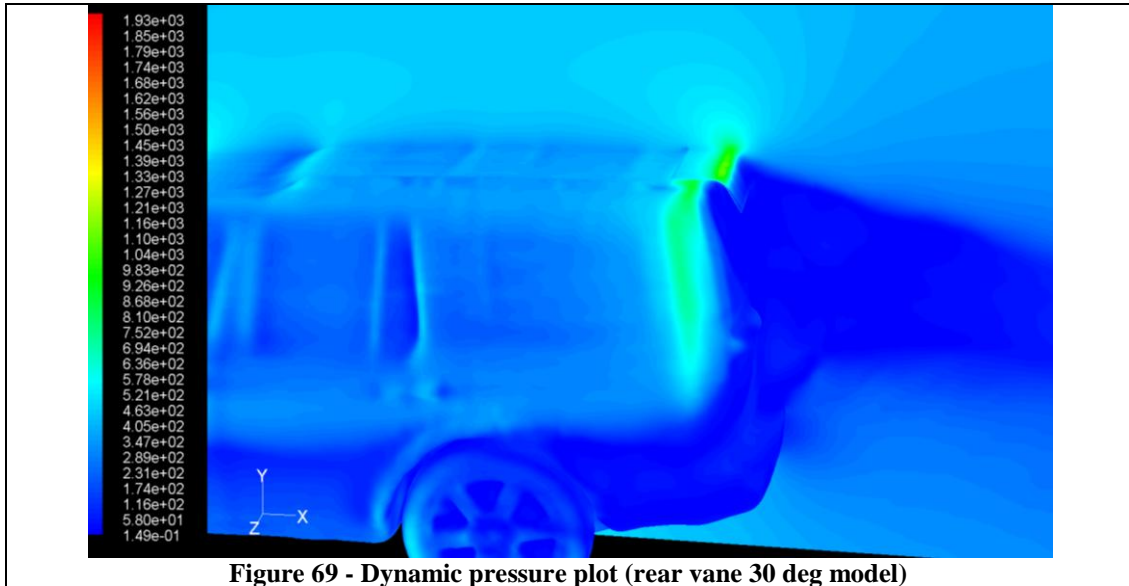
The Rear roof turning vane shown in Figure 68 (and *section 4.2.6*) was the initial design which showed a marked drag decrease. The dynamic pressure image in Figure 68 still shows an area of dynamic pressure increase, and hence boundary layer separation, but the vane appears to have shifted the area of separation further towards the rear. The adverse pressure gradient zone appears to have been evenly distributed by the vane, recirculation vortices are apparent in the wake and higher pressure air has been injected towards the rear of the vehicle.

**Table 21 - Aerodynamic force (Downforce -Y direction)**

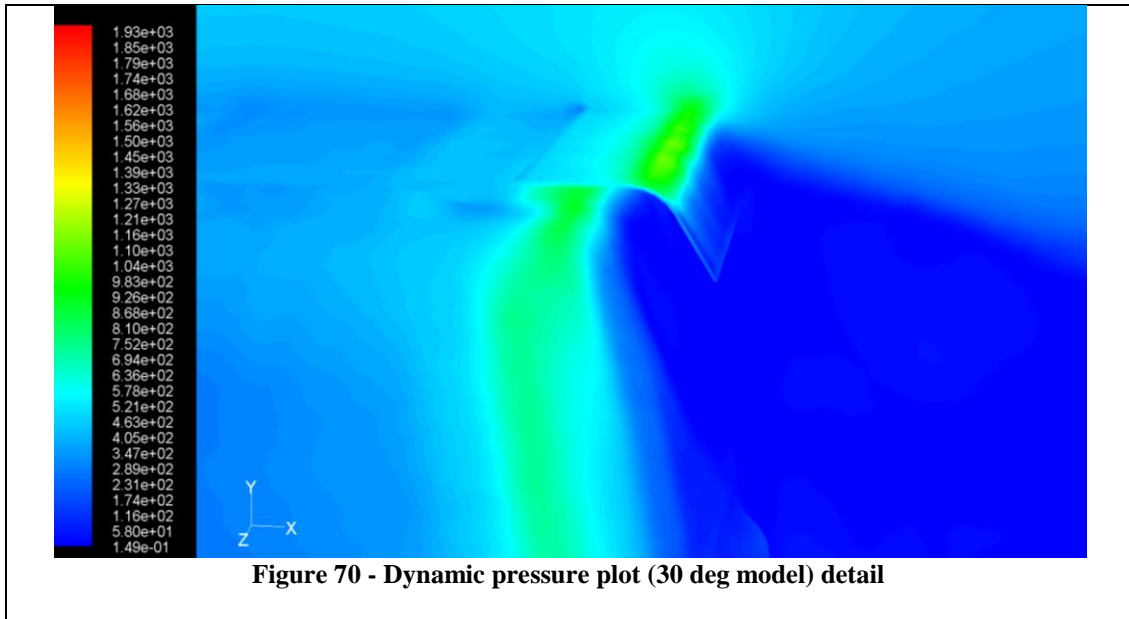
Rear roof turning vane	Downforce = 236.58N 4% greater than datum
------------------------	--

The effect on the vehicle's downforce is apparent from Table 21; the downforce has risen to 236.59 N for the full vehicle. It is reasonable to assume that the rear vane has had an affect with regard to the other induced drag forces i.e. downforce, and lift induced drag. Lift interference is most important for streamlined bodies designed to generate lift, such as aerofoils. Most bluff bodies are inefficient generators of lift; lift interference can be neglected<sup>#</sup>.

## Rear turning vane 30 deg



The 30 degree vane from *section 4.3* is another design that showed  $C_D$  decrease. The vane can be seen to have a similar effect to the original rear turning vane's, but it acts much more like a diffuser, similar to Figure 47. The upper section of the vane has reduced the occurrence of recirculation vortices - allowing a more gradual separation.



In Figure 70 it can be observed that the vane has shifted the zone of adverse pressure gradients, thus maintaining the boundary layer slightly longer. The downforce is considerably lower in this case as can be noted from Table 22, 185.58 N for the full

model. This could be attributed to the diffuser's not inclining the resultant force vector on the vehicle downwards.

**Table 22 - Aerodynamic force (Downforce -Y direction)**

Rear turning vane 30 deg	Downforce = 185.58N 18.43% less than datum
--------------------------	---

**Rear turning vane 60 deg**

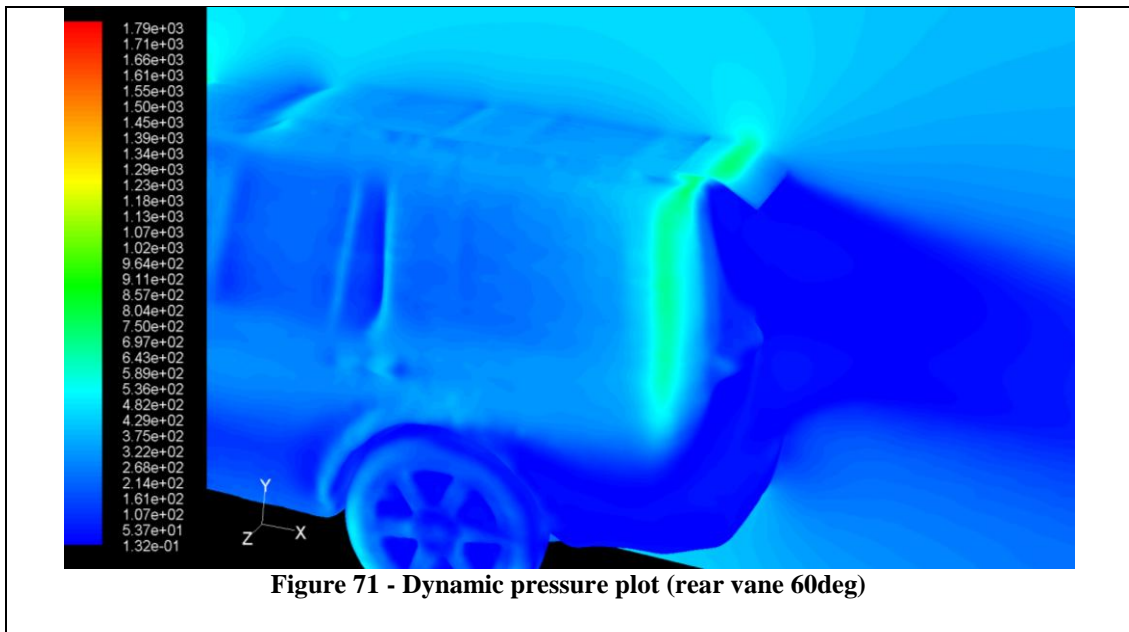


**Figure 71 - Dynamic pressure plot (rear vane 60deg)**

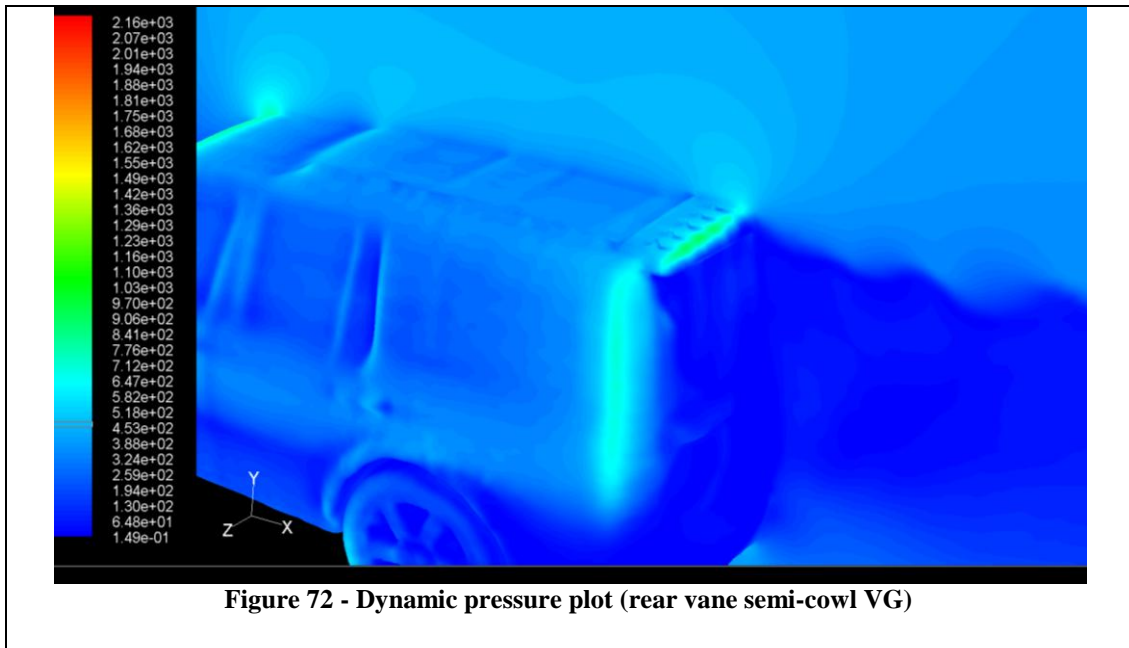
A similar effect can be noted in Figure 71 as compared to Figure 70. The smoother, more gradual, direction change in the upper section of the vane leads to a decreased adverse pressure gradient. This vane is almost at a stage of *favourable pressure gradient*, due to the gradual drop in vane angle.

**Table 23 - Aerodynamic force (Downforce -Y direction)**

Rear turning vane 60 deg	Downforce = 225.5N 0.88% less than datum
--------------------------	---

The downforce has returned to a number approaching that of the datum model, 225.5 N for the full model (Table 23). Again the diffuser shape and relative angle to the ground have little effect on increasing downforce; the increased flow over the top section of the vane probably leads to this increase in downforce.

## Rear turning vane semi-cowl and Vortex Generation



The design pictured in Figure 72 (and also *section 5.2.4*) shows the effect on the dynamic pressure. The cowled edges have had an immediate impact on the ‘fencing-off’ of the rear boundary zones - as a result the rear side shows a near *favourable pressure gradient*. The overall adverse pressure gradients have dropped, and the area over which they act has decreased in area, and the vortex generators are energising the flow and encouraging re-attachment.

**Table 24 - Aerodynamic force (Downforce -Y direction)**

Rear turning vane semi-cowl and vortex generation	Downforce = 259.6N 14.11% greater than datum
---	---

The downforce has increased markedly from the datum model, as a result of the redirection of the vehicle force vector. The ‘filled in’ sides to the vane seem to have had the effect of increasing this effect. The full vehicle downforce associated with this design is 259.6 N, a 32.1 N downforce increase when compared to the datum model (Table 24), leading to greatly increased traction and improved handling.



## 6. Engineering drawings, and wind tunnel set-up

Wind tunnel testing was carried out to verify the CFD procedure and to provide data to compare with virtual turning vane analysis. The wind tunnel used was a re-circulating closed-loop sub-sonic system.

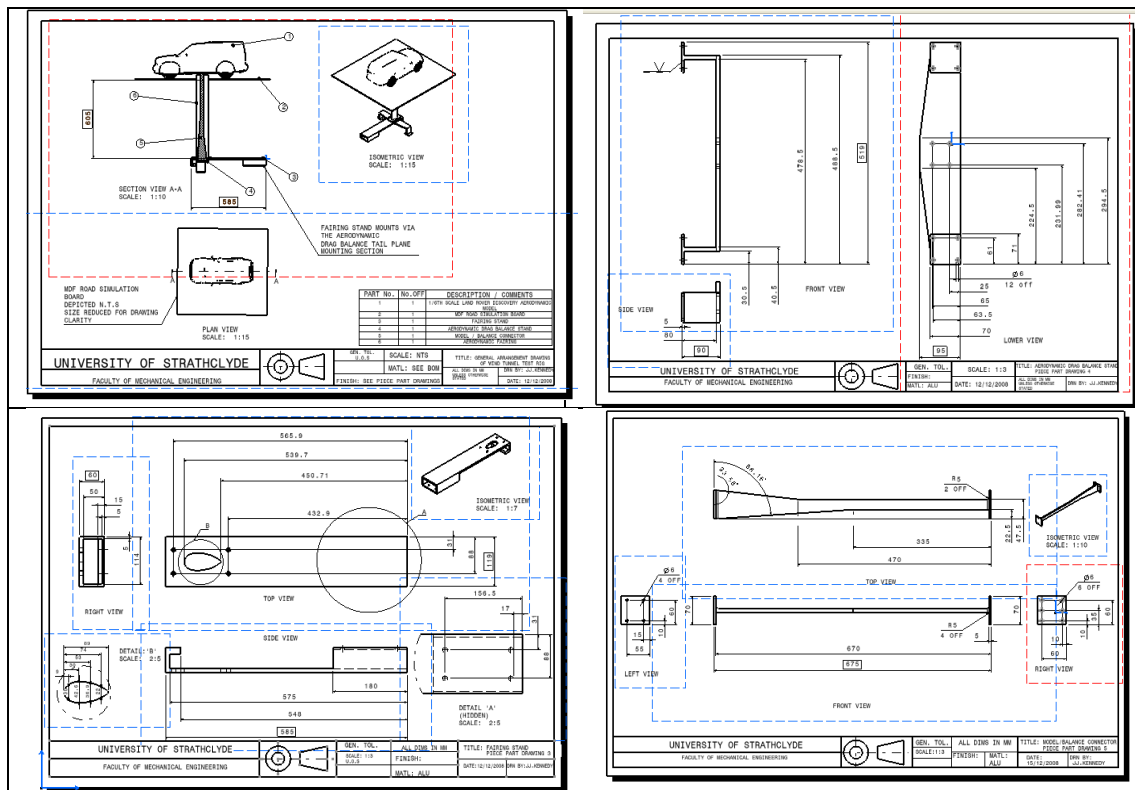


Figure 73 - Engineering drawings, see appendix for detailed prints

The engineering drawings in Figure 73 were created after lab work and discussion regarding both the wind tunnel measurement-taking and the apparatus currently available.

The use of the wind tunnel balance was agreed on. However the balance was designed for testing aeroplane prototypes - as a result it has fixing positions under each wing and also one for the tail plane. This set-up is obviously useless for vehicle testing, so a test-rig had to be developed, designed and drawn for manufacture.



As can be seen in the engineering drawings (*See Appendix*) a system was designed that utilises the tail plane fixing on the aerodynamic balance. This provides a fixing for the aerodynamic fairing, which in turn houses the connector that bolts to a bridge that sits above the cross bar on the balance. The other end of the connector screws into wooden/nylon block bonded to the cavity currently occupied by the battery case on the underside of the model's chassis.

The Lab set-up and test-rig was manufactured accurately and well; piece-parts such as the wooden block and mounting structures were developed and worked well in the test situation.

The vehicle itself was created from two separate *Discovery* model cars, the wheels were operated via remote control, and a 4-wheel drive battery-operated chassis was chosen to allow the wheels to rotate freely with no external apparatus. The bodywork was taped and glued to the chassis; all free flow through the body work was minimised.

It was important that the set-up worked correctly and was not hazardous to the operators, nor to the wind tunnel itself.

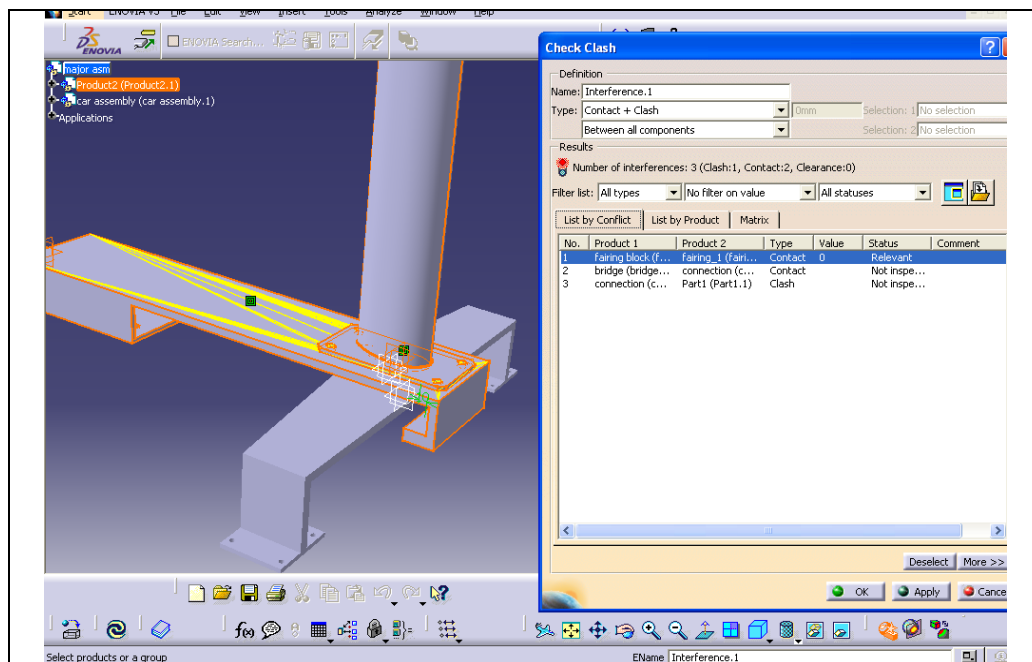


**Figure 74 - Catia V5 'clash detection'**

Clash detection function can test to see if mating components and closely fitting components have been assembled without clashing.

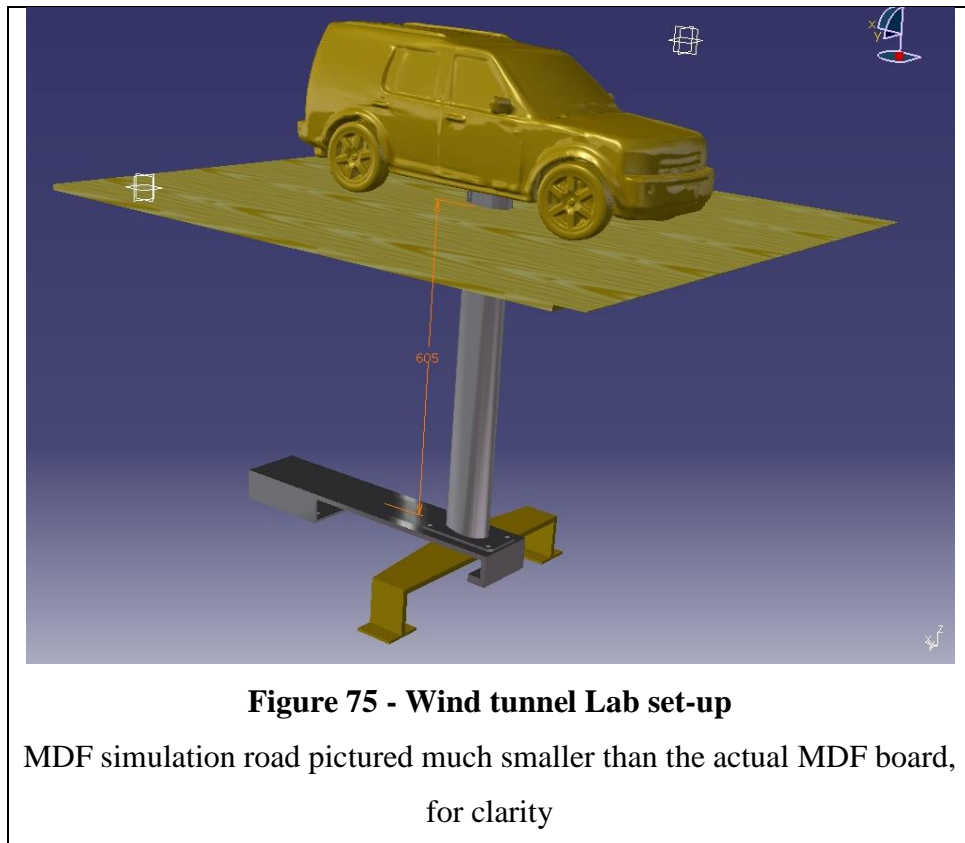


**Figure 75 - Wind tunnel Lab set-up**

MDF simulation road pictured much smaller than the actual MDF board,  
for clarity

The creation of a product containing all of the wind tunnel test components (Figure 75), and the use of the clash detection function in *Catia V5* (Figure 74) was an effective visual aid – and using the kinematics function the vehicle’s wheels can be made to spin. This provides assurance that the set-up will fit and will work appropriately in the lab, before any material is cut, or even ordered.

Torsion and/or bending forces on the connector were deemed to be minimal, due to the fact that the connector is not tethered but moves with the aerodynamic balance. Structural forces, on the other hand, led to a mis-reading of re-directed force on the wind tunnel drag balance. As a result a Force test was set up with the apparatus. Figure 76 shows the actual lab set-up (before the stationary road was applied), this can be compared with Figure 75.



Figure 76 - wind-tunnel lab set-up

### 6.1. Lab set-up drag force test

The Lab set-up drag force test was set up as illustrated in Figure 77. A cord was attached to the vehicle attachment plate and mass was added to simulate a drag force.



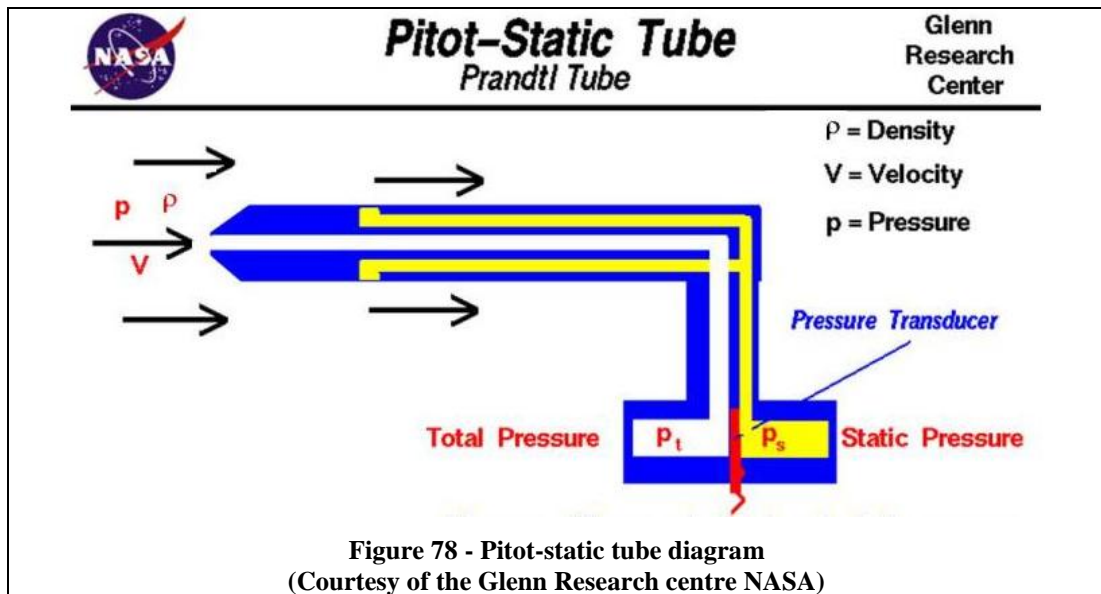
Figure 77 - drag force test

Unsurprisingly the design yielded losses in the transmitted force directed to the aerodynamic balance. This was always going to be an issue due to the unavoidably complex structures necessary to test a vehicle on an aircraft prototype balance. But, after investigation, the amount of drag force (in terms of mass) underrepresented by force lost to the structure was identified, allowing the error to be expressed as an equation. The test identified a constant systematic error (indicating bolt force losses) and also an error varying with respect to applied mass (indicating beam torsion/ bending moment loss). The corrected mass reading in lbs was applied to each result:

**Equation 4**

$$\text{Actual Reading} = \text{Reading} \times 1.176 + 0.35$$

## 6.2. Air velocity calculations



The Air flow velocity in the wind tunnel was calculated using a ‘Pitot-static’ tube, similar to the one pictured in Figure 78. The Pitot static tube (or Prandtl tube, after its inventor) is used as a speedometer on aircraft and Formula one vehicles. The Pitot tube used in the wind-tunnel is approx. 25cm long with a diameter of approx. 1cm. The areas coloured yellow in Figure 78 represent a number of drilled cavities arranged circumferentially around the central drilled opening. These ‘drilled cavities’ remain separate from the system, and allow a static base pressure to be maintained. These cavities marked yellow lead to one side of the ‘pressure transducer’. The other side of the pressure transducer is connected to the centrally drilled opening; the pressure difference is measured by the transducer’s using Wheatstone bridge style pressure gauges connected to a very thin pressure sensitive seal.

From *Bernoulli’s equation*:

$$\text{Static pressure} + \text{Dynamic pressure} = \text{Total pressure}$$

i.e.

Equation 5

$$\left( P_s + \rho \times \frac{V^2}{2} \right) = P_t$$

Solving for velocity:

Equation 6

$$V = \sqrt{2 \frac{(P_t - P_s)}{\rho}}$$

Since

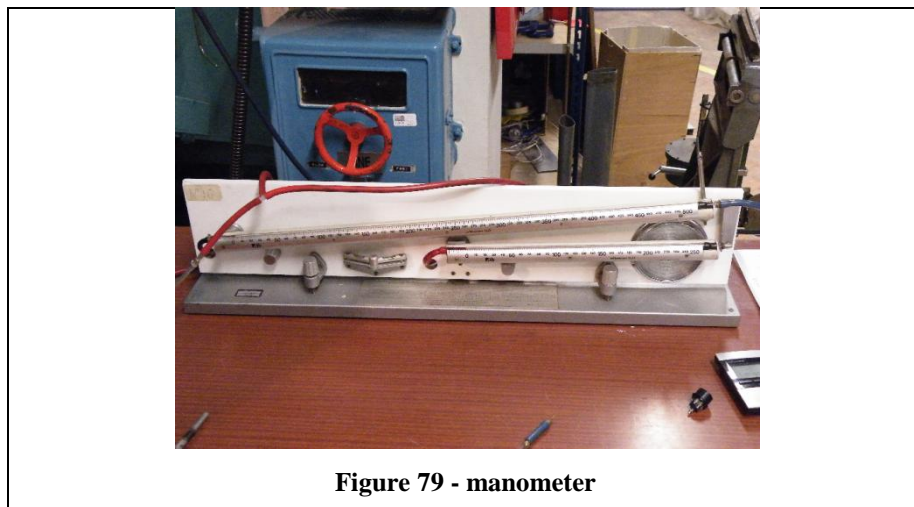
$$P_t = \frac{1}{2} \rho V^2$$

For a velocity of 25m/s

$$P_t = \frac{1}{2} (1.184)(25)^2$$

i.e.

$$P_t = 370\text{Pa}$$



Pressure measurements were taken with the longer manometer pictured in Figure 79, the height  $h$  is corrected using the scale multiplier relevant to the incline and tube used.

Since

$$h = \frac{P_{\text{dynamic}}}{gP_s}$$



→  $h = 31.855$

Using the scale multiplier of 0.2:

$$\text{Manometer reading} = 31.855/0.2 = 159.275\text{mm}$$

The wind-tunnel is designed to predict forces moments pressures and other parameters that an object will be subjected to in an unconfined ‘free-air’ situation. However, wind tunnel walls and object relative size can provide constraints, stifling this supposed ‘free-air’ situation. This is called ‘blockage’, this blockage affects the measured forces and generally has to be adjusted for. The blockage effect was deemed minimal in this investigation due to the projected model area / working area of the wind tunnel (S/A) ratio  $\approx 0.01$ . MIRA standard blockage correction is generally used for full scale vehicle models and is based simply on the area ratio: -

**Equation 7**

$$C_D = \frac{C_{Df}}{(1 - S/A)^2}$$

Equation 7 will generally underestimate blockage correction, although for motor vehicle shapes, it is of the right order.<sup>21</sup>



**Figure 80 – Mounted SUV model**

Figure 80 shows the model SUV mounted on the connector beam without the floor structure; an effort was made to make sure that the model was placed in the centre of the tunnel at zero degrees of incidence to the oncoming air-flow.

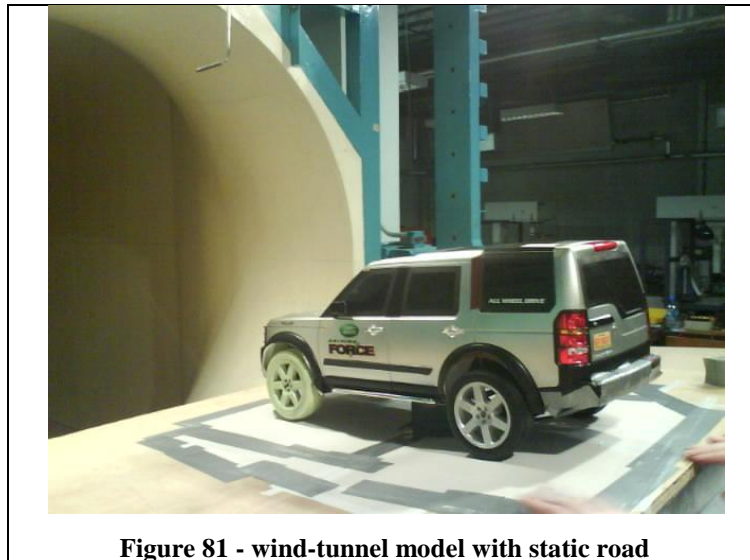


**Figure 81 - wind-tunnel model with static road**

Figure 81 shows the static floor added. Gaps were filled by card board and tape.

## 7. Wind-tunnel results and Analysis

### 7.1. Rear turning vane empirical data

Table 25 shows the wind tunnel data recorded, for the datum model, and differing vane applications. Readings were taken for both static and rotating wheel set-ups. The wheels were operated remotely using the radio controller, the wind speed for all tests was  $25\text{ms}^{-1}$ . Each force was recorded three times; the mean force was then taken and converted to Newtons (N), and adjusted for rig force losses, blockage was neglected.

**Table 25 – Wind-tunnel empirical data**

Angle	Drag (lb) static wheels	Drag (lb) moving wheels	Actual drag (N) static wheels	Actual drag (N) moving wheels	Cd static wheels	Cd moving wheels
0-0	2.25	2.125	13.32	12.672	0.477	0.454
0-10	2.25	2.15	13.32	12.803	0.477	0.458
0-20	2.25	2.2	13.32	13.065	0.477	0.468
0-30	2.2	2.125	13.065	12.672	0.468	0.454
0-40	2.4	2.225	14.111	13.196	0.505	0.473
0-50	2.125	2.075	12.672	12.411	0.454	0.444
0-60	2.2	2.1	13.065	12.542	0.468	0.449
Datum	2.3	2.2	13.588	13.065	0.487	0.468
front top vane	2.225	2.175	13.196	12.934	0.473	0.463
front side vanes	2.2	2.15	13.065	12.803	0.468	0.458





**Figure 82 - roof turning vane model**

Figure 82 shows the addition of a front roof turning vane; 1mm thickness tin was used to create the turning vanes, as it was malleable and did not flap or deform at high wind speeds. Plasticine was hand-moulded to form the connecting struts and was used in conjunction with electrical tape to prevent the vane from detaching and/or forming a hazard in the wind tunnel.



**Figure 83 - side turning vanes**

Front side turning vanes were attached in much the same way as the other vanes, again care was taken to prevent the vanes from detaching (Figure 83). Care was also taken to maintain the vane/vehicle flow channel. Minor  $C_D$  decreases were noted when these turning vane designs were added, but there did appear to be definite decreases, however marginal.



**Figure 84 - Rear turning vane**

The rear vane was mounted on the model vehicle as shown in Figure 84. Attention was paid to placing the vane at a distance of 4.2mm from the roof, as this is a scaled distance relative to the 25mm distance modelled in the 1:1 scale analysis. The boundary layer thickness increases as flow and Reynolds number increases. The angle change for each test was simple to adjust due to the malleable nature of the tin vane. A protractor was used to verify the angle of the adjusted vane, the process worked very well and the vane did not detach or flap at high wind speeds.

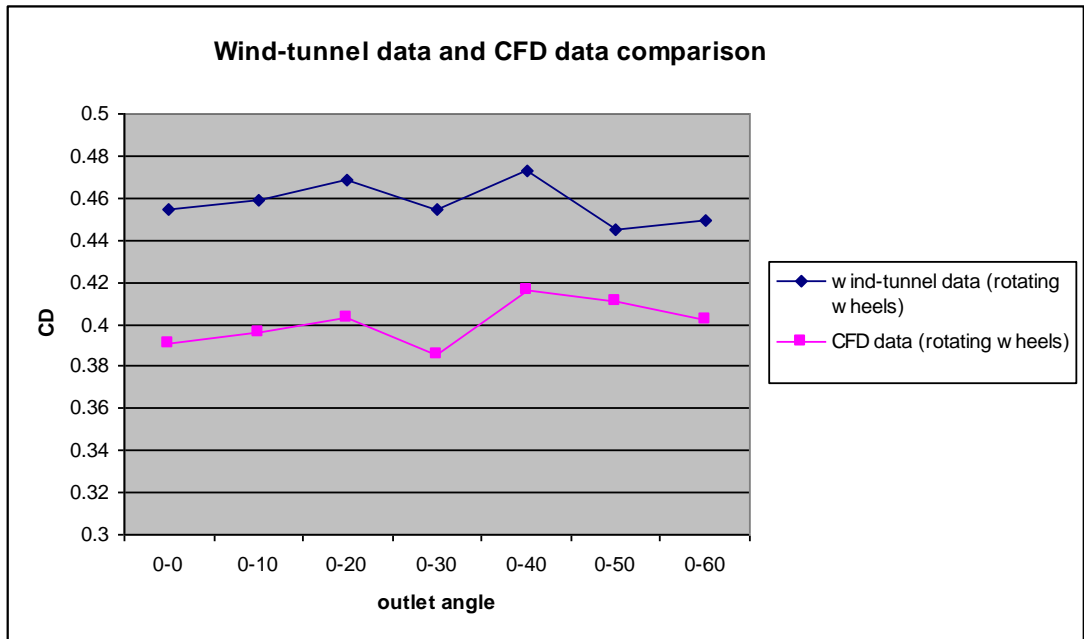


**Figure 85 - Graph to show Wind-tunnel data and CFD data comparison**

The wind tunnel data seemed to compare, at certain points, favourably with the CFD analysis, although a comparison is all that can scientifically be drawn due to Reynolds number differences. Each data point represents the mean force converted to C<sub>D</sub> taken during air speeds of 25ms<sup>-1</sup>, for each rear vane angle. The C<sub>D</sub> can be seen to drop at both 0-30° and 0-50°. Indicating that a diffuser styled rear turning vane could allow a C<sub>D</sub> drop with these configurations.

A similar phenomenon was also noted during CFD analysis, as was the large peak at 0-40°. The most interesting phenomenon noted during wind tunnel testing was the drag force change noted when the wheels were rotating.

## 7.2. *Moving surfaces (wheel rotation discussion)*

Moving surfaces in an aerodynamic context are unique in many ways. The rotating-surface principle is integral to many sports and physical interactions. Newton (1671) was well aware of the nature of the movement of spherical cannon balls with spin applied to them, but it was not systematically investigated until 200 years later by Magnus (1853) and Rayleigh (1877). The downward force generated by a top-spun table tennis ball is the main reason why the game has the velocity of play that it does; and the forces generated by rotating surfaces in mid air allow the travelling ball in the game of football to change direction relative to its initial trajectory.

This phenomenon is predominantly due to the boundary layer on the moving surface, and, importantly, to the prevention of its separation while the surface is moving fast enough in the direction of flow. Important experiments were conducted by Prandtl (1925) into this phenomenon based on the movement and forces generated on a rotating cylinder in a stream of water.

From this it can be assumed that moving surfaces in an aerodynamic system can work as an 'auxiliary power' and work has been carried out demonstrating possible applications to replace sails on boats, Flettner (1924). It is now more understandable, in terms of force changes, why the drag force change on the rotating wheel SUV model is so marked, compared to that in the static system in the wind tunnel. As was mentioned in earlier sections a vehicle's wheel's rotation has been noted as contributing up to 25% of the overall passenger vehicle drag<sup>18</sup> (within wheel arch). The aerodynamic effect of rotating exposed wheels and the wind tunnel differences between static wheels has been examined before. Research by Fackrell showed that isolated rotating wheels produce less drag overall than do stationary wheel sets.<sup>23</sup>

More research work has been performed by Cogotti (1983) and also Mercker et al.<sup>24</sup>, this work is built on the premise that a rotating wheel produces 3 sets of (major) vortices as shown in Figure 86.

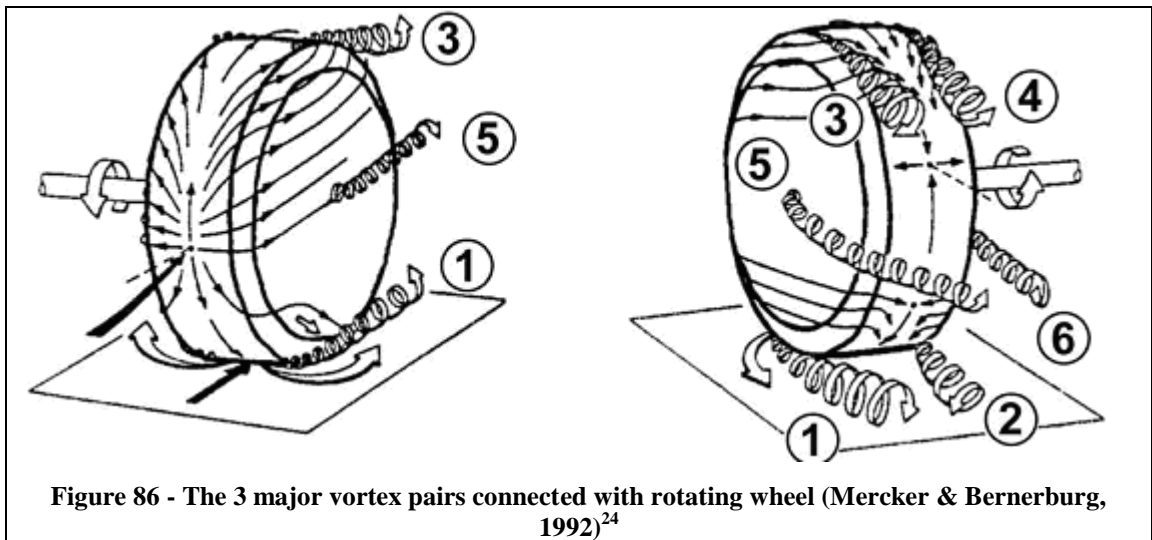
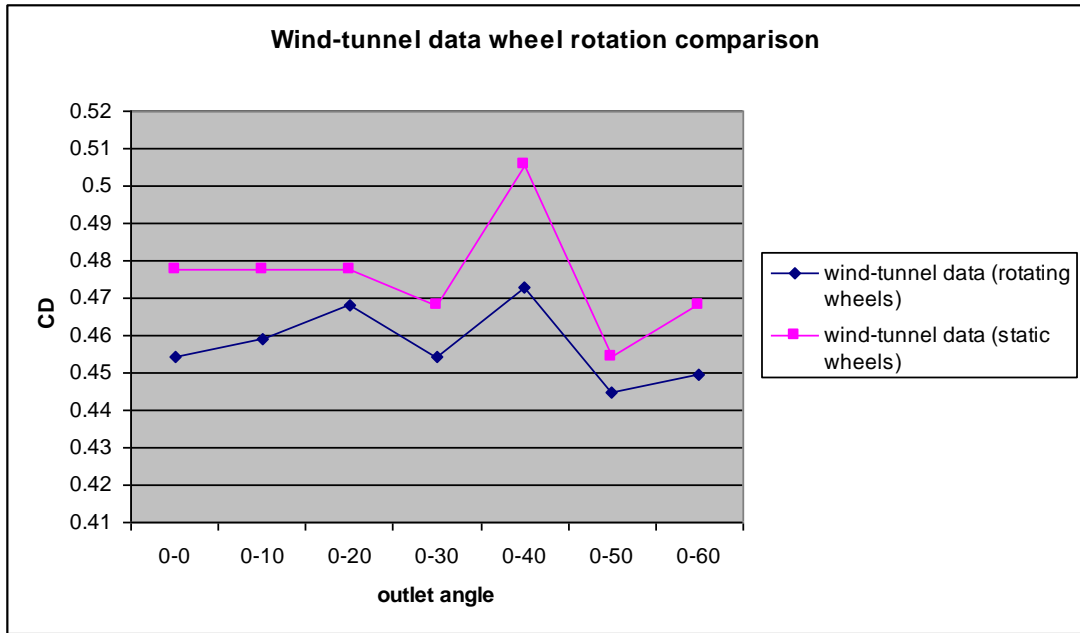


Figure 86 shows a front and rear view of a free wheel rotating on an axle un-covered or cowled in any way in a wind tunnel situation. The three sets of vortex trail pairs can clearly be seen; in research it has been noted that once a wheel arch is applied, (partially covering the wheel) three of these vortex trails disappear, leaving trail 1, 2, and 5 (Figure 86). It was found that vortices 1 and 2 were of much higher intensity than the other 4 vortex trails and these trails have been named ‘jetting vortices’.<sup>25</sup>

The situation encountered in the wind tunnel test of the *Discovery* involved a similar set-up. The stationary ground and moving wheels implied that a clearance distance from wheel to ground had to be maintained to provide an accurate drag reading and also to maintain continuous wheel rotation. Unavoidably, as a result, air flow was present between wheel and ground (although minimised as much as possible). This fact led to an increase in the ‘jetting vortices’ power, the minimisation of the flow against the direction of rotation due to the wheel arch, and thus to a decreased boundary layer separation on the bottommost section of the wheel. As was mentioned earlier the rotating of the surface, or its moving in the direction of flow, will create less drag. Limited research has been done to ascertain whether or not cowled moving wheels in contact with a moving road actually increase or decrease drag. This is due to wind tunnel constraints in creating a model that can be accurately tested in this way; but it can be assumed that the conditions encountered in the stationary ground model are a characteristic of *wind-tunnel* tests, and not actual applications.



**Figure 87 - Graph to show static and rotating wheel comparison in wind-tunnel tests**

The graph above shows the  $C_D$  decrease recorded by applying rotating wheels to the model *Discovery* in the wind tunnel. According to Elofsson et al the drag of a car under rotating-wheels conditions is typically less than the drag of a car under stationary-ground and stationary-wheel conditions. This drag difference has been found to vary from a decrease of about 25 drag counts to a small drag increase according to published sources. A drag reduction of 10 to 20 drag counts is more typical, however.<sup>26</sup>

A drag count of 1 is equal to a  $C_D$  of 0.001; Table 26 and Table 27 shows drag count data for the wind tunnel datum model, with wheels static, and rotating, respectively.

**Table 26 - wind-tunnel datum (static wheels)**

$C_D = 0.487$	487 drag counts
---------------	-----------------

**Table 27 - wind-tunnel datum (rotating wheels)**

$C_D = 0.468$	468 drag counts
---------------	-----------------

A drag reduction of 19 drag counts was noted when comparing static (Table 26), with rotating (Table 27), wheel studies. Which is in the range typically found by Elofsson<sup>26</sup>, this compares well with typical published sources for drag reduction.

Elofsson et al measured his decreased drag count on a full scale vehicle with rotating wheels *and* a moving ground plane. Taking Reynolds scaling effects on the 1/6<sup>th</sup> model, *and* boundary layer thickening on a static ground plane into consideration, this phenomenon is comparable to what was observed in the lab.

### 7.3. *Simulation wind-tunnel*

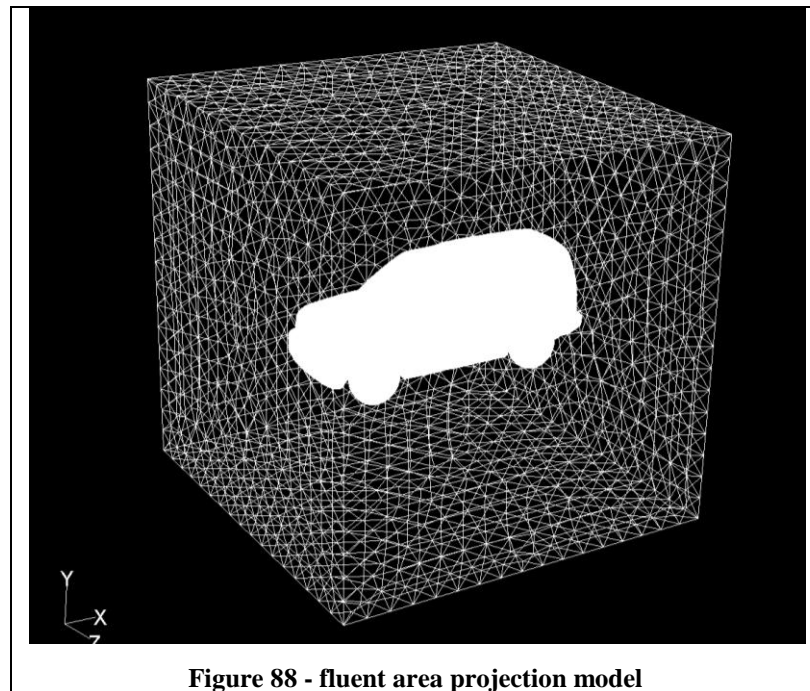
The *fluent* analysis in this case was created as a direct simulation of wind tunnel conditions. In the wind tunnel we had a static road and wheels moving at an estimated speed of 27kph (7.496m/s).

The air temperature was read from the lab thermometer as 26 deg Celsius, the large generator used to power the fan and the unventilated area resulted in a considerably higher lab temperature than was initially assumed. In the full scale *Discovery* simulation Air density was assumed to be 1.225kgm<sup>3</sup> (default sea level at 15 deg C). In this model scale wind tunnel CFD run the Air density was found to be 1.184kgm<sup>3</sup>; this figure was used during empirical C<sub>D</sub> calculation and also for this wind tunnel simulation run.

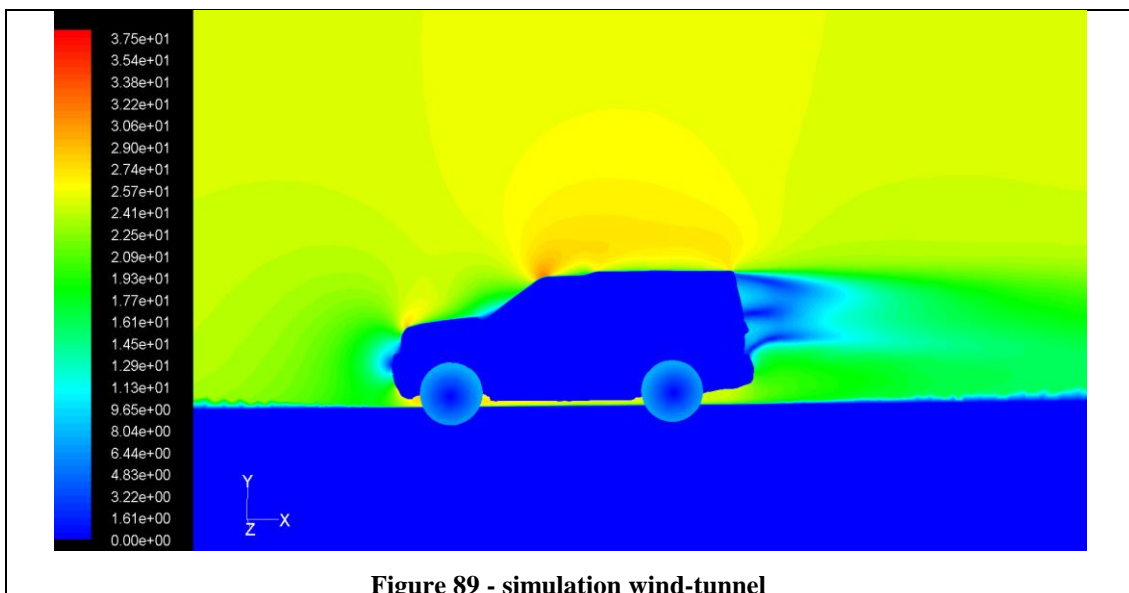
This run was conducted using a standard k-epsilon model at model scale (e.g. 1/6<sup>th</sup> *Discovery* size). Everything during this run was adjusted to emulate the wind tunnel datum simulation. The ground was set as stationary relative to the vehicle, and the wheels were set to rotate at a velocity of 27kph (7.496m/s) ( $\omega = 120.903$  rad/s); this was the approximate maximum vehicle 4 wheel velocity of the model used in the test.

The scale-model projected area of the was found using *fluent*, the scale-model *Discovery* was immersed in a mesh volume and the accurate projected area was calculated (Figure 88).





This projected area was used for the empirical wind tunnel lab work and the *fluent* wind tunnel simulation. A model area of  $0.0754\text{m}^2$  was calculated for the scale-model projected area. During *fluent* simulation only half the vehicle was analysed, creating a projected area of  $0.0377\text{m}^2$ . This projected area is lower than published *Discovery* data, wheel exposure discrepancy, model accuracy and neglected underbody detail led to an under representation of the actual *Discovery* frontal area.





This velocity contour plot (Figure 89) shows the closest accurate simulation of the wind tunnel activity. The road and vehicle are stationary, and the wheels are travelling at a velocity accurate to the manufacturer's approximate maximum 4-wheel capability.

For rotating wheels:-

**Table 28 – Simulation / Actual rotating wheels comparison**

Fluent simulation wind tunnel datum model	$C_D = 0.478$
Actual wind tunnel lab data datum model	$C_D = 0.468$

For stationary wheels:-

**Table 29 – Simulation / Actual static wheels comparison**

Fluent simulation wind tunnel datum model	$C_D = 0.477$
Actual wind tunnel lab data datum model	$C_D = 0.487$

Across the board a  $C_D$  decrease was observed when the scale model wheels were activated in the actual wind tunnel; this decrease was not encountered in the simulation wind tunnel run in Table 28 and Table 29 above. This in part is probably due to the lack of complete similitude between the actual wind tunnel test and the CFD simulated test; this will be discussed in the next section.

The simulated wind tunnel run was an attempt to mirror the exact processes in which the actual wind tunnel test was carried out. As a result it can be seen from the data in Table 28 that the CFD analysis was 97.9% accurate when compared to the Wind tunnel datum model. This shows a good approximation of CFD when compared to wind tunnel situations, but neither the empirical wind tunnel data nor this CFD wind tunnel can be assumed to be dynamically similar (in terms of flow) to the original 1:1 scale SUV, and as a result comparisons may be drawn but not definite rules of scale. Counter balancing and errors due to lost force and blockage have been assessed and applied where necessary.

#### 7.4. Similitude

Similitude is a term used to assess the similarity of a tested model when compared with the real life application. In the case of this project the real life application is the *Land Rover Discovery mk3* SUV travelling at a determined speed in normal conditions. The model tested in the wind tunnel was a 1/6<sup>th</sup> scale model and was tested at differing temperatures and pressures to the application. It is standard practice to test the ‘similitude’ or dynamic similitude of a scale model, in order to verify results and to account accurately for variables that are unavoidable during wind tunnel tests.

While the scale model is being constructed the environment and test procedure also need careful structure. However complete similarity is very difficult to obtain and is generally not as important in vehicle aerodynamics as it is in aeronautics. In low speed wind tunnels it is impossible to maintain the Reynolds number similarity with significantly smaller scale test models. But this does not render the wind tunnel results void, even in low-speed aircraft tests.

For low-speed wing tests, or tests involving highly streamlined objects, lift is the more important data, and drag is neglected. The Reynolds number dictates the flow characteristics seen around an object, and, importantly, the laminar to turbulent transition point. For adequately ‘bluff’ bodies however the lower Reynolds number can confidently be dismissed and the aerodynamicist can be fairly confident of an accurate drag prediction. The use of ‘trip strips’ (roughened tape) applied to test objects can, to some extent, mimic the flow transitions (and flow similitude with 1:1 scale) at lower Reynolds numbers, but would only be used on highly-streamlined objects, not ‘bluff’ bodies such as the *Discovery*.

**Equation 8**

$$\text{Re} = \frac{\rho C l}{\eta}$$

$\rho$  = Fluid density ( $\text{kgm}^{-3}$ )

$C$  = Fluid velocity ( $\text{ms}^{-1}$ )

$l$  = Characteristic linear dimension (m)

$\eta$  = Dynamic viscosity ( $\text{N}\cdot\text{m}^{-2}\cdot\text{s}$ )

$Re = 6.88 \times 10^6$  for the full scale *Discovery*

$Re = 1.14 \times 10^6$  for the model 1/6<sup>th</sup> scale *Discovery*

According to Massey, at  $5 \times 10^5 < Re < 4 \times 10^6$ , since viscous effects are now relatively small, it is probable that  $C_D$  is practically independent of  $Re$ .<sup>5</sup>

The full scale *Discovery* SUV has a Reynolds number (Equation 8) approx. 6 times that of the model scale geometry. This point is undoubtedly a cause for a difference in simulation results compared to wind tunnel results. But for drag comparison the aerodynamicist can be confident of the validity of the wind tunnel outcome, due to the geometric characteristics of the test object.

#### 7.4.1. Geometric Similarity

Geometric similarity is the accuracy in scaling and attention to original morphology of the application portrayed on the model. Whether describing geometric bodies, patterns or fluid flow shapes it is important that the ratio of any length in one system to the corresponding length in the other system is everywhere the same.<sup>2</sup> This ‘ratio’ is more commonly described as the scaling factor, and is probably the most obvious requirement when creating an accurate wind tunnel model, as prototypes in general are scaled from the original by some factor. But shape is not the only factor relating to geometric similarity, surface roughness is also a major factor; this is why the painted original laser-scanned *Discovery* model was not used in the lab tests, due to the difference in its surface texture.

## 8. Conclusions

### 8.1. Turning vane installation data

Front side turning vane structure	$C_D = 0.429$ (2.14% increase from datum)
'A' frame Turning vane structure	$C_D = 0.408$ (4.77% decrease from datum)
Windscreen / roof vane	$C_D = 0.399$ (5% decrease from datum)
Side rear vane	$C_D = 0.408$ (2.858% decrease from datum)
Rear roof vane	$C_D = 0.377$ (10.24% decrease from datum)
Large inlet/nozzle outlet (Figure 49)	$C_D = 0.447$ (6.42% increase from datum)
Narrow inlet/Diffuser outlet (Figure 50)	$C_D = 0.397$ (5.48% decrease from datum)
Rear cowl (Figure 52)	$C_D = 0.399$ (5% decrease from datum)
Rear semi-cowl (Figure 55)	$C_D = 0.372$ (11.43% decrease from datum)

### 8.2. Vortex Generation data

Delta 'bump' vortex generators	$C_D = 0.411$ 2.15% decrease from datum
Delta 'fin' VGs, 25mm	$C_D = 0.398$ 5.24% reduction from datum
Rear vane with 'fin' VG addition	$C_D = 0.365$ 13.1% decrease from datum
Front fender Vortex generator design	$C_D = 0.391$ 6.91% decrease from datum

### 8.3. Downforce data

Datum model	Downforce = 227.49N
Rear roof turning vane	Downforce = 236.58N 4% greater than datum
Rear turning vane 30 deg	Downforce = 185.58N 18.43% less than datum
Rear turning vane 60 deg	Downforce = 225.5N 0.88% less than datum
Rear turning vane semi-cowl and vortex generation	Downforce = 259.6N 14.11% greater than datum

- A drag decrease of 13.1% has been found while using a turning vane structure on the rear roof of the vehicle (Figure 64).
- The turning vane effect does not decrease drag for already well rounded vehicle components (e.g. the air-flow remains attached to the under tray in ***Error!*** ***Reference source not found.*** until the sharp corner), (also side turning vanes are ineffective on the *Discovery* due to the suitable radius currently employed).
- Evidence suggests that any drag reduction obtained derives from the increase in the effective external radius of the turning vane.
- Inappropriately placed turning vanes have at best no discernable effects, and at worst actually increase drag.
- Rear vortex generators when placed as designed (Figure 59) have a drag reducing ability through highly energising the turbulent boundary layer (Figure 58) allowing the boundary layer to survive adverse pressure gradients and remain attached to the surface area for longer, and reducing rear pressure drop. Providing a 5.24%  $C_D$  decrease from datum model of the *Discovery*.
- Optimum size of rear turning vane depends on the angle of the structure and the related adverse pressure gradient, the smoothness of the vane external radius allows adjacent airflow to ‘stick’ to the surface, maintaining attached flow.
- Front vortex generators decrease the over all vehicle  $C_D$  by energising the boundary layer passing over the front wheel arch, allowing sufficient re-attachment reducing vortices.

- The wind tunnel rear vane angle work is comparable to the CFD rear vane angle information, but due to differing Reynolds numbers complete similitude could not be attained in the low speed wind tunnel. However, wind tunnel results can be held as a confident prediction.
- The effect of wheel rotation on decreasing the drag was found to be a characteristic of the wind-tunnel and the method of testing. In industrial wind tunnel testing a ‘stinger’ style balance connector is attached to the model from the top, allowing separate wheel arrangements to rotate with the movement of a ‘conveyer belt’ moving road. Many other papers have shown a drag reduction when the configuration used in this project was tested, and actual road data seems to confirm otherwise.<sup>22</sup> This discrepancy could be a result of fan-moment not being measured as indicated in [18].
- The additions to the rear turning vane had drag relieving effects, the rounded corners of the ‘semi-cowl’ design had a similar effect to that of a ‘horse-shoe spoiler’, and currently many SUV designs on the market have similarly ‘filled in’ outboard edges.
- The ‘fin’ vortex generators possibly had a dual effect of energising the flow over the top of the rear turning vane and increasing the chance of re-attachment, and also acting as boundary layer fences, preventing thickening and drag increase.
- The CFD and the wind-tunnel data agrees very well, which shows that the CFD modelling process used can be trusted.
- The rear turning vane semi-cowl with vortex generation had an added effect of greatly increasing downforce. This could be due to the redirection of resultant force vectors. This design appears to aid the drag reduction and downforce generation of the *Discovery* markedly.

## 9. References

- 1) Schenkel,M, Aneiros,R, Frasher,D, Anderton,I Elliott-Sink,S, 2006, *Improving Aerodynamics to Boost Fuel Economy* [online], [cites 05-02-2006], Access: <http://www.edmunds.com/advice/fueleconomy/articles/106954/article.html>
- 2) Massey,B.S., 1989, '8.8.3 Pressure Drag', 6<sup>th</sup> Edition, *Mechanics of Fluids*, Chapman & Hall, London.
- 3) Massey,B.S.,1989, '9.2.3 Dynamic Similarity', 6<sup>th</sup> Edition, *Mechanics of Fluids*, Chapman & Hall, London.
- 4) Goro,T, 1999, '2.2.1 Introduction to the Boundary layer', 1<sup>st</sup> Edition, *The Leading Edge*, Robert Bentley, Cambridge MA, USA.
- 5) Massey,B.S., 1989, '8.9 Boundary Layer Control', 6<sup>th</sup> Edition, *Mechanics of Fluids*, Chapman & Hall, London.
- 6) Thwaites, B., 1960, 'the calculation of the Boundary layer' 1<sup>st</sup> edition, *Incompressible Aerodynamics*, Oxford University Press, Clarendon Press, Oxford, UK.
- 7) Euler, Leonhard, E258 *Principia Motus Fluidorum, Novi Commentarii academiae Scientiarum Petropolitanae* 6, 1761, pp.271-311. Reprinted in, *Opera Omnia: Series 2, volume 12*, pp.133-168. Available online at EulerArchive.org
- 8) Euler, Leonhard, E332 *Recherches Sur le mouvement des Rivieres (Research concerning the flow of Rivers)*, *Mémoires de l'académie des Sciences de Berlin* 16, 1767, pp.101-118. Reprinted in, *Opera Omnia: Series 2, volume 12*, pp.272-288. Available online at EulerArchive.org
- 9) Euler, Leonhard, E276 *Dilucidationes de Resistentia Fluidorum (Clarification into Fluid Resistance)*, *Novi Commentarii academiae Scientiarum Petropolitanae* 8, 1763, pp.197-229. Reprinted in *Opera Omnia: Series 2, volume 12*, pp.215-243. Available online at EulerArchive.org
- 10) McBeath, S., 1998, *Competition car Downforce*, ISBN – 0 854299777, G.T. Foulis & Company, UK.
- 11) Gaylard, A.P., 2009, *The Appropriate Use of CFD in the Automotive Design Process*, SAE no. 2009-01-1162, 2009
- 12) Department for Transport (DfT), (2007) *Freight Best practice: Quick guide to truck Aerodynamics*, Queens Printer and Controller of HMSO 2007, U.K.

- 13)** Konica Minolta group, 2004, *3D Digitizing KONICA MINOLTA 3D Laser scanner Applications in medical science*, Copyright 2004 Konica Minolta Photo Imaging Europe GmbH, printed in Germany
- 14)** Lanfrit, M., 2005, '3. Meshing', *Best practice guidelines for handling Automotive External Aerodynamics with FLUENT*, Version 1.2, Fluent Deutschland GmbH Birkenweg 14a64295 Darmstadt/Germany
- 15)** FLUENT Inc. (1998) *Fluent 5 User's Guide Volume 2*, E.I. du Pont de Nemours and Company, Fluent Incorporated, Lebanon
- 16)** Speziale, C.G; Thangam, S., *Analysis of an RNG based turbulence model for separated flow*, Smithsonian/NASA physics paper.
- 17)** Hucho, W.H., (Ed.) *Aerodynamics of Road Vehicles*, ISBN – 10 0408014229pp 15-152, Butterworth, 1987
- 18)** KOIKE, M.; NAGAYOSHI, T.; HAMAMOTO, N. (2004), 'Conclusions', *Research on Aerodynamic Drag Reduction by Vortex Generators*, Mitsubishi Motors technical review No.16
- 19)** Kim, K., Geng, X. and Chen, H. (2008) *Development of a rear spoiler of a new type for mini-vans*, Int. J. Vehicle Design, Vol. 48, Nos. 1/2, pp.114–131 doi: [10.1504/IJVD.2008.021155](https://doi.org/10.1504/IJVD.2008.021155)
- 20)** Jiyuan TU, Guan Heng YEOH, Chaoqun LIU., (2007) *Computational Fluid Dynamics: A Practical Approach*, ISBN - 0750685638, 9780750685634, Elsevier Science & Technology, 2007
- 21)** Dr D.J. Cockrell et al., (November 1980) *Blockage correction for bluff bodies in confined flows*, EDSU 80024, Amended A March 1998
- 22)** Wickern, G., Zwicker, K. & Pfadenhauer, M. *Rotating wheels – Their impact on wind tunnel test techniques and on vehicle drag results*. SAE n° 97133, 1997.
- 23)** Fackrell, J. E. *The aerodynamics of an isolated wheel rotating in contact with the ground*. PhD Thesis, University of London, 1974.
- 24)** Mercker, E. & Bernerburg, H. *On the simulation of road driving of a passenger car in a wind tunnel using a moving belt and rotating wheels*. 3<sup>rd</sup> Int. Conf. Innovation and Reliability, Florence, April 8-10, 1992.
- 25)** Morelli, A. *A new aerodynamic approach to advanced automobile basic shapes*, SAE n° 2000-01-0491, 2000.



**26)** Elofsson, P. & Bannister, M. *Drag Reduction Mechanisms Due to a Moving Ground and Wheel Rotation in Passenger Cars*, SAE no. 2002-01-0531, SAE 2002 world congress & exhibition, Detroit, march 2002

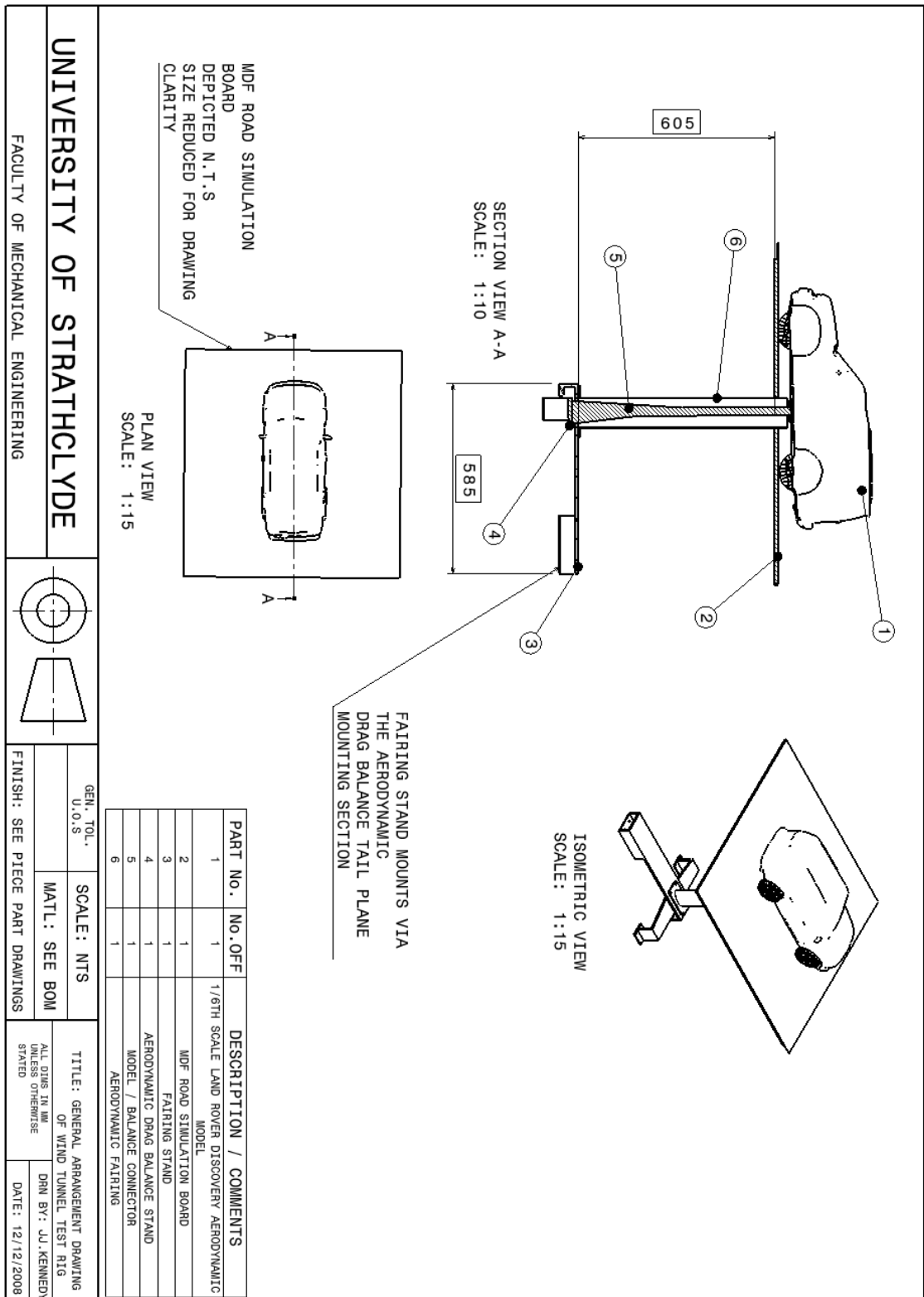
## 10. Publications

The outcomes of this thesis have been the subject of a number of internationally peer reviewed publications, and one international presentation, these include:

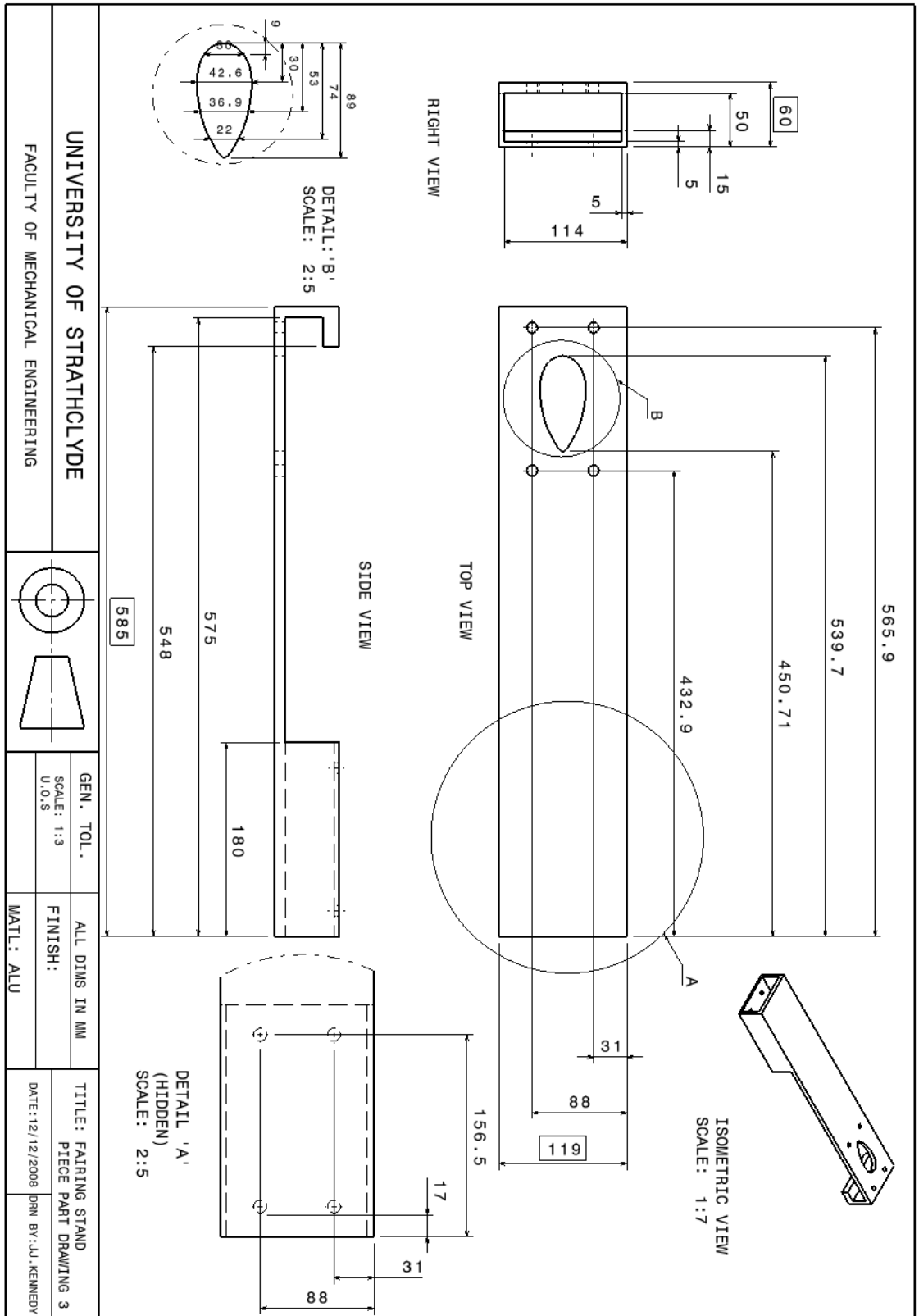
- 1) Kennedy, J.J., Lamond, A., Stickland, M., 2009, *Research into the installation and optimisation of turning vanes and drag reduction technology applied to the Land Rover Discovery MK3 vehicle*, EASC, European Automotive Simulation Conference, July 2009 Munich, Germany.
- 2) A 20 minute presentation of paper, (title above), by J.J. Kennedy, a selected speaker at EASC, European Automotive Simulation Conference, July 2009 Munich, Germany.
- 3) Lamond, A., Kennedy, J.J., Stickland, M., 2009, *Investigation into unsteady base bleed for bluff two-box SUV's*, EASC, European Automotive Simulation Conference, July 2009 Munich, Germany.

# 11. Appendix

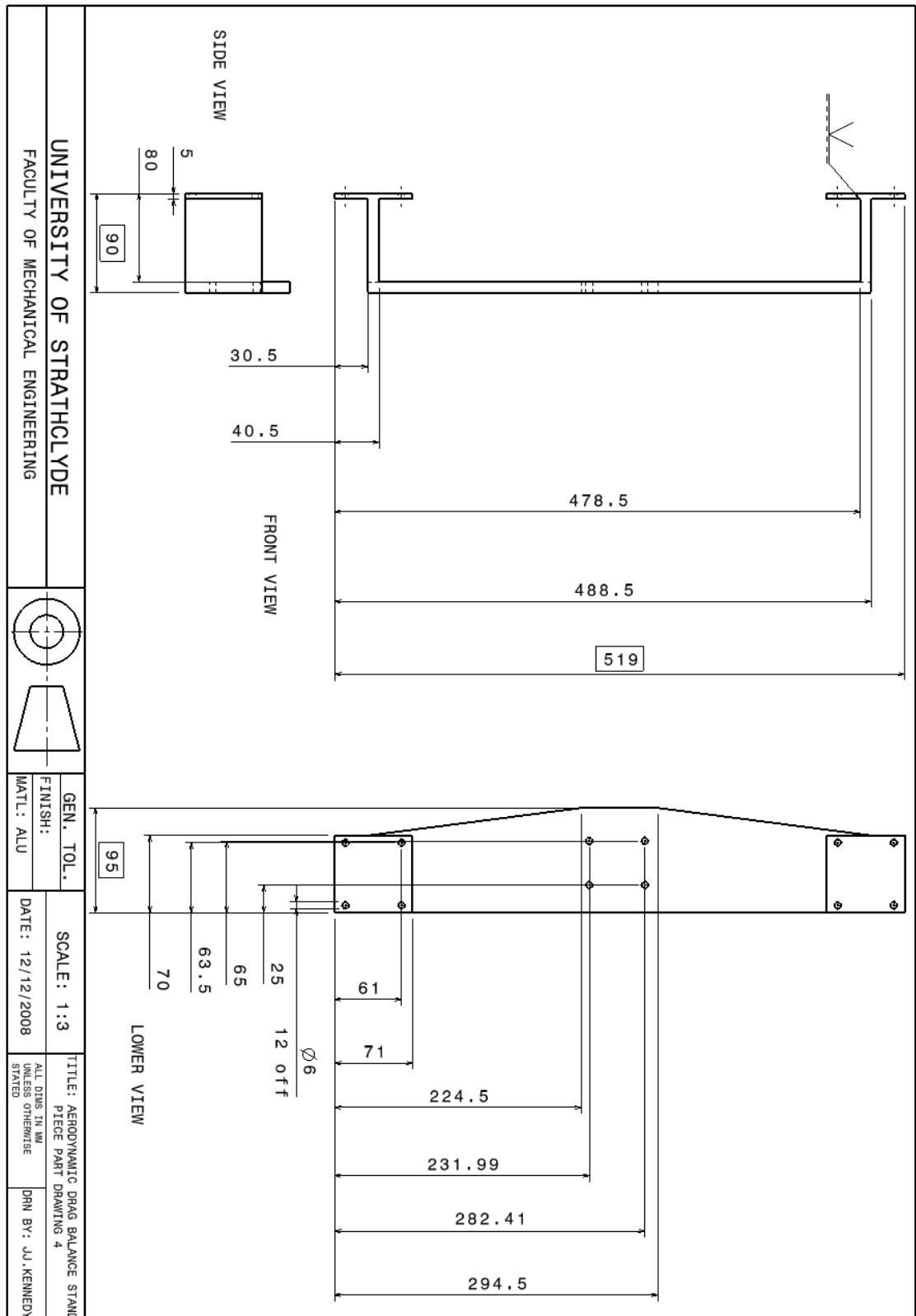
## 11.1. General arrangement drawing



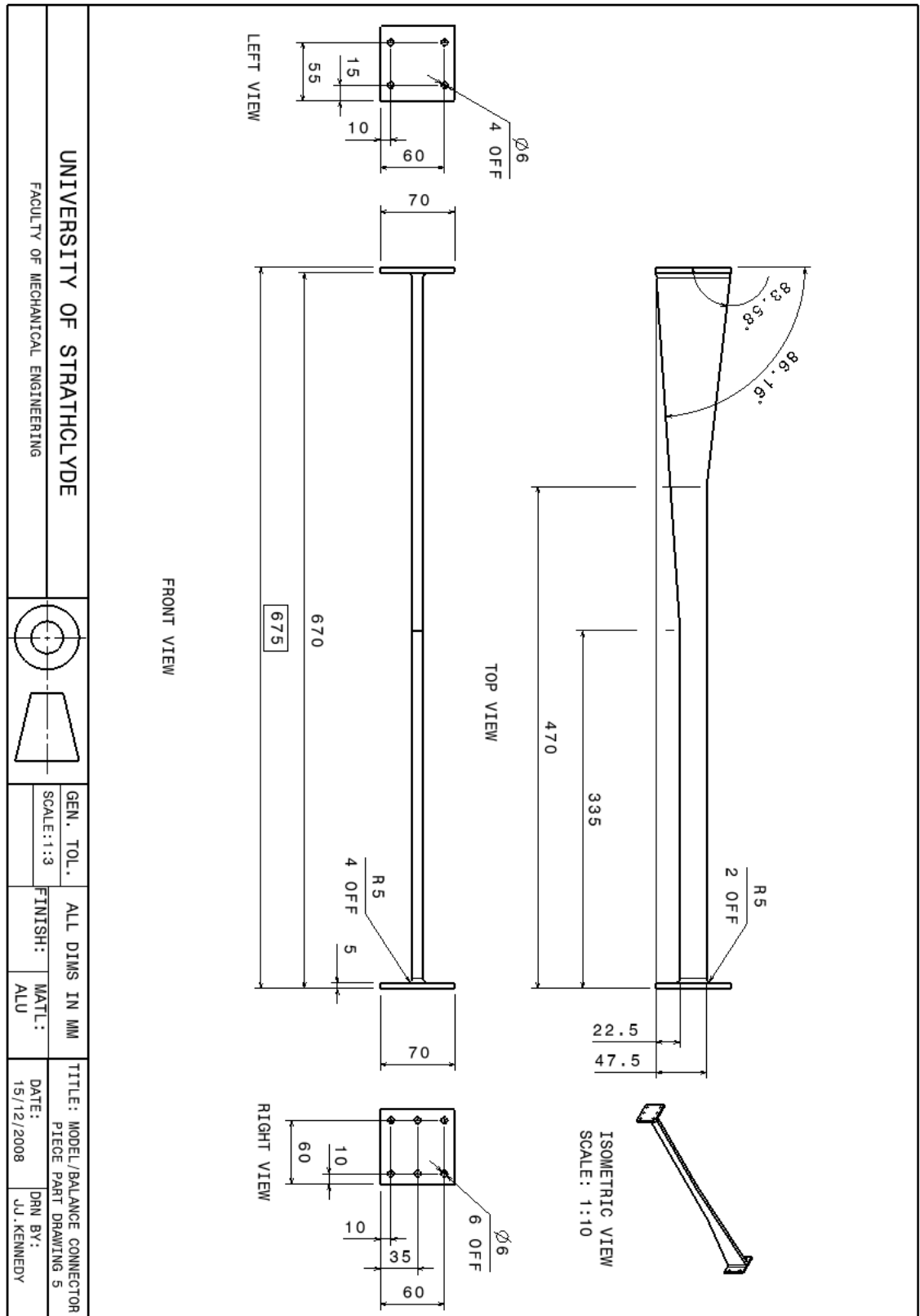
11.2. *Fairing stand Drawing*



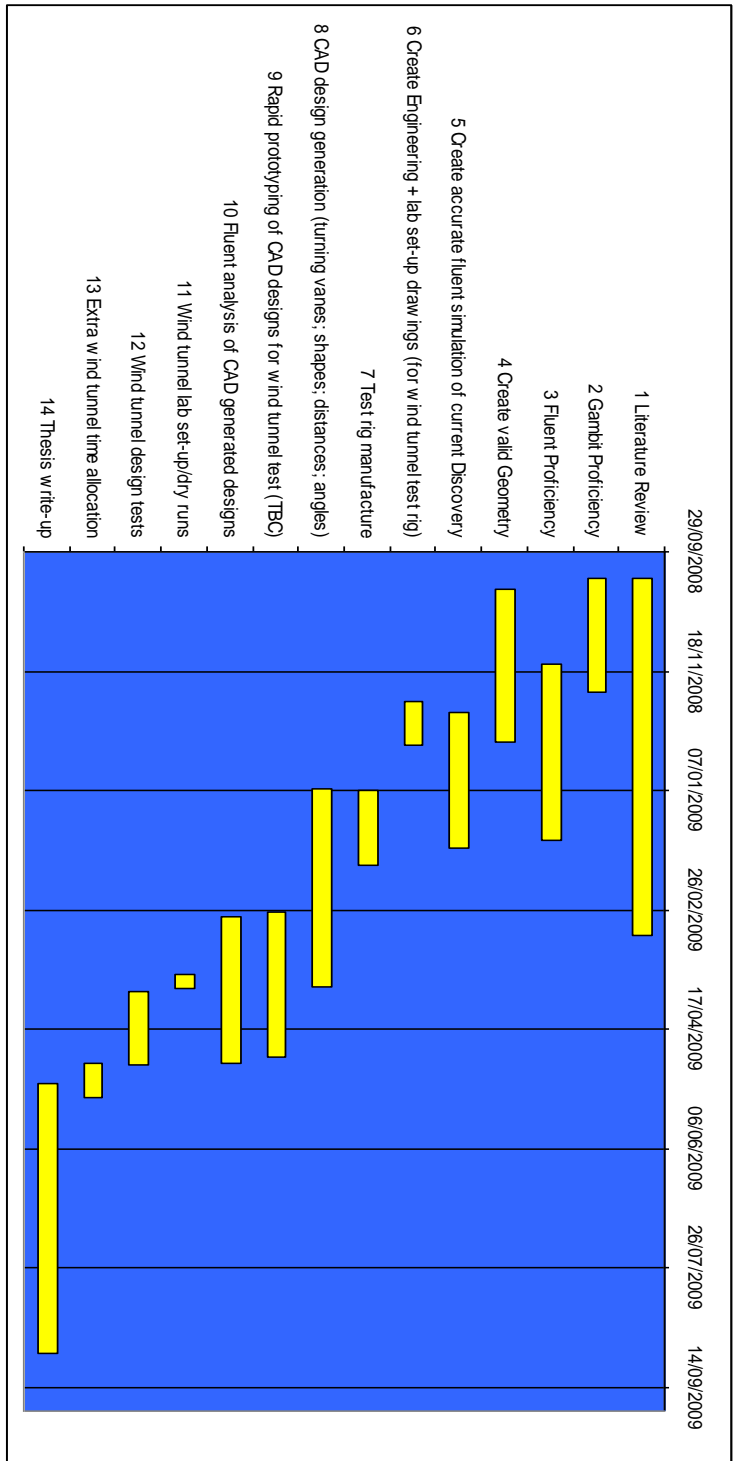
### 11.3. Aerodynamic drag balance stand Drawing



11.4. Model/Balance connector Drawing



### 11.5. Project Gantt chart



## 11.6. Aerodynamic Force plots

**Table 30 – Aerodynamic force plot (datum model)**

Force vector: (1 0 0)						
zone name	pressure force n	viscous force n	total force n	pressure coefficient	viscous coefficient	total coefficient
wall	195.20714	13.03604	208.24318	0.50992923	0.034053355	0.54398258
wheel_front	20.716957	1.1997876	21.916745	0.054117806	0.0031341414	0.057251947
wheel_rear	18.624681	0.99185413	19.616536	0.048652265	0.0025909678	0.051243233
net	234.54878	15.227682	249.77646	0.6126993	0.039778464	0.65247776

**Table 31 – Aerodynamic force plot (side turning vane model)**

Force vector: (1 0 0)						
zone name	pressure force n	viscous force n	total force n	pressure coefficient	viscous coefficient	total coefficient
front_wheel	20.221006	1.2053782	21.426385	0.052822251	0.0031487448	0.055970995
rear_wheel	18.105461	0.96829623	19.073757	0.047295925	0.0025294283	0.049825353
wall	201.4557	12.97666	214.43236	0.52625193	0.033898232	0.56015016
net	239.78217	15.150334	254.93251	0.62637011	0.039576406	0.66594651

**Table 32 – Aerodynamic force plot ('A' frame vane)**

Force vector: (1 0 0)						
zone name	pressure force n	viscous force n	total force n	pressure coefficient	viscous coefficient	total coefficient
wall	190.49995	10.820204	201.32016	0.49763349	0.028265076	0.52589857
wheel_front	19.62702	0.85749841	20.484518	0.051270681	0.0022400001	0.053510681
wheel_rear	19.750299	0.78815252	20.538452	0.051592718	0.0020588513	0.053651569
net	229.87727	12.465855	242.34313	0.60049689	0.032563928	0.63306082

**Table 33 – Aerodynamic force plot (roof vane model)**

Force vector: (1 0 0)						
zone name	pressure force n	viscous force n	total force n	pressure coefficient	viscous coefficient	total coefficient
wall	184.25426	10.62267	194.87693	0.48131752	0.027749032	0.50906655
wheel_front	19.955341	0.98695445	20.942296	0.052128268	0.0025781682	0.054706436
wheel_rear	20.459631	0.90787232	21.367503	0.053445597	0.0023715862	0.055817183
net	224.66923	12.517497	237.18673	0.58689138	0.032698786	0.61959017

**Table 34 – Aerodynamic force plot (rear step vane model)**

Force vector: (1 0 0)						
zone name	pressure force n	viscous force n	total force n	pressure coefficient	viscous coefficient	total coefficient
wall	199.69736	13.110877	212.80823	0.5216587	0.034248841	0.55590755
wheel_front	20.402138	1.1852387	21.587376	0.053295411	0.0030961356	0.056391547
wheel_rear	18.212257	1.0076542	19.219912	0.047574904	0.002632241	0.050207145
net	238.31175	15.30377	253.61552	0.62252902	0.039977218	0.66250624



**Table 35 – Aerodynamic force plot (side rear vane)**

Force vector: (1 0 0)						
zone name	pressure force n	viscous force n	total force n	pressure coefficient	viscous coefficient	total coefficient
wall	193.98668	10.975141	204.96182	0.50674129	0.028669787	0.53541107
wheel_front	18.094749	0.922553	19.017302	0.04726797	0.0024099371	0.049677907
wheel_rear	17.572376	0.80205369	18.37443	0.045903402	0.002095163	0.047998565
net	229.6538	12.699747	242.35355	0.59991266	0.033174887	0.63308755

**Table 36 – Aerodynamic force plot (rear roof vane model)**

Force vector: (1 0 0)						
zone name	pressure force n	viscous force n	total force n	pressure coefficient	viscous coefficient	total coefficient
front_wheel	20.317663	0.95090622	21.268569	0.053074589	0.0024839941	0.055558583
rear_wheel	19.614193	0.85223997	20.466433	0.051236956	0.0022262543	0.053463211
wall	170.99387	11.117846	182.11171	0.44667682	0.02904247	0.47571929
net	210.92572	12.920993	223.84671	0.55098836	0.033752719	0.58474108

**Table 37 – Aerodynamic force plot (Large inlet/nozzle outlet design)**

Force vector: (1 0 0)						
zone name	pressure force n	viscous force n	total force n	pressure coefficient	viscous coefficient	total coefficient
wall	210.74712	10.73003	221.47715	0.55052405	0.028029516	0.57855357
wheel_front	18.630957	0.98029739	19.611254	0.048668708	0.0025607814	0.051229489
wheel_rear	23.289398	0.96536654	24.254765	0.060837719	0.0025217783	0.063359498
net	252.66747	12.675694	265.34316	0.66003048	0.033112076	0.69314256

**Table 38 – Aerodynamic force plot (narrow inlet/diffuser outlet model)**

Force vector: (1 0 0)						
zone name	pressure force n	viscous force n	total force n	pressure coefficient	viscous coefficient	total coefficient
wall	179.82373	13.310188	193.13392	0.46974389	0.034769491	0.50451338
wheel_front	21.378086	1.1824841	22.56057	0.055844828	0.0030889399	0.058933768
wheel_rear	19.197645	1.0122515	20.209897	0.050148979	0.0026442503	0.052793229
net	220.39946	15.504924	235.90439	0.57573769	0.040502681	0.61624038

**Table 39 – Aerodynamic force plot (rear cowl design)**

Force vector: (1 0 0)						
zone name	pressure force n	viscous force n	total force n	pressure coefficient	viscous coefficient	total coefficient
wall	180.82921	13.629385	194.45859	0.47237017	0.035603291	0.50797346
wheel_front	20.520887	1.1747142	21.695602	0.053605582	0.0030606411	0.056674223
wheel_rear	20.168909	0.9884156	21.157325	0.052686129	0.0025819836	0.055268112
net	221.519	15.792515	237.31152	0.57866188	0.041253915	0.61991579

**Table 40 – Aerodynamic force plot (rear semi-cowl design)**

Force vector: (1 0 0)						
zone name	pressure force n	viscous force n	total force n	pressure coefficient	viscous coefficient	total coefficient
wall	169.24942	11.158847	180.40827	0.44212118	0.029149657	0.47127084
wheel_front	19.824297	0.86282176	20.687119	0.051785948	0.002253903	0.054039851
wheel_rear	18.838942	0.86402613	19.702968	0.049211957	0.0022570491	0.051469006
net	207.91266	12.885695	220.79835	0.54311909	0.033660609	0.5767797

**Table 41 – aerodynamic force plot (delta ‘bump’ VG design)**

Force vector: (1 0 0)						
zone name	pressure force n	viscous force n	total force n	pressure coefficient	viscous coefficient	total coefficient
front_wheel	19.346375	0.96087807	20.307253	0.05053747	0.0025100489	0.053047519
rear_wheel	19.250704	0.90008676	20.150791	0.050287555	0.0023512471	0.052638802
wall	192.96294	10.458518	203.42145	0.50406646	0.027320211	0.53138668
net	231.56001	12.319483	243.8795	0.60489149	0.032181507	0.637073

**Table 42 – Aerodynamic Force plot (Delta ‘fin’ VG design)**

Force vector: (1 0 0)						
zone name	pressure force n	viscous force n	total force n	pressure coefficient	viscous coefficient	total coefficient
wall	186.03694	10.754711	196.79165	0.48597393	0.028093932	0.51406786
wheel_front	19.701595	0.85224575	20.553841	0.051465379	0.0022262741	0.053691653
wheel_rear	18.576792	0.84691381	19.423706	0.048527118	0.0022123457	0.050739463
net	224.31533	12.453871	236.7692	0.58596643	0.032532552	0.61849898

**Table 43 – Aerodynamic force plot (rear vane ‘bump’ VG addition model)**

Force vector: (1 0 0)						
zone name	pressure force n	viscous force n	total force n	pressure coefficient	viscous coefficient	total coefficient
wall	183.9041	11.163137	195.06724	0.48040306	0.02916088	0.50956394
wheel_front	18.543283	0.98219174	19.525475	0.04843965	0.0025657281	0.051005378
wheel_rear	18.963943	0.90807545	19.872019	0.049538518	0.002372118	0.051910636
net	221.41133	13.053405	234.46473	0.57838123	0.034098726	0.61247995

**Table 44 – Aerodynamic force plot (Rear vane with ‘fin’ VG addition model)**

Force vector: (1 0 0)						
zone name	pressure force n	viscous force n	total force n	pressure coefficient	viscous coefficient	total coefficient
wall	168.00359	11.179154	179.18274	0.43886673	0.029202703	0.46806943
wheel_front	18.267466	0.8829146	19.15038	0.047719117	0.0023063903	0.050025508
wheel_rear	17.669708	0.80597258	18.475681	0.046157628	0.0021053988	0.048263027
net	203.94076	12.868042	216.8088	0.53274347	0.033614493	0.56635796

**Table 45 – Aerodynamic force plot (front fender vortex generator design)**

Force vector: (1 0 0)						
zone name	pressure force n	viscous force n	total force n	pressure coefficient	viscous coefficient	total coefficient
wall	180.35799	10.696625	191.05461	0.47113983	0.027942239	0.49908207
wheel_front	19.725826	0.9636057	20.689432	0.051528755	0.0025171773	0.054045932
wheel_rear	19.778326	0.88730258	20.665629	0.051665897	0.0023178546	0.053983752
net	219.86214	12.547533	232.40967	0.57433448	0.032777271	0.60711175

## Downforce

**Table 46 - Aerodynamic force (Downforce -Y direction)**

Force vector: (0 -1 0)

zone name	pressure force n	viscous force n	total force n	pressure coefficient	viscous coefficient	total coefficient
wall	56.080261	-0.96370548	55.116556	0.14649549	-0.0025174367	0.14397806
wheel_front	34.965347	-0.33747166	34.627876	0.091338123	-0.00088155934	0.090456564
wheel_rear	24.244379	-0.24027278	24.004106	0.063332306	-0.00062765183	0.062704654
net	115.28999	-1.5414499	113.74854	0.30116592	-0.0040266479	0.29713927

**Table 47 - Aerodynamic force plot (Downforce -Y direction)**

Force vector: (0 -1 0)

zone name	pressure force n	viscous force n	total force n	pressure coefficient	viscous coefficient	total coefficient
front_wheel	38.664448	-0.13537581	38.529072	0.10100077	-0.00035363395	0.10064714
rear_wheel	27.253874	-0.097623862	27.15625	0.071193627	-0.00025501684	0.07093861
wall	53.192474	-0.57813126	52.614343	0.13895145	-0.0015102169	0.13744123
net	119.1108	-0.81113093	118.29967	0.31114584	-0.0021188677	0.30902697

**Table 48 - Aerodynamic force plot (Downforce -Y direction)**

Force vector: (0 -1 0)

zone name	pressure force n	viscous force n	total force n	pressure coefficient	viscous coefficient	total coefficient
wall	30.26325	-0.65087676	29.612374	0.079055066	-0.0017002505	0.077354816
wheel_front	38.58894	-0.1531398	38.4358	0.10080302	-0.00040003889	0.10040378
wheel_rear	24.856159	-0.11146978	24.744689	0.064930412	-0.00029118654	0.064639225
net	93.708349	-0.91548634	92.792863	0.2447893	-0.0023914759	0.24239782

**Table 49 - Aerodynamic force plot (Downforce -Y direction)**

Force vector: (0 -1 0)

zone name	pressure force n	viscous force n	total force n	pressure coefficient	viscous coefficient	total coefficient
wall	56.076427	-0.86282563	55.213602	0.14640544	-0.0022539131	0.14423153
wheel_front	35.559826	-0.31565103	35.244175	0.092891026	-0.00082455826	0.092066468
wheel_rear	22.522356	-0.2292095	22.293147	0.058833943	-0.00059875168	0.058235191
net	114.15861	-1.4076862	112.75092	0.29821041	-0.0036772231	0.29453319

**Table 50 - Aerodynamic force plot (Downforce -Y direction)**

Force vector: (0 -1 0)

zone name	pressure force n	viscous force n	total force n	pressure coefficient	viscous coefficient	total coefficient
wall	65.514004	-0.55054486	64.963539	0.17113893	-0.0014381588	0.16970077
wheel_front	39.338974	-0.13588721	39.203087	0.10276309	-0.00035497086	0.10240812
wheel_rear	25.750227	-0.11660951	25.633617	0.067265937	-0.00030461278	0.066961324
net	130.60328	-0.80304158	129.80024	0.34116795	-0.0020977424	0.33907021